



University  
of Glasgow

<https://theses.gla.ac.uk/>

Theses Digitisation:

<https://www.gla.ac.uk/myglasgow/research/enlighten/theses/digitisation/>

This is a digitised version of the original print thesis.

Copyright and moral rights for this work are retained by the author

A copy can be downloaded for personal non-commercial research or study,  
without prior permission or charge

This work cannot be reproduced or quoted extensively from without first  
obtaining permission in writing from the author

The content must not be changed in any way or sold commercially in any  
format or medium without the formal permission of the author

When referring to this work, full bibliographic details including the author,  
title, awarding institution and date of the thesis must be given

Enlighten: Theses

<https://theses.gla.ac.uk/>  
[research-enlighten@glasgow.ac.uk](mailto:research-enlighten@glasgow.ac.uk)

DIRECT PHOTON AND  $\pi^0$  PRODUCTION  
IN  $\pi^- p$ ,  $\pi^+ p$  AND  $p\bar{p}$  INTERACTIONS  
AT 280 GeV/c.

Stephen Christopher Jack B.Sc.

Department of Physics and Astronomy,  
University of Glasgow.

Presented for the degree of Doctor of Philosophy  
in the University of Glasgow.

January 1989.

ProQuest Number: 10999355

All rights reserved

INFORMATION TO ALL USERS

The quality of this reproduction is dependent upon the quality of the copy submitted.

In the unlikely event that the author did not send a complete manuscript and there are missing pages, these will be noted. Also, if material had to be removed, a note will indicate the deletion.



ProQuest 10999355

Published by ProQuest LLC (2018). Copyright of the Dissertation is held by the Author.

All rights reserved.

This work is protected against unauthorized copying under Title 17, United States Code  
Microform Edition © ProQuest LLC.

ProQuest LLC.  
789 East Eisenhower Parkway  
P.O. Box 1346  
Ann Arbor, MI 48106 – 1346

### ***ACKNOWLEDGEMENTS***

I would like to thank the Science and Engineering Research Council and the University of Glasgow for their financial support, and the Department of Physics and Astronomy, under the guidance of Professors E. Laing and I.S. Hughes, for the facilities provided. I am also very grateful to Professors I.S. Hughes and I. Skillicorn for the opportunity to work in the High Energy Physics Group.

I greatly appreciated the help provided by all my colleagues who worked on the WA70 experiment, in particular my supervisors Drs. J. Lynch and P. Negus, and also Dr. R.M. Turnbull for their advice and guidance. I would also like to thank Dr. D. Frame for his help in the early days, Dr. J. Wells for his advice and endless enthusiasm and Dr. A.S. Thompson for solving all my computing problems. I would also like to acknowledge the assistance of the Systems Programmers and Operations Staff, and Ms. C. MacIntyre for arranging all my travel and accommodation.

I also greatly enjoyed and appreciated the friendship and assistance of all my fellow students and other members of the High Energy Physics Group.

Finally, I would like to thank my mother for the magnificent catering service during my studying bouts, my father for his car breakdown service and both of them for their support during my seemingly endless student days. I am also greatly indebted to Carol for her constant "encouragement" when it seemed that I would never reach the end.

### *Synopsis*

This thesis presents results on direct photon and  $\pi^0$  production in  $\pi^- p$ ,  $\pi^+ p$  and  $p p$  interactions at an incident beam momentum of 280 GeV/c, using data recorded by CERN experiment WA70 at the Omega Prime Spectrometer.

Chapter 1 discusses the theoretical background for direct photon production and presents results from previous experiments.

Chapter 2 describes the experimental apparatus used by WA70, with particular emphasis on the high-granularity electromagnetic calorimeter constructed specifically for the experiment.

Chapter 3 discusses the reconstruction programs used to process the raw data from the Omega Prime Spectrometer and calorimeter prior to performing any physics analysis.

Chapter 4 presents a detailed account of the method, developed by the author, to calculate the efficiencies of the individual planes of the 4m wire chamber, and presents these efficiencies for the two experimental runs.

Chapter 5 discusses some of the methods used in offline calibration of the electromagnetic calorimeter, referring particularly to two separate studies performed by the author;

(i) the detection of a discontinuity in the online calibration for the 1984 data taking run, and (ii) the search for a  $J/\psi$  signal in the 1985 run, which would be particularly useful, since the  $e^+e^-$  pair can be detected in both the wire chambers and photon detector.

In Chapter 6 an analysis of the 1985 data is performed to provide the cross-sections for direct photon and  $\pi^0$  production and the ratio of the cross-sections. This chapter gives a description of the procedures involved in producing the raw signals, calculating the various cuts and contaminations, and evaluating the detection efficiencies for  $\pi^0$  and direct photons.

The  $\pi^0$  cross-sections are compared to the parametrised results from other experiments, and the direct photon cross-sections are compared with the predictions of next-to-leading order QCD.

*Table of Contents*

Acknowledgments	i
Synopsis	ii
Chapter 1 Introduction to Direct Photon Physics	1
1.1 Introduction	1
1.2 Theoretical predictions	1
1.3 Corrections to lowest order predictions	4
1.4 Experimental difficulties	4
1.5 Additional WA70 physics topics	5
1.6 Previous experiments	6
Chapter 2 The Apparatus	9
2.1 Introduction	9
2.2 Beam	9
2.3 Omega Spectrometer	10
2.4 WA70 Calorimeter and 4m Chamber	12
2.5 Trigger	14
2.6 Time of Flight (TOF)	16
2.7 Online Calorimeter Calibration	18
2.8 Data Acquisition System (DACP)	20
Chapter 3 Offline Event Reconstruction	21
3.1 Introduction	21
3.2 Pattern Recognition	21
3.3 TRIDENT	26

Chapter 4 4m Wire Chamber Efficiency	29
4.1 Introduction	29
4.2 Data	29
4.3 Analysis	31
4.4 Fit	32
4.5 Results	34
Chapter 5 Offline Calorimeter Calibration	46
5.1 Discontinuities in Calorimeter Calibration	46
5.2 Absolute Energy Calibration	48
Chapter 6 Direct Photon and $\pi^0$ Analysis	56
6.1 Introduction	56
6.2 Experimental Data Analysis	56
6.3 Backgrounds and Losses	60
6.4 Monte Carlo simulation chain	64
6.5 Systematic Errors	68
6.6 $\gamma/\pi^0$ Ratio	68
6.7 Cross-Sections	70
6.8 Conclusions	73
References	88

## CHAPTER 1

### *Introduction to Direct Photon Physics*

#### 1.1      *Introduction*

The work described in this thesis was performed on data taken by the WA70 experiment at CERN. WA70 is a fixed target experiment designed to study the production of direct photons in hadronic interactions at 280 GeV/c. The author participated in two data taking runs in 1984 and 1985 respectively and a test run in 1983.

#### 1.2      *Theoretical Predictions*

Quantum Chromodynamics (QCD) is now generally accepted as the basic theory describing the strong interaction. In this theory, the fundamental constituents of hadrons are 'gluons' and 'quarks', collectively known as partons. Hard scattering of these fundamental particles can result in the production of large transverse momentum ( $P_t$ ) secondary particles, including photons. A photon is defined as direct or prompt when it comes from the primary parton interaction and not from the subsequent decay of hadrons produced by parton fragmentation or by bremsstrahlung from one of the secondary partons.

At first order in QCD, the two subprocesses involved in direct photon production are the Compton scattering (Fig. 1.1a) and annihilation processes (Fig. 1.1b). These diagrams have equivalent physics content to the corresponding parton interaction diagrams in Fig. 1.2 but the direct photon events provide a much cleaner way of studying the constituent dynamics since the resulting partons in Fig. 1.2 fragment into jets, and this process cannot be treated quantitatively by QCD, since  $a_s$  is a running coupling constant, given by

$$\alpha_s(Q^2) = \frac{12\pi}{(33 - 2f) \ln(Q^2/\Lambda^2)}$$

where,  $Q^2$  is the square of the momentum transfer,  $f$  is the number of flavours that can contribute to the scattering and  $\Lambda$  is a parameter that sets the scale for  $Q^2$ .

For the direct photon production reaction, whose kinematics are shown in Fig. 1.3, the invariant cross-section in factorised form can be written as,

$$E_\gamma \frac{d^3\sigma}{dp_\gamma^3} (A + B \rightarrow \gamma + \dots) = \int \frac{dx_a}{x_a} \frac{dx_b}{x_b} F(a, A; x_a) F(b, B; x_b) \frac{E d^3\sigma}{dp_\gamma^3}$$

where the  $x$ 's are four momenta fractions carried away by the partons, and the  $F$ s are the hadronic structure functions.

Parametrisation of the parton structure functions in nucleons has been produced by fitting experimental data for deep-inelastic lepton scattering,  $J/\psi$  and  $T$  production [1]. These authors produced two sets of fits (subsequently referred to as Duke and Owens Set I and Set II), with the main difference between the two parametrisations being that the Set II gluon distribution is much broader than the Set I gluon distribution. Two equivalent sets of fits have been obtained for the pion structure functions [2]. These parametrisations have been used in calculating the predicted direct photon cross-sections (Chapter 6).

The cross-sections (for example [3]) for the two QCD first order diagrams are

Annihilation : 
$$\frac{d\sigma}{dt} (q\bar{q} \rightarrow g\gamma) = \frac{8\pi\alpha\alpha_s}{9s^2} e_q^2 \frac{\hat{u}^2 + \hat{t}^2}{\hat{u}\hat{t}}$$

Compton : 
$$\frac{d\sigma}{dt} (qg \rightarrow q\gamma) = \frac{\pi\alpha\alpha_s}{3s^2} e_q^2 \frac{\hat{u}^2 + \hat{s}^2}{\hat{s}\hat{u}}$$

where,  $e_q$  is the quark charge and  
 $s, t$  and  $u$  are the Mandelstam variables.

The cross-sections for the processes in Fig. 1.1 are basically reduced by  $a/a_s$ , the ratio of the strong to the electromagnetic coupling constant, in comparison to the corresponding process in Fig. 1.2.

However, the  $\gamma$ /jet production ratio becomes greater as  $P_t$  is increased for a fixed  $X_f$ .\* This is a result of  $a_s$  being a running coupling constant, which decreases with the hardness of the collision and hence with higher  $P_t$ .

Experimentally, in order to reduce errors caused by uncertainty in energy calibration, it is convenient to measure the ratio  $\gamma/\pi^0$  production. This ' $\gamma/\pi^0$ ' ratio is further enhanced relative to the  $\gamma$ /jet ratio since

- (1) the quarks or gluons must fragment, therefore the  $\pi^0$ 's do not possess the total  $P_t$  of the parent partons,
- (2) in the harder processes, which produce the high  $P_t$  jet, the fragmentation function is softer and so the hadronic constituents of the jet have a smaller fraction of the total momentum of the jet.

In addition, the annihilation process becomes dominant as  $P_t$  is increased, and so due to their respective quark contents, the ratio

$$\sigma(\pi^- p \rightarrow \gamma X)/\sigma(\pi^+ p \rightarrow \gamma X).$$

is expected to increase with increasing  $P_t$ .

Due to the different quark content of the pions and protons, the  $X_f$  distributions for the direct photons and  $\pi^0$ 's in proton production should be symmetric about zero, whereas for pion production the distributions are expected to be forward biased.

$$* X_f = \frac{2 P_{T,cm}}{\sqrt{s}}$$

### 1.3 Corrections to lowest order predictions

There are several corrections which need to be made to the simplified first order predictions.

In the preceding section, the colliding partons were assumed to have zero Pt. However, the intrinsic Pt of the partons (normally referred to as  $k_t$ ) is usually represented as a Gaussian distribution, with mean between 0.4 - 1.0 GeV/c. Since  $k_t$  contributes to both direct photon and  $\pi^0$  production, its effect is expected to be greatly reduced when considering the  $\gamma/\pi^0$  ratio [4].

As previously mentioned, there is a contribution to single photon production from bremsstrahlung. This has been estimated [5,6], for various values of  $\sqrt{s}$  and Pt, to be < 30 % of the total single photon rate.

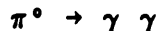
Direct photon production by higher twist processes, where a parton from one hadron interacts with the other hadron, has also been considered. However, these contributions have been shown [7] to be insignificant.

Full second order calculations have been performed [8] including bremsstrahlung contribution, and these have been used with the structure functions of Duke and Owens Sets I and II to provide the theoretical predictions given in the results section. The main difficulty in producing quantitative theoretical predictions is setting the  $a_s$  and structure function  $Q^2$  scales, which cannot be predicted by QCD. The method used for determining the 'optimised' scales was the minimum sensitivity approach [9], where the scales are varied until a stationary point is found in the calculated cross-section.

### 1.4 Experimental difficulties

Although direct photons are expected to provide relatively clean events, the detection of a good sample of direct photons is experimentally very difficult to

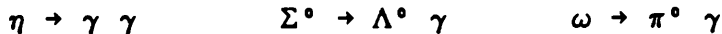
achieve, due to the small cross-section and the large background of high Pt photons from other processes. The main contribution to this background comes from the electromagnetic decay,



This decay can resemble a high Pt direct photon in several ways ;

- 1) the  $\pi^0$  decays asymmetrically, producing a low energy photon below the threshold of the photon detector,
- 2) merging of the two photons which will then resemble a single shower in the reconstructed event.
- 3) one of the photons misses the photon detector,
- 4) a photon converts to an  $e^+e^-$  pair.

Other important sources of photon background are the decays ;



### 1.5 Additional WA70 Physics Topics

Although no results will be presented here on these topics, the WA70 experimental data is being used to study event structures and double direct photon production.

Since WA70 can reconstruct charge particle tracks in the OMEGA [10] wire chambers, the structure of direct photon and  $\pi^0$  events can also be studied. Such studies are expected to show that the high Pt photon triggers are relatively isolated, whereas high Pt  $\pi^0$  triggers should be accompanied by other particles, since the  $\pi^0$  is part of a jet.

If the recoil jet can be reconstructed in direct photon events, this again provides information on the fractional momenta of the colliding partons. Also, since the annihilation contribution is expected to be much greater in the  $\pi^- p$  interactions, studies of the structure of the away side jets for the different beam particles, should provide a comparison of the quark and gluon fragmentation processes.

The study of double direct photon production should provide a powerful technique for studying the dynamics of parton interactions due to the relatively simple theoretical analysis and the removal of the complication of parton fragmentation and jet reconstruction. However, detection of a significant double direct photon signal is even more difficult than for single photons, since the cross-section is again essentially reduced by the ratio of  $a/a_s$ .

### **1.6      *Previous experiments***

The first indications of high Pt direct photon production were provided at the CERN Intersecting Storage Rings (ISR) and at Fermilab, with the first published results being produced by experiment R412 at the ISR in 1976. However, in general, the results obtained by experiments at that time were either inconclusive or inconsistent with present observations.

A complete review of the results obtained in earlier experiments will not be given here, as this is well covered elsewhere [11]. The more recent results have also been fully covered [12].

Recent results on direct photon production have been produced by both fixed target and collider experiments at CERN. Unlike the earlier experiments, the CERN fixed target experiments were specifically designed to study direct photon production, and so, in addition to presenting results on the traditional  $\gamma/\pi^0$  ratio, results have been given for direct photon cross-sections and comparisons have been

made between these results and next to leading order calculations with the Duke and Owens structure functions Sets I and II.

Of the fixed target experiments, NA24 [13] has produced results for the direct photon cross-section and  $\gamma/\pi^0$  ratio in  $\pi^- p$ ,  $\pi^+ p$  and  $p p$  interactions at 300 GeV/c. The cross-sections all agree well with the predicted values produced using Duke and Owens Set I. The  $\gamma/\pi^0$  ratios increase with Pt in all three cases as does the ratio  $\sigma(\pi^- p \rightarrow \gamma X)/\sigma(\pi^+ p \rightarrow \gamma X)$ .

NA3 [14] has published final results for direct photon cross-sections in  $\pi^- C$ ,  $\pi^+ C$  and  $p C$  interactions at 200 GeV/c. Again, the results favour the Duke and Owens Set I structure functions and the measured  $\gamma/\pi^0$  ratio increases with Pt for all three interactions.

In colliding beam experiments, R808 has produced corrected  $\gamma/\pi^0$  ratios for  $p\bar{p}$  and  $p p$  interactions at  $\sqrt{s} = 53$  GeV [15] and in  $p p$  interactions at 63 GeV [16]. A direct photon signal has been observed in both cases, but statistics are not good enough to detect any differences between the two ratios.

UA2 [17] has measured direct photon cross-sections in  $\bar{p} p$  interactions at  $\sqrt{s} = 546$  GeV and  $\sqrt{s} = 630$  GeV. This experiment differs from those mentioned above, in that the electromagnetic background produced by  $\pi^0$  decay is not removed by attempting to reconstruct the  $\pi^0$  mass, but instead a converter is placed in front of the calorimeter and the background is calculated by a statistical process. The ratios of the  $\gamma$  and  $\pi^0$  cross-sections at the different energies are compared with calculated values and found to be in excellent agreement. Also, the  $\gamma/\text{jet}$  ratio is close to the expected value.

UA6 [18] has presented preliminary results for direct photon cross-section and  $\gamma/\pi^0$  ratio in  $\bar{p} p$  interactions. The cross-section again shows agreement with predictions using Duke and Owens Set I.

WA70 has also presented its final results on direct photon production for  $\pi^- p$  and  $\pi^+ p$  interactions [19] and  $p p$  interactions [20]. The results for  $P_t$  and  $X_f$  distributions for all three data sets are in clear agreement with results obtained using Duke and Owens Set I.

*Figures - Chapter 1*

Fig. 1.1      The two first order subprocesses for direct photon production.

a) Compton scattering.

b) Annihilation.

Fig. 1.2      The corresponding diagrams to Fig. 1.1 for jet production.

Fig. 1.3      Kinematics for direct photon production.

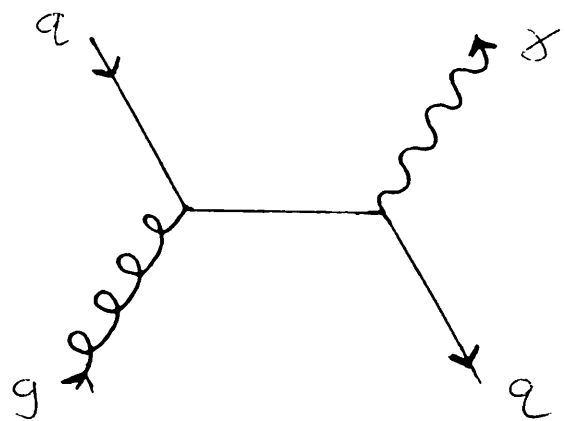


Fig. 1.1a

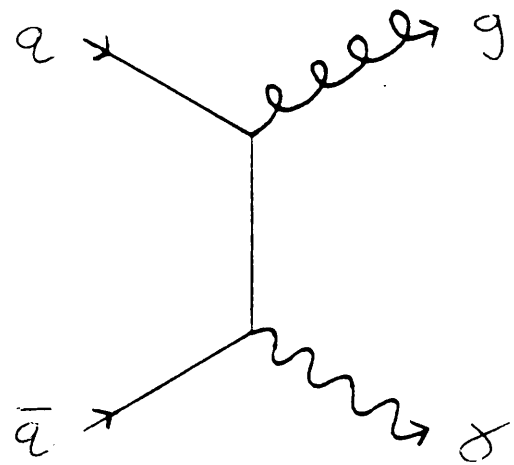


Fig. 1.1b

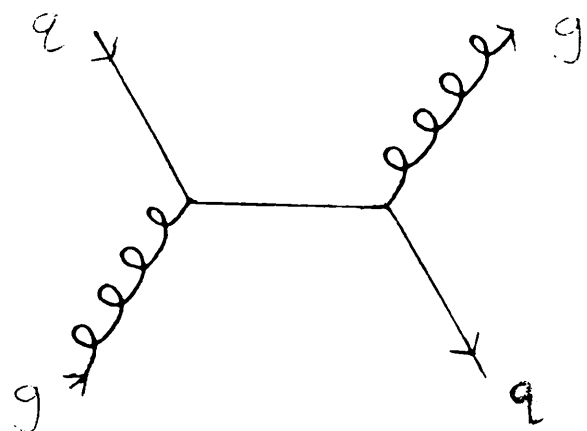


Fig. 1.2a

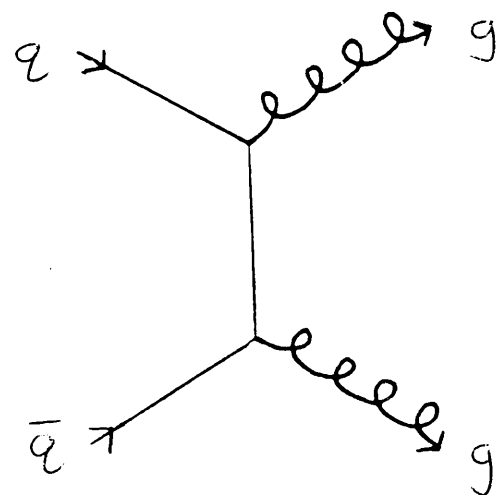


Fig. 1.2b

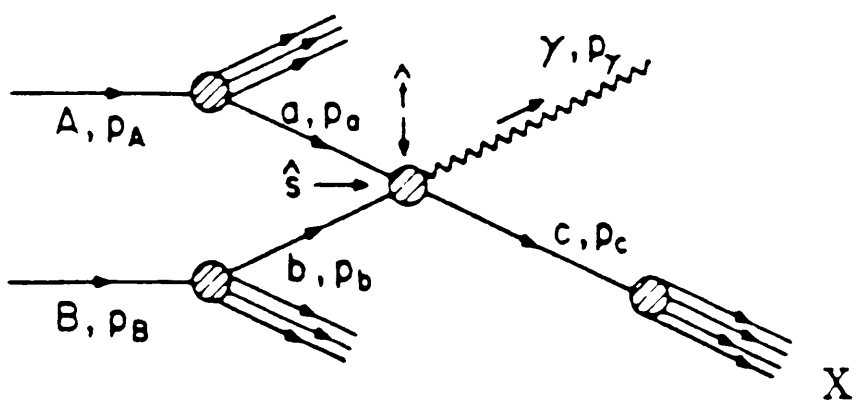


Fig. 1.3

## CHAPTER 2

### *The Apparatus*

#### 2.1 *Introduction*

The WA70 experiment used the Omega Spectrometer facility at CERN, and constructed a lead-liquid scintillator electromagnetic calorimeter [21] and a large 4m x 4m Multiwire Proportional Chamber (4m chamber) specially for the experiment. This chapter describes the arrangement and operation of the experimental hardware (Fig. 2.1).

#### 2.2 *Beam*

The experiment was performed in the H1 beamline in the West Area and the data were recorded with 280 GeV/c unseparated beams of positive and negative hadrons incident on a liquid hydrogen target. The original proton beam extracted from the SPS at 400 GeV/c was incident on a 50 cm Beryllium target. The magnets and collimators in the H1 beamline defined the momentum and focus of the beam for data taking.

For the positive beam, a polythene absorber was placed in the beam line to enhance the pion content of the beam. This resulted in a final positive beam composition of approximately 20 %  $\pi^+$ , 77 % p and 3 % K $^+$ . The negative beam consisted of around 97 %  $\pi^-$ , 2.6 % K $^-$  and 0.3 %  $\bar{p}$ .

For particle identification during positive beam data taking, two CEDAR Cerenkov counters [22], tuned to identify  $\pi^+$ , were used. Two different types of output signals were taken from the CEDARs. The first was the '6-fold coincidence' for each CEDAR, which corresponded to at least six of the eight photomultipliers in the Cerenkov giving a signal above a specified level. The second type was the PI bit and P bit signals. These involved adding the analogue signals from all of

the photomultipliers (sixteen in total) on both CEDARs and passing the sum to two discriminators. If the total signal exceeded the threshold for the 'higher' discriminator, the PI bit was set. If it was below the threshold for the 'low' discriminator, the P bit was set. The PI and P bits were included in the WA70 trigger logic for positive beam, whereas the '6-fold coincidence' bits (C1 for CEDAR 1 and C2 for CEDAR 2) were simply read by the data acquisition system when an event was accepted, as they arrived too late for the trigger. The rates for the PI and P bits were also recorded on scalers.

### 2.3        *Omega Spectrometer*

The Omega Spectrometer consists of a large superconducting magnet and Multiwire Proportional Chambers (MWPCs) provide tracking information. In addition, just outside the magnetic field a single drift chamber was used for the 1984 data taking run and two drift chambers in 1985, to increase tracking precision.

The Omega magnet has a peak field of 1.8 T at a current of 4800 A. This peak field was used at the beginning of the 1984 data taking run; however, this produced a large number of triggers near the beam hole due to charged particles being swept out by the magnetic field and hitting the inner edges of the calorimeter, and so for the remainder of the 1984 run and all of the 1985 run, the current was reduced to 2800 A, producing a peak field of 1.18 T. The magnet has a half-field diameter of 4 m and a gap between the pole faces of 1.5 m.

Positioned inside the magnet was a liquid hydrogen target of length 1 m and radius 1.25 cm. The ends of the target were positioned at  $x = -1.3$  cm and  $x = -101.3$  cm in the Omega reference frame. This is forward from the usual target position in the Omega, to optimise the calorimeter acceptance, and so the

number of Omega MWPCs used was less than normal.

Immediately downstream of the target were the six 'B' MWPCs. These chambers have two planes of wires with spacing between the wires of 2mm. They are arranged so that the chambers alternately have YU and YV planes. The wires in the Y planes are vertical and the U and V wires are at an angle of  $\pm 10.14^\circ$  to the Y plane. The B chambers have only two planes so that they can be closely packed to assist in the offline reconstruction of the charged tracks near the vertex in the target.

After the B chambers were the seven 'A' chambers, each of which has three planes of wires YUV. The orientation of the wires in the planes are identical to the corresponding planes in the B chambers.

Finally, the drift chambers were positioned outside the magnetic field. These have four planes of wires YUVY' with the wires separated by 5 cm. The Y' wires are parallel to the Y wires but have been offset by 2.5 cm. Since at high beam intensity there is a large background in the drift chambers, due to the drift time of 500 ns, an MWPC consisting of two Y planes is positioned in front of each drift chamber to assist in space point identification for offline reconstruction.

All chambers have Y planes to assist in event reconstruction, as the charged particles are deflected by the magnetic field in the y direction.

Early analysis of the 1984 data showed a large number of high Pt showers. These showers were shown to be produced by muons from beam halo. Consequently, for the 1985 data taking run, a toroidal magnet was placed in the beam line 80 metres upstream from the target, in an attempt to deflect the halo outside the calorimeter. In addition, several counters were placed upstream to detect the muons. Thus, by using these halo counters and routines used to detect halo showers in the calorimeter, the halo contamination of the direct photon signal

in the 1985 data was negligible.

## 2.4            *WA70 Calorimeter and 4m Chamber*

*Apparatus specially constructed for this experiment*

### 2.4.1        4m Chamber

Positioned approximately 10 m from the centre of the Omega magnet and immediately in front of the electromagnetic calorimeter was a large 4m x 4m MWPC, which was needed to identify charged particles, particularly electrons. The chamber has four planes of wires UYVZ, with the angles of the Y, U and V planes as described previously and the Z plane wires orthogonal to the Y plane wires. The planes are separated by 4 cm in the beam direction and the wires in each plane have 4 mm spacing. The efficiencies of the planes of this chamber are discussed in more detail in Chapter 4.

### 2.4.2        Electromagnetic calorimeter

Immediately behind the 4m chamber was the electromagnetic lead-liquid scintillator sampling calorimeter. The calorimeter is divided into four identical quadrants, each of which has three segments numbered 1 to 3 in the beam direction. The quadrants are segmented in this way to assist in the identification of hadrons.

Each segment consists of ten layers of teflon tubes, containing liquid scintillator, interleaved with 5.2 mm thick lead sheets. The layers of tubes are arranged alternately in the y and z directions. The tubes are 2.4 m long and have an inner diameter of 4.4 mm and 0.4 mm wall thickness. The tubes were

embedded in epoxy with 0.15 mm thick stainless steel bands placed between every other tube to provide rigidity. Fibreglass sheets, 0.2 mm thick, were placed on top of each layer of tubes (Fig. 2.2). There are three hundred and eighty four tubes in each layer, giving an active surface area of  $205.4 \times 205.4 \text{ cm}^2$  per quadrant. After stacking the layers of tubes and lead sheets, each segment was then placed in an aluminium frame and enclosed in a stainless steel skin.

In constructing a quadrant, three segments were interleaved with four polypropylene sheets containing the tracks for the source calibration system and epoxy bags were placed between the segments to make up for any irregularities in the segment faces. Finally, 15 cm foam-aluminium sandwich compression modules were placed on either side of the quadrant to take up the strain due to the hydrostatic pressure of the liquid scintillator. The total amount of material is 24 radiation lengths (Fig. 2.3).

The light produced in the scintillator travels by total internal reflection to the light collection system which is positioned on the outer edges of the quadrants. The aluminium frame contains quartz windows which view the ends of the teflon tubes. In the inner half of segments 1 and 2, there are ten teflon tubes viewed by each window and on the outer half of segments 1 and 2 and all of segment 3 there are twenty tubes per window. This corresponds to a grouping of two or four teflon tubes from each of the five layers. This results in both views in segments 1 and 2 each having ninety six narrow channels of width 1.07 cm and forty eight wide channels of width 2.14 cm. Segment 3 has only ninety six channels per view, all of width 2.14 cm.

The light from each quartz window passes through a 15 cm long perspex lightmixer into a photomultiplier tube (PM) (Fig. 2.4) [23]. The PMs (XP2972) were specially constructed by Philips for the calorimeter. The voltage supply to the 3072 PMs was produced by twelve Lecroy (1440) mainframe high voltage supply units. The voltage to each PM could be monitored and set to a nominal

accuracy of 2.5 V by computer. The anode signals from the PMs are connected to charge integrating (LeCroy 2282C) ADCs in the WA70 experimental counting room. Online pedestal subtraction was performed and only channels with greater than 5 ADC counts were read out, together with the two neighbouring channels on either side.

## 2.5 *Trigger*

The trigger logic accepted events which were a combination of two separate triggers, the interaction trigger and the calorimeter trigger [24].

### 2.5.1 Interaction Trigger

This trigger selected beam particles which had interacted in the hydrogen target.

A particle entering the target was identified by a coincidence of five beam counters positioned upstream from the target. These consisted of two scintillation counters  $S_1$  and  $S_2$  and three veto counters  $V_1$ ,  $V_2$  and  $V_3$  on the beam line. A clean beam signal was defined as  $S_1.S_2.\bar{V}_1.\bar{V}_2.\bar{V}_3$ . There were also two anticoincidence counters  $A_1$  and  $A_2$  downstream from the calorimeter, to detect whether the particle had interacted in the target. Thus, the interaction trigger was defined by  $S_1.S_2.\bar{V}_1.\bar{V}_2.\bar{V}_3.(\bar{A}_1+\bar{A}_2)$ .

### 2.5.2 Calorimeter trigger

The function of this trigger was to identify high Pt showers in the calorimeter.

Due to the construction of the calorimeter, the main problem in triggering

on high Pt showers was the matching of the shower profiles detected in the two views. The solution to this problem was to divide each quadrant into four strips per view which produced sixteen trigger cells. The arrangement of these trigger cells is shown in Fig. 2.5. The cells were overlapped by one channel in each view to avoid splitting the energy of a shower between two cells.

The PM outputs were weighted by a resistance depending on the angle of the PM relative to the beam to give a signal proportional to the transverse momentum. All the outputs in a given strip were then added to give the transverse momentum measured in the strip.

A three level trigger check was then performed on the signals from these strips;

- (1) The first level trigger selected events where the transverse momentum in any of the strips in the calorimeter was above a given threshold.
- (2) The second level check was performed on the individual cells. In calculating the energy deposited in a given cell, it is assumed that all the energy from both of the overlapping strips came from that particular cell. This obviously overestimates the energy deposited in each cell, but ensures that no high Pt events are lost.

The first level signals from the y and z strips were digitised by flash ADCs. For each cell an estimate of the attenuation in both views was calculated.

Three checks were then performed on each cell ;

- (i)  $\sqrt{(\text{Pt}^2(\text{y strip}) + \text{Pt}^2(\text{z strip}))} > \text{Pt}_1,$
- (ii)  $\text{Pt}(\text{y strip}) > \text{Pt}_2 \text{ and } \text{Pt}(\text{z strip}) > \text{Pt}_2,$
- (iii)  $|\text{E}_y - \text{E}_z| / (\text{E}_y + \text{E}_z) < \text{ASYM},$

where  $\text{Pt}_1$ ,  $\text{Pt}_2$  and ASYM were all fixed limits depending on the trigger setting.

There were four different trigger types ;

- (a)  $Pt > 3 \text{ GeV}/c$ ,
- (b)  $Pt > 4 \text{ GeV}/c$ ,
- (c)  $Pt > 1.8 \text{ GeV}/c$ , and
- (d) Showers with  $Pt > 1.8 \text{ GeV}/c$  in both quadrants 1 and 3.

Obviously, trigger type (d) demanded that two cells passed the level 2 checks. This trigger was intended to detect electron pairs from  $J/\psi$  decay. The detection of this particle was intended to provide a useful check in calibration (Chapter 5).

(3) The third level trigger carried out the same check as level 2 on smaller strips. The calculations were performed by a microprocessor system (MICE) [19] which could be used in either flagging or rejection mode. If MICE was in flagging mode, a flag was set showing whether a given cell had passed the cuts. In rejection mode, if all the candidate cells failed the cuts then the event was rejected. The  $Pt$  threshold for MICE corresponding to the  $3 \text{ GeV}/c$  level 2 trigger threshold was set at  $1.5 \text{ GeV}/c$  to ensure that high  $Pt$   $\pi^0$ 's and  $\eta$ s were retained.

Although the four different trigger threshold settings were possible, the data were taken using only trigger types a, b and d.

## 2.6        *Time of Flight (TOF)*

Time of flight electronics [25] are connected to each of the 1152 channels in the first segment of the calorimeter's four quadrants to resolve position ambiguities resulting from the orthogonal geometry of the calorimeter described in the previous section. This system provided additional positional information for the offline analysis program by measuring the travel time of the light down the scintillator tube to the PM, and enabled the rejection of overlapped events.

The TOF circuitry was driven by the signal from the second last dynode of the PMs. This signal was then amplified and passed to a discriminator. A long delay cable between the discriminator and the ADCs allowed a decision time of up to 375 ns for the Trigger to accept or reject the event. If the event was accepted, by the Trigger, the ADC gate was opened by the PM signal and was stopped by a signal from the S<sub>2</sub> beam counter.

The TOF system was calibrated both by using the laser calibration system (Chapter 2.6) and real data. The laser data were taken with and without a 10 ns cable delay in the stop signal. Since the laser system simultaneously fires all of the TOF channels this method provides information on the relative timing of all the channels. These laser runs were performed every few days during the experiment.

Corrections had to be made for the jitter in both the start and stop signals. The variation in the start signal was a function of the pulse height. This was corrected by using an electron test beam to provide data over a range of pulse heights. The jitter in the stop signal was reduced in each event by using information from showers whose position can be unambiguously identified by a pattern recognition program.

The final system achieved a resolution of around  $\pm 5$  cm for electromagnetic showers of energy greater than 10 GeV.

## 2.7        *Online Calorimeter Calibration*

The calorimeter has two independent methods of calibration [26], one based on a N<sub>2</sub> laser and the other using sixteen <sup>60</sup>Co sources.

### 2.7.1      Calibration Systems

#### 2.7.1.a     Laser System

The system (Fig. 2.6) was fired by a N<sub>2</sub> laser which provides 4 ns FWHM, 10 mJ pulses of UV light. A beam splitter diverts approximately 8 % of this light by optical fibre to a photomultiplier which acts as the trigger for the system. The remainder of the light passes through a selection of up to seven quartz filters and is focussed by quartz lenses onto a quartz cell filled with stilbene and methanol. The purpose of this cell is to provide light which closely matches the scintillator light produced in real data. The output from the cell is fed to a plastic light mixer to provide a light intensity output which varies by less than 1 % across its surface. The incoherent light then passes into one of five bunches of twenty five plastic fibres, and one of these fibres transmits light to two reference PMs. Each of the remaining fibres is connected to one of twenty four barrettes which are situated on the inner edges of the quadrants (Fig. 2.7b). Each barrette contains one hundred and forty four quartz fibres (ninety six in segment 3) which have a diameter of 125  $\mu\text{m}$  (Fig. 2.7a). These fibres inject the light into the teflon tubes. Thus, by altering the illuminated bunch of fibres, this system can provide five different measurements for each PM.

#### 2.7.1.b     Radioactive Source System

The source system consists of sixteen <sup>60</sup>Co sources whose positions in the calorimeter can be individually adjusted by computer. Each quadrant has four source plates which are situated in front of segment 1, between segments 1 and 2,

between segments 2 and 3, and behind segment 3.

Each source is attached to a plastic covered wire chain and runs round a track (Fig. 2.8) which has been cut in the 9 mm thick polypropylene source plate (Chapter 2.4.2). The source drive system is shown in Fig. 2.9 and the control system in Fig. 2.10. The long straight sections of track are c. 30 cm and c. 170 cm from the PMs. (These positions are referred to as 'level 1' and 'level 2' respectively). This arrangement of sources provides four different measurements for each PM, using front and back sources, and level 1 and level 2 information.

In addition to providing relative PM calibration data, this system can also be used to measure the attenuation of light in the teflon tubes.

Unfortunately, since in each view the PM signals are measured sequentially, a full source scan takes about twenty four hours to complete.

## 2.7.2 Calibration method

During the 1984 run, the PM voltages were set by the laser calibration system. The voltages on the PMs were corrected at approximately two week intervals and in addition the gain drifts were monitored by laser runs which were performed every two days.

Source calibration information was not used during the 1984 run to adjust the voltages. However, two source calibration runs were performed at the beginning and the end of the run.

When the source calibration data were analysed, after equalisation with the laser system, it showed that the laser had introduced systematic variations in the setting of the gains of the PMs. In particular, moving away from the calorimeter centre, most views had a systematic decrease in gain of around 15 % over 2m, and there was also evidence of steps or discontinuities between the wide and

narrow channels in segments 1 and segments 2 (Chapter 5.1). These effects are thought to be due to light attenuation in the quartz fibres in the barrettes and misalignment of the fibres with the teflon tubes. Both of these effects were also seen in the experimental data, and so the source calibration data were used for offline correction.

In the 1985 data taking run the source calibration system was used to set PM voltages and three source scans were performed during breaks in the run.

The final offline energy scale calibration for both runs was provided by studying the  $\pi^0$  and  $\eta$  masses.

## 2.8        *Data Acquisition System (DACP)*

Two VAX 780 computers were used to record the experimental data. The main data taking computer was the 'Omega' VAX which recorded on magnetic tape all events which were passed by MICE. The other computer, the 'Geneva' VAX, was used to record subsets of events of particular interest, for example those containing a very high Pt shower.

The information written to tape included the calorimeter ADCs, trigger type, TOF data, the digitisations in the various wire chambers and CEDAR information. In addition, various scalers were recorded, which monitored beam condition and interaction rates.

The two VAX computers were also used to run control and monitoring programs. The control programs could be used to adjust for example the high voltage supplies to the calorimeter PMs or alter the trigger type or Pt threshold. The monitoring programs provided online information on the performance of the calorimeter, TOF system and Omega wire chambers.

*Figures - Chapter 2*

Fig. 2.1

The layout of the WA70 experimental system.

Fig. 2.2

The construction of a layer of teflon tubes in the photon detector.

Fig. 2.3

Details of the geometry and construction of the photon detector.

Fig. 2.4

Connection of the Photomultiplier tubes to the ends of the teflon tubes.

Fig. 2.5

The area on the front face of a quadrant covered by the sixteen trigger cells.

Fig. 2.6

The laser calibration system.

Fig. 2.7a

Arrangement of quartz fibres within a barrette.

Fig. 2.7b

Positioning of barrettes in a quadrant.

Fig. 2.8

Shape of track used by the source calibration system.

Fig. 2.9

Drive mechanism for the source calibration system.

Fig. 2.10

Source calibration control system.

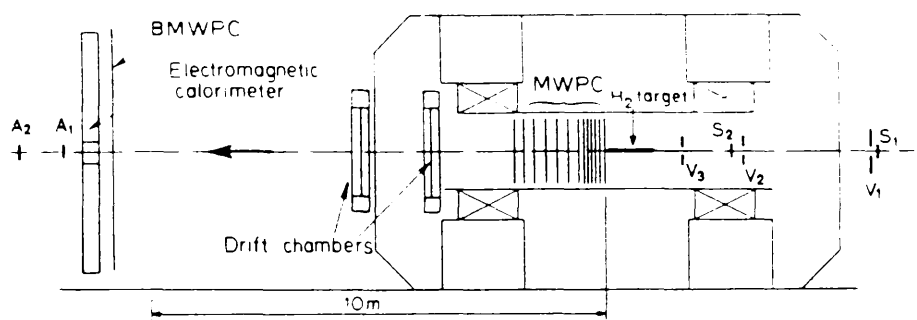


Fig. 2.1

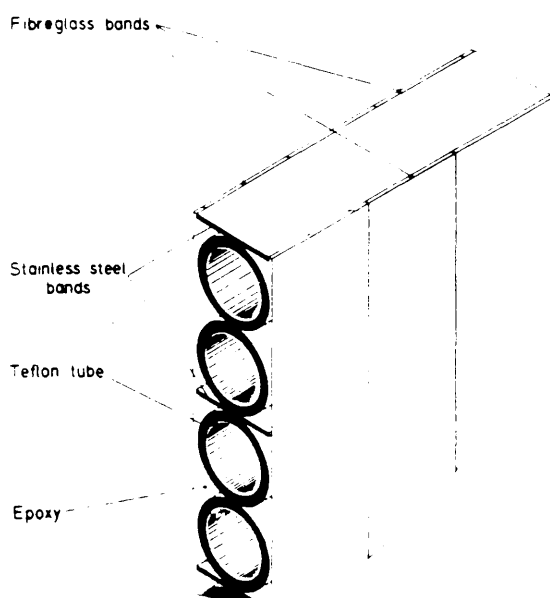


Fig. 2.2

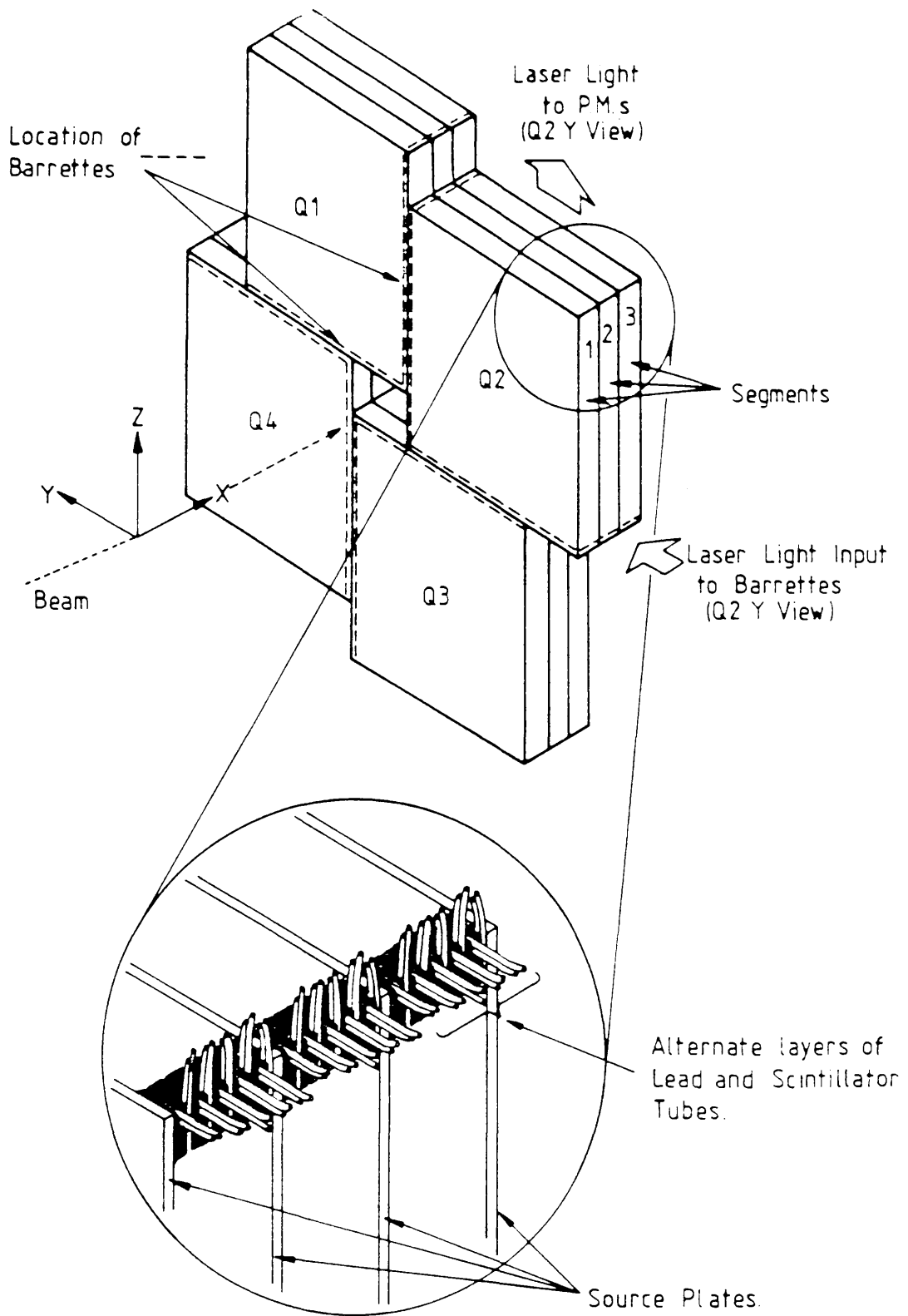


Fig. 2.3

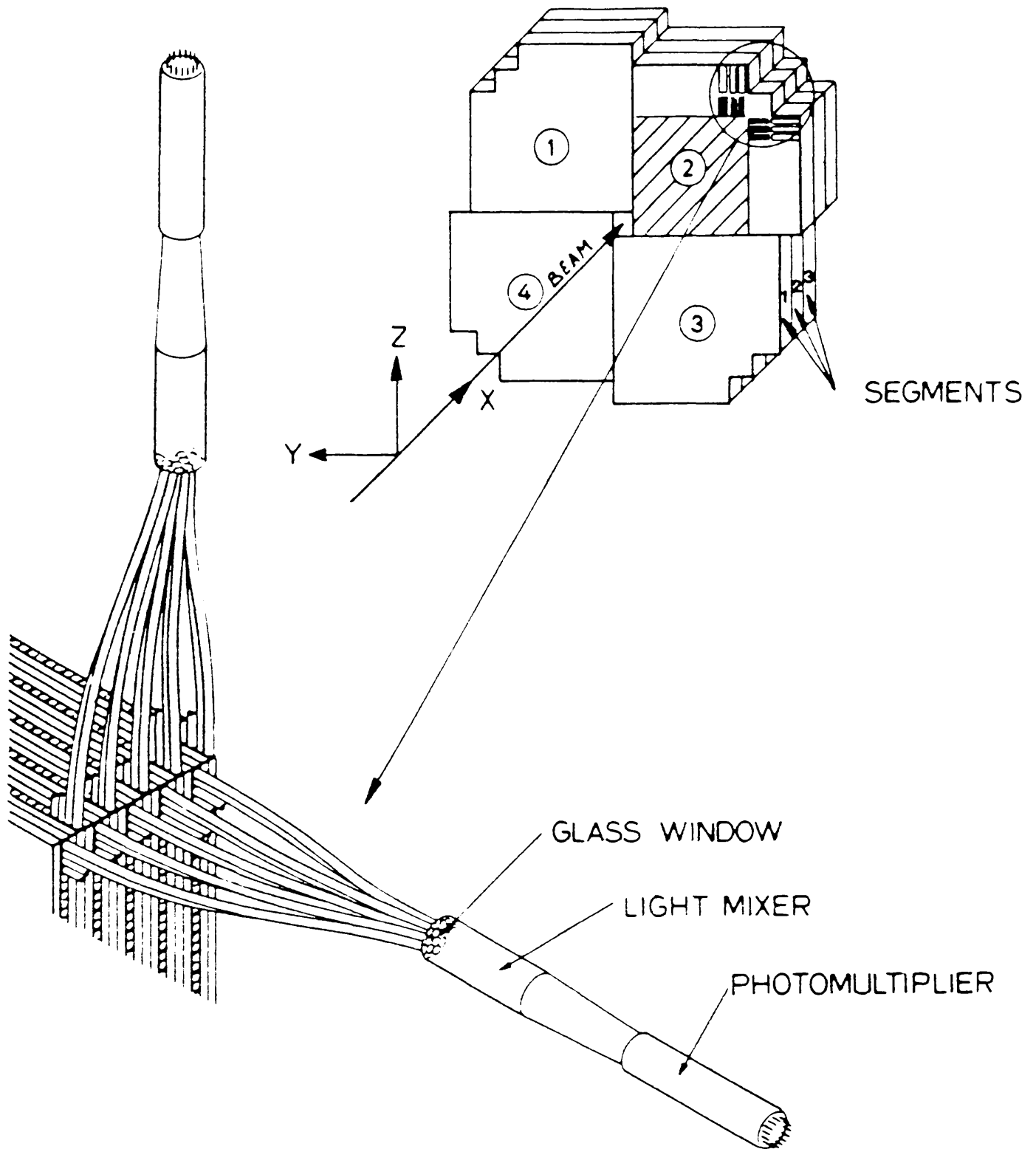


Fig. 2.4

\* Beam

1	2	3	4
5	6	7	8
9	10	11	12
13	14	15	16

Fig. 2.5

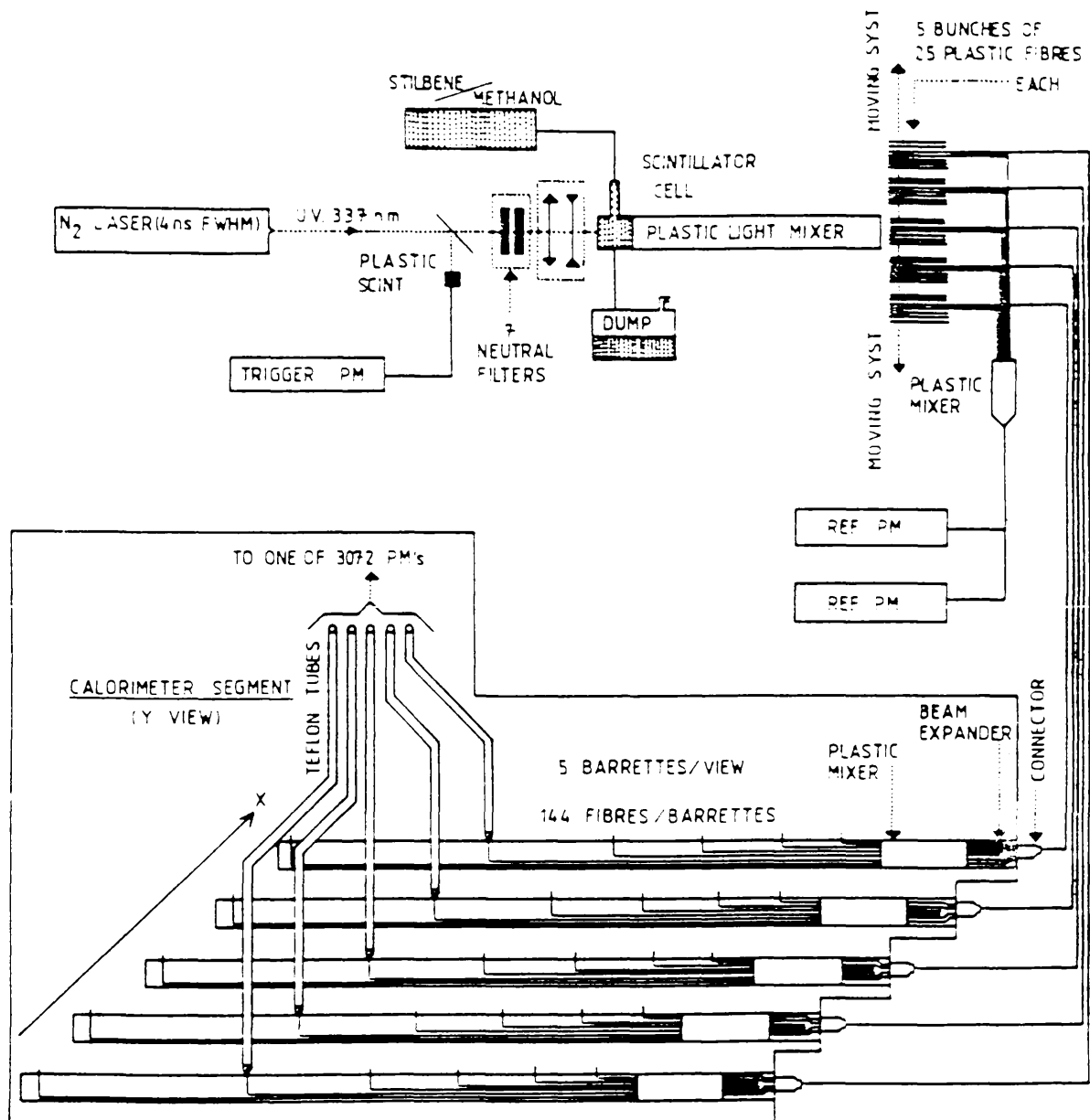


Fig. 2.6

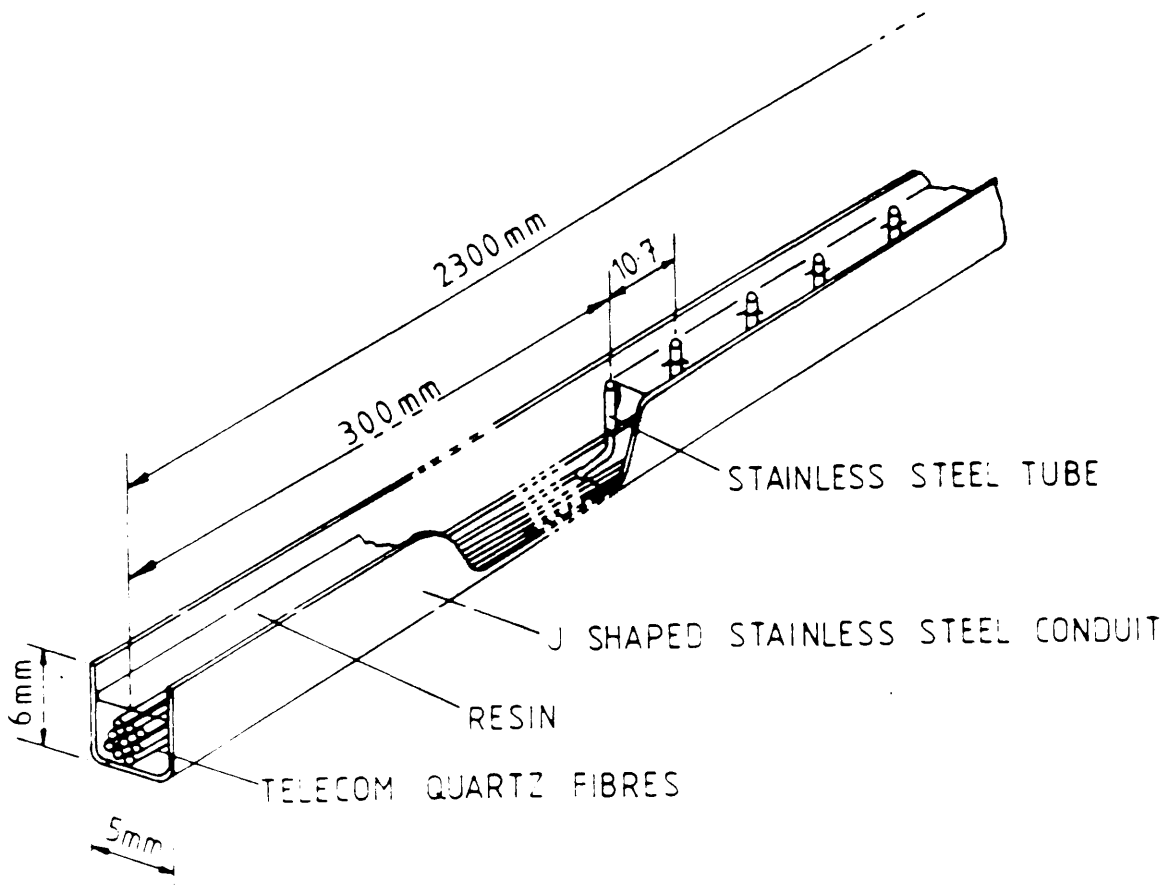


Fig. 2.7a

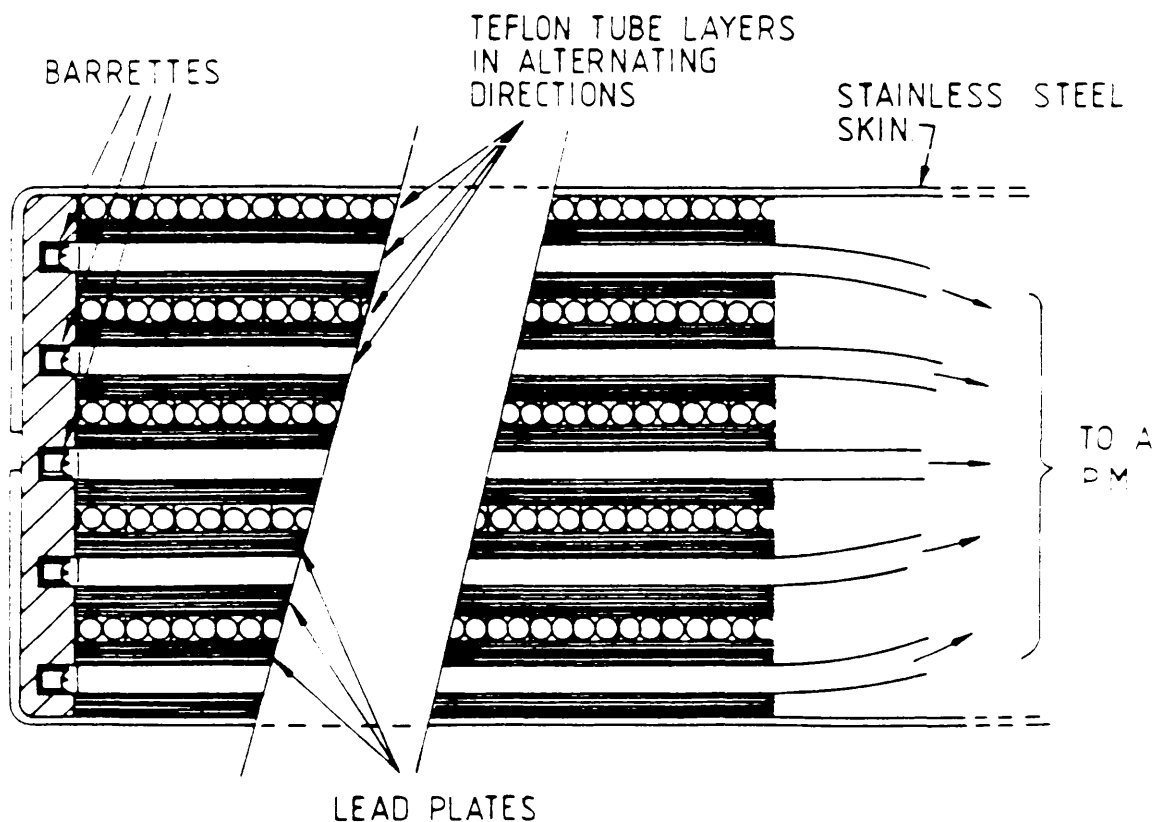


Fig. 2.7b

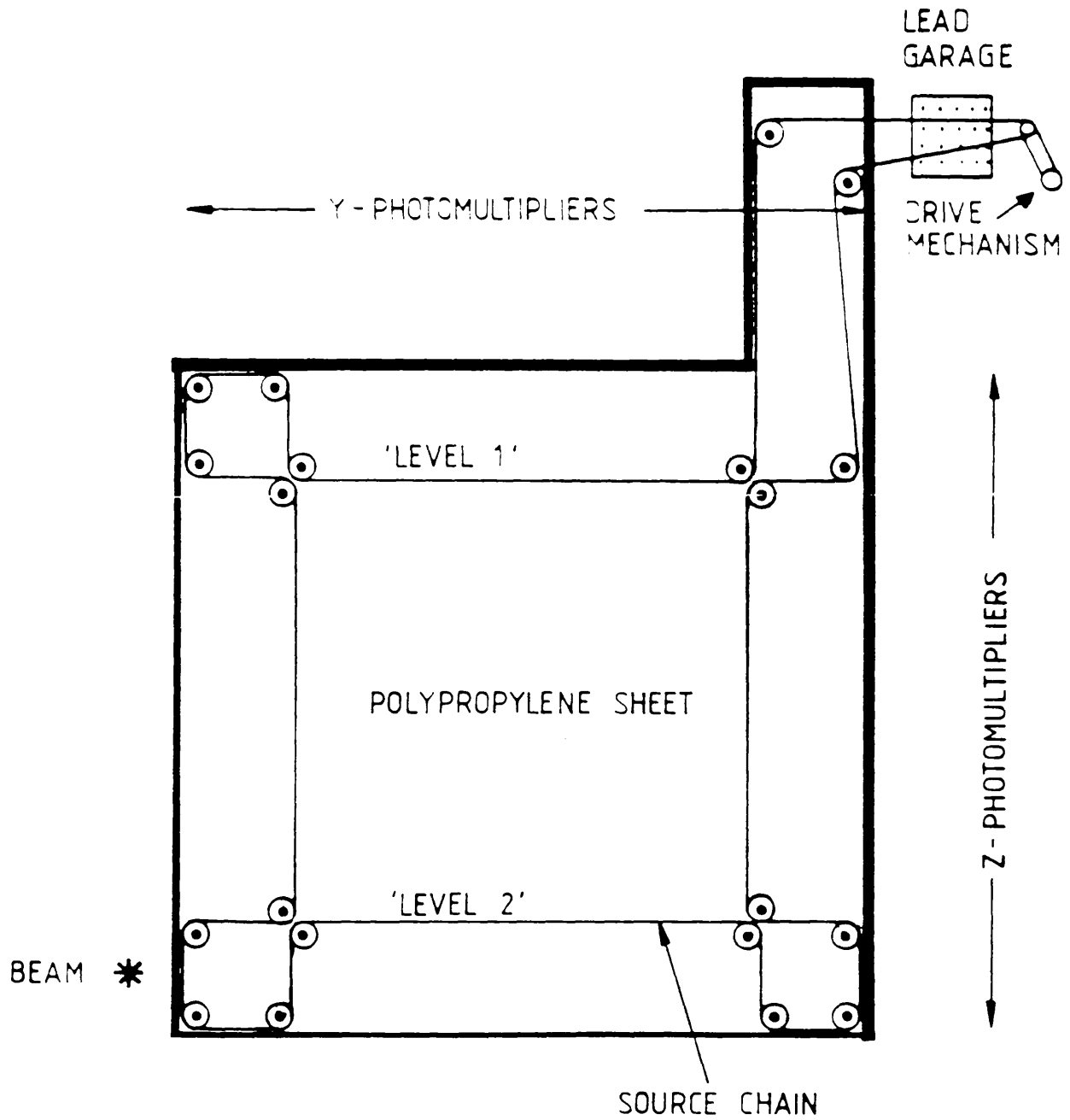


Fig. 2.8

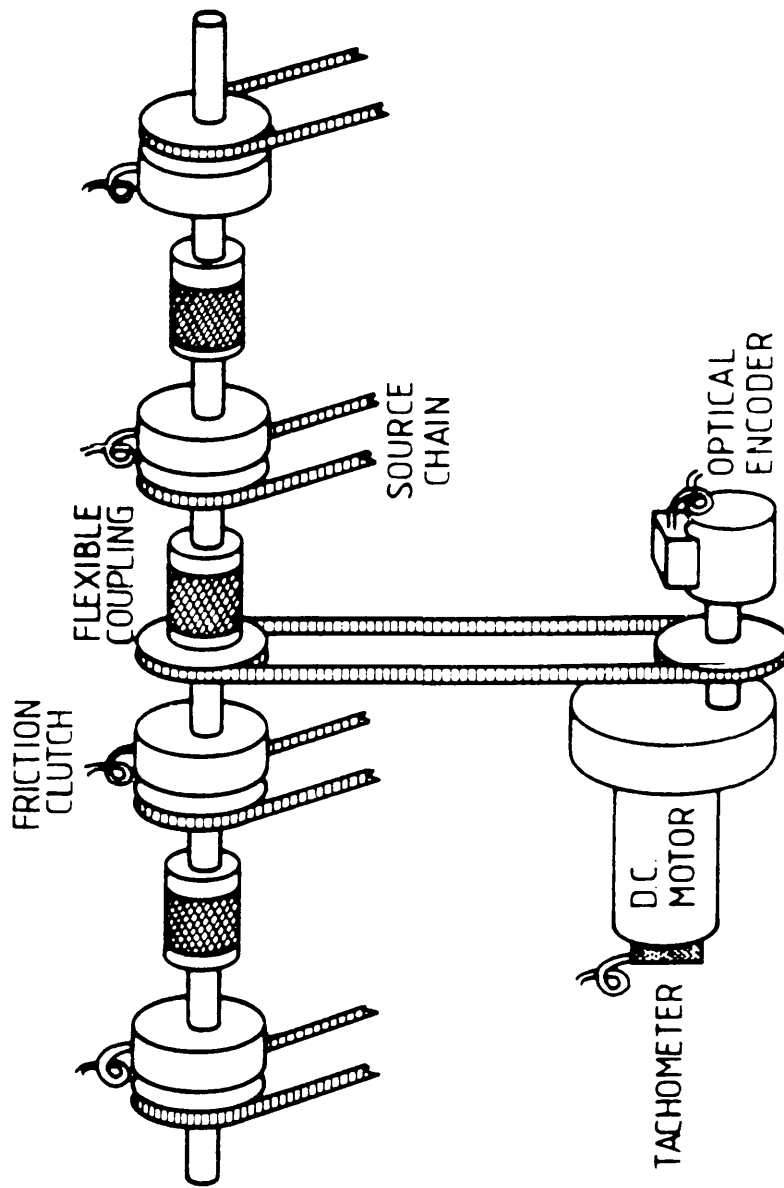


Fig. 2.9

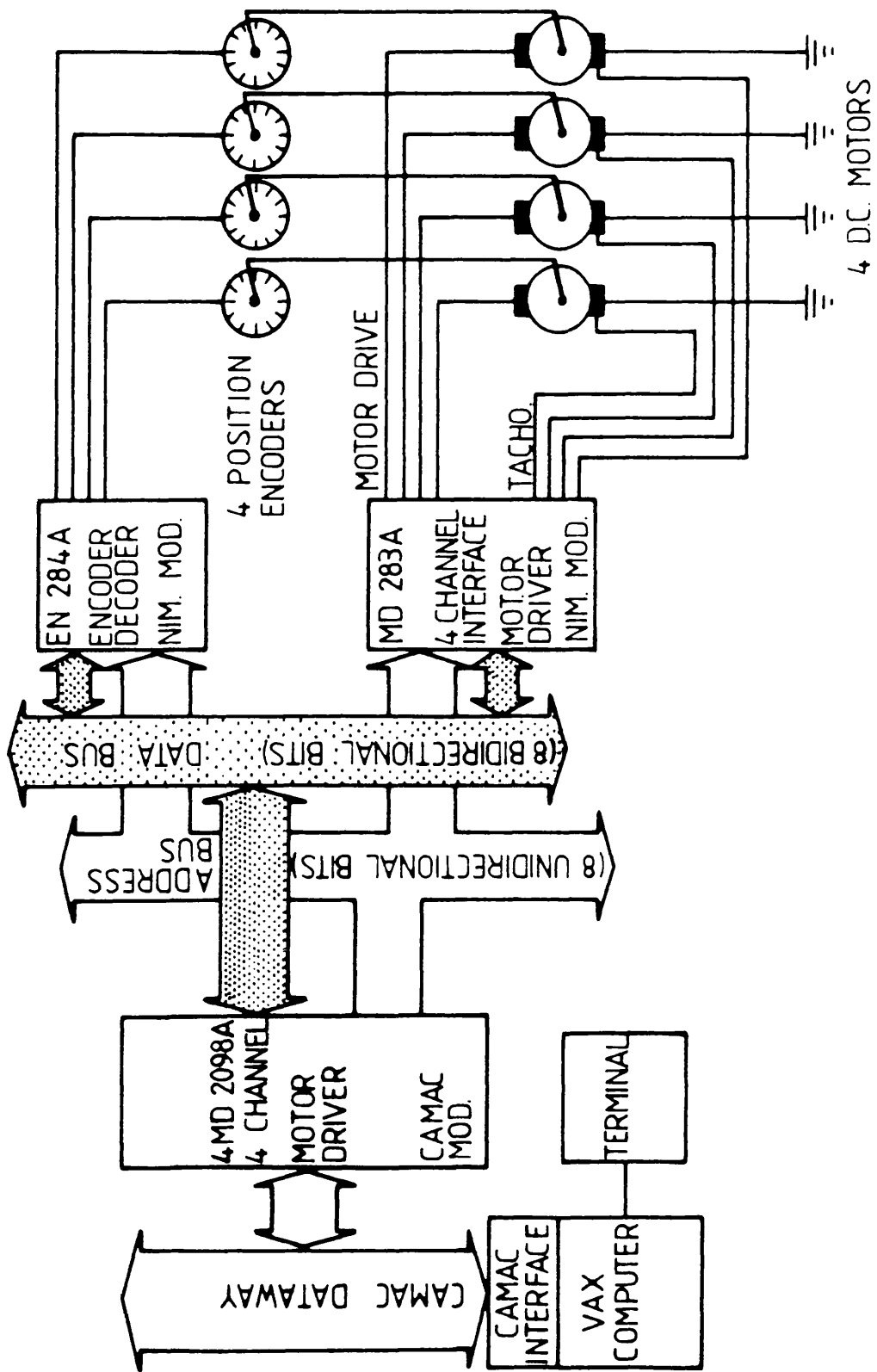


Fig. 2.10

## CHAPTER 3

### *Offline Event Reconstruction.*

#### 3.1      *Introduction.*

To analyse the physics of an event with the information obtained from the calorimeter and wire chambers, it is necessary to run reconstruction programs on the raw experimental data. In the WA70 experiment there were two programs used for this purpose. A pattern recognition program was used to reconstruct the showers in the calorimeter and then TRIDENT [27] was used to reconstruct charged particle tracks in the wire chambers. This chapter describes the main philosophies behind each program.

#### 3.2      *Pattern Recognition*

The offline reconstruction of showers in the calorimeter can be divided into three separate procedures ;

- (1) event selection,
- (2) one dimensional shower reconstruction,
- (3) two dimensional matching.

Different programs were used for the pattern recognition of the 1984 and 1985 data taking runs. In 1984, the program initially used was PATREC and in 1985, GLOBAL. As both programs used the same procedure in their one dimensional shower reconstruction and only differed in their method of matching the showers in the two orthogonal views, only section (3) needs a separate description for PATREC and GLOBAL.

### 3.2.1 Event Selection

Before attempting to reconstruct the calorimeter showers, various corrections and checks have to be performed on the data.

At the start of each new data tape, the first two hundred events are checked for any pedestal drift since the last tape. If a noticeable drift is observed then the pedestals are corrected accordingly.

An offline version of MICE is called. This is needed for two reasons;

- (i) to select events which were recorded when MICE was in flagging mode,
- (ii) the offline MICE analyses up to six possible trigger cells compared with two cells in the online version.

A 'PM correction' file is then called to assign readings to various PM channels which were identified as faulty from the source scan data. In this program, the ADC value for each of these channels is set to the geometric mean of its neighbours.

The data are then corrected by various calibration files. As mentioned in Chapter 2, a source calibration file is used in the 1984 data to correct for the systematics produced by the laser system. For both sets of data, laser calibration files were generated by laser runs performed every few days during the run. These files are used to correct for drifts in the PM gains.

In addition, in the 1985 data, the attenuation length factor and equalisation slope are individually corrected for each quadrant to minimise the  $\pi^0$  width and E(y)-E(z) distributions across the quadrant.

The remaining event rejection is performed using the TOF system (Chapter 2.6). The stop signal from the S<sub>1</sub> beam counter is used to check for event pile-up. There are two ways this pile-up appears in the data ;

(i) a simple matching of showers is performed and the difference between the shower position predicted by the TOF and the measured position is plotted. Usually these shifts are grouped around a single value, but there are also events with two or more apparent  $S_2$  timings. These 'double' events are rejected.

(ii) a large number of showers have no TOF value. This effect is produced by the second event occurring after the stop signal from  $S_2$  has reached the counters. A cut is made on events with greater than two such channels.

A cut is also made on showers which have a single  $S_2$  timing, but the value is  $> 200$  cm or  $< -50$  cm. Further tests are then applied to the highest Pt shower in each trigger cell. The highest ADC channel in segment 2 is located and the channels in front of this, in segment 1, are searched. DTOF is then calculated, given by;

$$\text{DTOF} = (y - T_z) - (z - T_y)$$

where  $y, z$  are the measured shower coordinates and  $T_y, T_z$  the coordinates given by the TOF. If no signal is found or the signal is too small to give a TOF signal then the cell is rejected. Also, if  $\text{DTOF} > 40$  cm or either  $T_y$  or  $T_z$  is greater than 200 cm the trigger is rejected as being due to a shower in the light guide.

These 'good' trigger events are then passed to the shower reconstruction routines.

### 3.2.2 One dimensional Reconstruction

At all times, the four quadrants are treated separately and initially the three segments are also analysed individually. The program searches for the channel with the highest ADC value in a segment and constructs the shower to right and left until a minimum is reached. The highest non-assigned ADC value is then used to begin the construction of the next shower and this process is repeated until the highest remaining ADC count is less than 10 in segments 1 and

2 and less than 5 in segment 3.

The showers in each view of the individual segments are now associated. The process begins with the segment 3 showers. These are extrapolated into segment 2 and a search is made for a nearby shower. If no nearby shower is found, then the shower exists only in segment 3. However, if a matching shower is found in segment 2, then the two showers are associated and the search is continued into segment 1. After all the segment 3 showers have been analysed, the unassigned segment 2 showers are then used to search in segment 1. The final result gives for each shower the total ADC, the y or z coordinate, a mean longitudinal position (barycentre), and also TOF information, provided the shower exists in segment 1.

An attempt is now made to correct for overlapped showers and to divide the energy between the showers. In segments 1 or 2 if the double shower has only one peak visible, then the positions of the two peaks can be extrapolated from the other segment. The method then used to calculate the energy of each separate shower is to divide the energy deposited in the region between the two peaks in proportion to the energy contained in the two external regions. The energy in the third segment is then divided proportionally to the energies in the first two segments.

At this stage, the energies and coordinates of the showers in each view should be correctly assigned. However, this is not the case for showers which are completely overlapped in all three segments, but these will be corrected when the two dimensional matching is made.

### 3.2.3 Two dimensional Matching.

#### *PATREC*

If there are the same number of showers in each view then PATREC attempts a global match of the single showers. If this fails, then showers are dealt with individually, beginning with the largest energy shower. The main problem with PATREC is that the matching proceeds sequentially and if a shower is wrongly matched this cannot subsequently be corrected.

#### *GLOBAL*

After the 1984 production, a program, GLOBAL, was developed, which analysed all possible combinations of showers in a given quadrant and then chose the best hypothesis based on the amount of unassociated energy and the total chi-squared of the hypothesis.

To choose which version of pattern recognition would be used in the 1985 production, the two programs were run on the same samples of real and Monte Carlo data to check their ability to reconstruct  $\pi^0$ 's. In each case, GLOBAL was more efficient in reconstructing  $\pi^0$ 's and so was chosen as the new pattern recognition program. At this stage the 1984 data was also reprocessed through the GLOBAL program.

GLOBAL attempts to match the showers in the two profiles, by using the energy, TOF and barycentre information to produce a chi-squared for each match. The program allows any individual shower in one view to be matched with one, two or three showers in the other view. A total chi-squared can then be calculated for each possible permutation. Also, since showers can be left unmatched in certain hypotheses, the unassociated energy is also calculated.

The best fit is then chosen as the combination with the least unassociated

energy. If this is equal for different permutations, then the one with the lowest chi-squared per degree of freedom is chosen. It is not sufficient to use the total chi-squared, since for different permutations there will be a different number of individual matches contributing to the total chi-squared.

The shower matching finally chosen is known as the primary hypothesis. In addition, secondary hypotheses are kept which are similar to the primary hypothesis in unassociated energy and chi-squared.

After the pattern recognition program has been run on the data, information is available on all the showers in the calorimeter. At this stage, this type of data is known as DST1. DST2s are produced by running TRIDENT on the DST1 tapes. To save computing time, the calorimeter shower information is used to select interesting events to pass through TRIDENT. These interesting events include all possible high Pt direct photons,  $\pi^0$ 's and  $J/\psi$ s.

### 3.3        *TRIDENT*

The aim of the TRIDENT program is the full event reconstruction from charged tracks recorded in the Omega Particle Detector system. The digitisings from the A and B MWPCs, the drift chambers and the 4m chamber were used to reconstruct tracks, determine the event vertex and calculate the momenta of the tracks.

The track recognition process used by TRIDENT is basically a three dimensional track following technique. The search for tracks begins in the two lever arm chambers. Usually, the lever arm chambers are the two drift chambers, however, as mentioned in Chapter 2, in the 1984 data taking run there was only one drift chamber present, so the 4m chamber was used as one of the lever arm chambers.

At the upstream end of each drift chamber there is a chamber consisting of two Y planes. These chambers are used to define 'roads' in the lever arm chambers, to reduce the problems produced by a large background in the drifts. When using the 4m chamber as a lever arm chamber, the Y plane was used for this purpose. These roads are produced by combining the hits in the four Y planes and searching for combinations of three or four planes which define a road. The search for the tracks in the lever arm chambers is then restricted to the regions predicted by the roads.

Both a 'space points' approach and a 'global' approach are used to search for tracks in the lever arm chambers. The space points approach combines the digitisings in all four planes of each lever arm chamber to construct track elements. They must satisfy prescribed slopes in x,y and x,z and also the constraint relation :

$$2y\cos A - u - v = 0 \quad (1)$$

where A is the angular displacement of the U and V planes and y,u,v are the coordinates in the Y,U and V planes.

The track elements in each chamber are then linked and each straight line must have a slope in agreement with the local slopes. In addition, the tracks must point to the target in the x,z projection. This method does not tolerate any chamber inefficiencies.

The global approach deals with the two chambers simultaneously. First, the y planes are combined to make strings of three or four measurements. Then, using equation (1), the u and v coordinates are investigated to construct with the y coordinates a straight line in space. This method can tolerate up to two missing coordinates out of eight.

The tracks found in the lever arm chambers are then extrapolated into the

last four A chambers, where digitisings are assigned to create new tracks. These tracks are created by combining the digitisings in the Y planes of the chambers to define arcs of a circle. Cuts on the slope of segments and curvature are applied. For each chamber and a given y coordinate, the u,v combinations compatible with (1) are looked for, allowing z :

$$2z\sin A = v - u$$

to be derived. Only the u,v combinations giving rise to z's in a straight line are kept.

The tracks are then extrapolated into the next chamber as before, and the digitisings assigned to the tracks. The process of extrapolation and creation is continued until all the A and B chambers have been examined. The track momenta are then calculated using a quintic spline as a model for the track.

For both sets of data, the 4m chamber was used as an extra chamber. This means that the final tracks from the Omega chambers are projected to the 4m chamber and a local search is made for space points. If a three or four plane space point is found within the area searched, this is assigned to the track, which is then refitted. Finally, a track is then accepted if it has at least five space points and has a good chi-squared.

To determine the main vertex position, all the tracks are extrapolated back and a chi-squared fit is performed on the projected tracks. All tracks passing within a certain distance of the calculated vertex position are called vertex tracks. All other tracks are referred to as extra tracks. If TRIDENT fails to find a vertex, the x,y,z coordinates of the vertex are set to -50.0 cm, 0.0, 0.0 respectively.

*a) 1984 Data*

- (i) the tracks had at least eight space points (Fig.4.1a) (45087 tracks),
- (ii) they must end in the drift chamber (10314) or the last Omega wire chamber (24750) and
- (iii) the projected track must hit the sensitive area of the calorimeter (21411).

The number of vertex tracks with at least eight space points and with their last point in the drift chamber seemed very low. This was possibly due to the fact that just before the low intensity data were taken, there had been a technical problem with the drift chamber. Hence, to improve statistics, tracks which ended in the last Omega wire chamber were also accepted for this data sample.

*b) 1985 Data*

- (i) the tracks had at least ten space points (Fig. 4.1b) (48020 tracks),
- (ii) they must end in either drift chamber (23580), and
- (iii) the projected track must hit the sensitive area of the calorimeter (16725).

The TRIDENT tracks were then projected to the calorimeter, and if a shower with energy greater than 1 GeV was found within a radius of 4 cm from the projected hit position, the track was accepted for analysis. In total, there were 4090 of these tracks in the 1984 data (Fig. 4.2a) and 4556 in 1985 (Fig. 4.2b).

This provided a good sample of charged tracks which were reconstructed by

the Omega wire chambers and with a corresponding shower in the calorimeter and hence should also be seen in the 4m chamber.

#### 4.3      *Analysis*

For the selected tracks, the position of the shower in the calorimeter and the coordinates of the last point of the track in the chambers were used to estimate the coordinates of the track in each of the four planes of the 4m chamber. The track was rejected if it did not pass through the region of the chamber covered by all four planes (Fig. 4.3). Fig. 4.4 shows a plot of the distance between the projected hit position and the nearest digitising for the u plane of the 4m chamber, using the 1985 data. Plots for the other three planes of the chamber in both 1984 and 1985 data showed similar distributions. A track was accepted as having given a 'hit' in a plane if the distance to the nearest digitising was less than 4 cm.

In order to use all the information available in the estimation of efficiencies, the tracks were then divided into sixteen categories, depending on which combination of planes registered a hit from a given track (Tables 4.2 and 4.3). Since the efficiency of a wire chamber is known to decrease near the support wires, an additional sixteen numbers were produced, to obtain the efficiencies of the planes away from the support wires. In this case a track is rejected if its projected hit position on any of the four planes was within 3 cm of the nearest support wire (Tables 4.4 and 4.5).

To provide an estimate of the background, the digitisings in the 4m chamber were used from neighbouring events which also contained one or more good track, and the same analysis as above was performed to produce background sets of the sixteen numbers described earlier. These numbers for the relevant data sample are also shown in Tables 4.2-4.5.

**4.4 Fit**

The fit was performed on the thirty two data points, using the following ten parameters :

PU, PY, PV, PZ - the efficiencies of the planes,

BU, BY, BV, BZ - the random digitisings in the planes,

F - the fraction of fake good tracks (This should correspond to the background under the peak in Fig. 4.2),

C - an estimate of the 'correlated' background. This is relevant when an additional background track passes within the 4 cm cut on some of the planes. This background will not be constant for all combinations of planes due to their relative orientation. It is expected that the background contribution in any combination of planes produced by this effect will be proportional to the inverse sine of the half angle between the wires of given planes. Therefore, this background will be highest for the combinations involving the U, V and Y planes. An attempt has been made to correct for this complication by the various RS factors shown in the equations. For each combination of planes, the most likely hit position of the track is assumed to lie on the line bisecting the angle between the wires of the planes registering a hit. The angle between this line and the wires in each plane is then calculated and the inverse sine of half of this angle is used as a weighting factor for that plane. Hence, in the equations, RS10 is equal to the inverse sine of 10.

Thus, the equation used to fit the number of 0 plane hits (CAL(1)) was

$$\begin{aligned} \text{CAL}(1) = & (1-C)\{(F(1-BU)(1-BY)(1-BV)(1-BZ)) \\ & + \{(1-F)(1-PU)(1-BU)(1-PY)(1-BY)(1-PV)(1-BV)(1-PZ)(1-PZ)\}] \\ & + C\{F(1-BU)(1-BY)(1-BV)(1-BZ) \\ & (1-RS25.PU)(1-RS25.PY)(1-RS25.PV)(1-RS20.PZ)\} \\ & + \{(1-F)(1-PU)(1-BU)(1-PY)(1-BY)(1-PV)(1-BV)(1-PZ)(1-BZ) \\ & (1-RS25.PU)(1-RS25.PY)(1-RS25.PV)(1-RS20.PZ)\}] \end{aligned}$$

and for the four plane hits (CAL(16))

$$\begin{aligned} \text{CAL}(16) = & (1-C)\{F.BU.BY.BV.BZ\} \\ & + \{(1-F)(1-(1-PU)(1-BU))(1-(1-PY)(1-BY)) \\ & (1-(1-PV)(1-BV))(1-(1-PZ)(1-BZ))\}] \\ & + C\{F(1-(1-BU)(1-RS5.PU))(1-(1-BY)(1-RS0.PY)) \\ & (1-(1-BV)(1-RS5.PV))(1-(1-BZ)(1-RS45.PZ))\} \\ & + \{(1-F)(1-(1-BU)(1-PU)(1-RS5.PU)) \\ & (1-(1-BY)(1-PY)(1-RS0.PY)) \\ & (1-(1-BV)(1-PV)(1-RS5.PV)) \\ & (1-(1-BZ)(1-PZ)(1-RS45.PZ))\}] \end{aligned}$$

with the other fourteen equations for the one, two and three plane hits similarly constructed.

For the corresponding sixteen background equations, F was set to 1, as there were no genuine tracks.

The main philosophy of the equations is that the tracks which have been classified as 'good', can be divided into two groups, first those which are genuine 'good' tracks, the (1-F) term, and those which are 'fake', the F term. The C parameter represents another track hitting the chamber, which will produce another

form of background in the planes. Thus, the F and (1-F) terms can be divided into two, those with another background track in the analysed region of the chamber, the C term, and those without, the (1-C) term.

In dealing with the individual planes, if there is no digitising in, for example, the U plane, then the terms involved are (1-BU) and (1-PU), and if there is a digitising in the U plane, BU and (1-(1-BU)(1-PU)).

#### 4.5      *Results*

The results of the fit for the four different sets of thirty two numbers are shown in Tables 4.6-4.9 along with the standard deviation on the first sixteen data points. For numbers 17-32, the background, the fit was not expected to follow the data accurately, as the correct parametrisation of the background would have required extra parameters.

The efficiencies for the planes are shown in Tables 4.10 and 4.11. These tables clearly show that with the exception of the Z plane, the efficiencies were all significantly lower for the 1985 run. The cause of this is not known, since an attempt was made at the start of the 1985 run to plateau the planes.

If the individual planes are used to calculate the probability of a charged track producing a three or four plane hit, the efficiencies are  $89 \pm 2\%$  in 1984 and  $85 \pm 2\%$  in 1985. An independent method was used to calculate these efficiencies using candidate direct photon events (Chapter 6.3.2). This produced efficiencies of  $85 \pm 2\%$  in 1984 and  $81 \pm 2\%$  in 1985. So, both methods independently show a similar drop in the efficiency of the 4m chamber between the two runs.

The results clearly show that in all cases, the efficiency of the z plane is significantly lower than the other planes. This was probably produced by a

hardware problem, since prior to the 1985 data taking run a satisfactory plateau for the z plane could not be found.

*Table 4.1*

Plane	Limits(cm)		Angle
u	-176.4	233.1	10.14
y	-205.2	204.4	0.0
v	-233.1	176.4	-10.14
z	-205.2	204.4	90.0

Table 4.2 (1984 Data)		
Planes hit	Real events	Background
0	15	1847
u only	15	344
v "	21	272
y "	7	220
z "	95	485
uv "	72	57
uy "	97	91
uz "	64	136
vy "	49	100
vz "	67	69
yz "	55	58
uvy "	577	106
uvz "	219	29
uyz "	211	35
vyz "	184	42
uvyz	2210	67
Total	3958	3958

*Table 4.3 (1985 Data)*

Planes hit	Real events	Background
0	18	2109
u only	27	386
v "	29	260
y "	30	232
"	103	614
uv "	91	75
uy "	101	124
uz "	94	139
vy "	72	121
vz "	90	77
yz "	86	73
uvy "	567	80
uvz "	294	23
uzy "	382	37
vyz "	241	43
uvyz	2238	70
Total	4463	4463

*Table 4.4 (1984 Data)*

Planes hit	Real events	Background
0	4	1066
u only	6	191
v "	9	211
y "	1	160
z "	8	229
uv "	39	40
uy "	63	63
uz "	15	54
vy "	26	80
vz "	11	57
yz "	16	44
uvy "	342	82
uvz "	134	27
uzy "	124	28
vyz "	93	34
uvyz	1533	58
Total	2424	2424

*Table 4.5 (1985 Data)*

Planes hit	Real events	Background
0	6	1209
u only	11	216
v "	11	194
y "	19	175
z "	19	296
uv "	52	58
uy "	58	94
uz "	47	49
vy "	34	95
vz "	33	58
yz "	41	59
uvy "	321	57
uvz "	160	15
uzy "	244	28
vyz "	136	33
uvyz	1498	54
Total	2690	2690

*Table 4.6*

No.	Data	Fit	SD
1	15.0	23.2	2.12
2	15.0	9.0	1.54
3	21.0	7.4	2.97
4	7.0	7.4	0.14
5	95.0	69.5	2.61
6	72.0	73.6	0.20
7	97.0	75.9	2.14
8	64.0	32.4	3.96
9	49.0	62.0	1.85
10	67.0	26.3	4.98
11	55.0	26.3	3.87
12	577.0	636.3	2.47
13	219.0	275.3	3.81
14	211.0	274.3	4.36
15	184.0	222.7	2.86
16	2210.0	2334.1	2.64
17	1847.0	1953.2	
18	344.0	431.5	
19	272.0	328.1	
20	220.0	267.6	
21	485.0	579.2	
22	57.0	64.9	
23	91.0	109.0	
24	136.0	114.6	
25	100.0	91.9	
26	69.0	86.0	
27	58.0	71.1	
28	106.0	37.0	
29	29.0	20.7	
30	35.0	15.7	
31	42.0	11.9	
32	67.0	11.8	

*Table 47*

No.	Data	Fit	SD
1	18.0	26.2	1.93
2	27.0	19.0	1.54
3	29.0	13.1	2.95
4	30.0	16.0	2.56
5	103.0	79.6	2.31
6	91.0	93.5	0.26
7	101.0	119.0	1.79
8	94.0	71.1	2.36
9	72.0	81.9	1.17
10	90.0	48.6	4.36
11	86.0	59.7	2.84
12	567.0	607.7	1.71
13	294.0	367.3	4.27
14	382.0	448.6	3.41
15	241.0	306.5	4.22
16	2238.0	2326.1	1.86
17	2109.0	2233.1	
18	386.0	487.0	
19	260.0	330.7	
20	232.0	295.0	
21	614.0	722.0	
22	75.0	63.3	
23	124.0	130.7	
24	139.0	137.7	
25	121.0	102.8	
26	77.0	91.4	
27	73.0	82.9	
28	80.0	41.5	
29	23.0	21.8	
30	37.0	18.0	
31	43.0	12.1	
32	70.0	14.2	

Table 4.8

No.	Data	Fit	SD
1	4.0	4.3	0.14
2	6.0	3.7	0.95
3	9.0	2.8	2.08
4	1.0	2.6	1.62
5	8.0	7.7	0.10
6	39.0	34.0	0.80
7	63.0	34.5	3.58
8	15.0	13.5	0.37
9	26.0	24.3	0.35
10	11.0	9.5	0.45
11	16.0	9.4	1.66
12	342.0	372.3	1.64
13	134.0	145.5	0.99
14	124.0	142.7	1.68
15	93.0	100.0	0.73
16	1533.0	1543.9	0.28
17	1066.0	1113.6	
18	191.0	237.9	
19	211.0	266.7	
20	160.0	207.4	
21	229.0	292.4	
22	40.0	51.5	
23	63.0	74.5	
24	54.0	55.4	
25	80.0	79.0	
26	57.0	62.5	
27	44.0	49.0	
28	82.0	29.1	
29	27.0	14.7	
30	28.0	10.4	
31	34.0	11.7	
32	58.0	8.1	

*Table 4.9*

No.	Data	Fit	SD
1	6.0	8.5	1.02
2	11.0	8.8	0.66
3	11.0	5.5	1.66
4	19.1	7.4	2.68
5	19.1	16.2	0.66
6	52.2	42.1	1.40
7	58.3	62.6	0.56
8	47.2	34.6	1.83
9	34.2	36.9	0.46
10	33.1	20.4	2.21
11	41.2	29.1	1.89
12	322.4	345.5	1.29
13	160.7	191.1	2.40
14	245.1	271.7	1.70
15	136.6	159.6	1.97
16	1504.7	1511.6	0.18
17	1214.4	1272.6	
18	217.0	271.1	
19	194.9	60.6	
20	175.8	239.2	
21	297.3	358.8	
22	58.3	48.9	
23	94.4	93.6	
24	49.2	65.3	
25	95.4	87.2	
26	58.3	63.1	
27	59.3	58.6	
28	57.3	32.9	
29	15.1	15.1	
30	28.1	12.4	
31	33.1	11.9	
32	54.2	9.7	

*Table 4.10 (1984 Efficiencies)*

Plane	Good tracks	All tracks
u	92.6 $\mp$ 0.9 %	89.4 $\mp$ 0.9 %
y	89.8 $\mp$ 0.9 %	88.1 $\mp$ 0.8 %
v	89.5 $\mp$ 1.0 %	87.7 $\mp$ 1.0 %
z	76.3 $\mp$ 1.0 %	74.8 $\mp$ 1.0 %

*Table 4.11 (1985 Efficiencies)*

Plane	Good tracks	All tracks
u	88.4 $\mp$ 0.7 %	85.8 $\mp$ 0.6 %
y	86.7 $\mp$ 0.7 %	84.6 $\mp$ 0.6 %
v	81.6 $\mp$ 0.9 %	81.4 $\mp$ 0.6 %
z	77.2 $\mp$ 1.0 %	75.2 $\mp$ 0.9 %

*Figures - Chapter 4*

Fig. 4.1a

The number of space points in the TRIDENT tracks for the 1984 data taking run.

Fig. 4.1b

The number of space points in the TRIDENT tracks for the 1985 data taking run.

Fig. 4.2a

The separation (cm) between the projected TRIDENT tracks and the nearest shower with energy greater than 1 GeV, at the front face of the calorimeter, for the 1984 data.

Fig. 4.2b

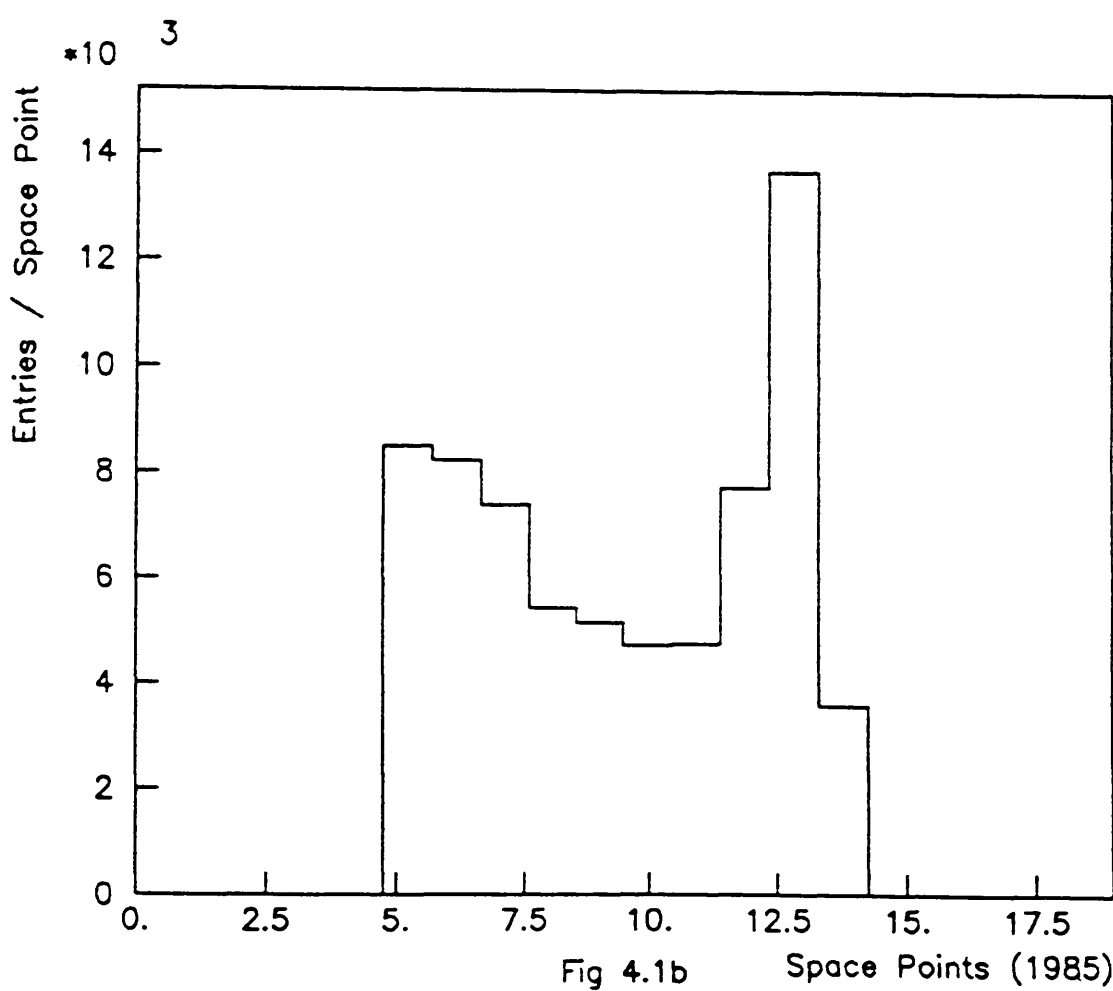
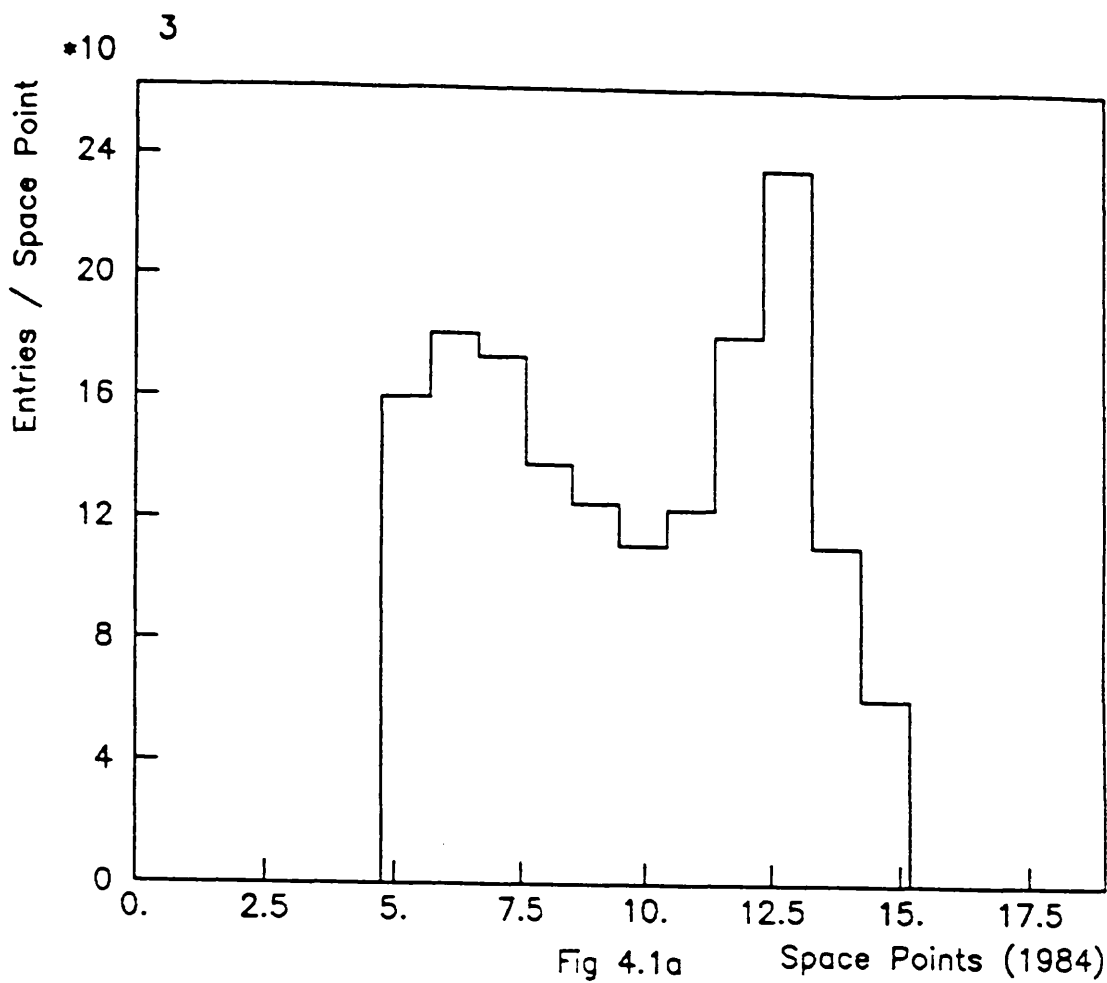
The separation (cm) between the projected TRIDENT tracks and the nearest shower with energy greater than 1 GeV, at the front face of the calorimeter, for the 1985 data.

Fig. 4.3

The area of the 4m chamber covered by the four planes of wires (white), and the area covered by three planes (shaded).

Fig. 4.4

The distance between the projected TRIDENT track and the nearest digitising for the u plane, using the 1985 data.



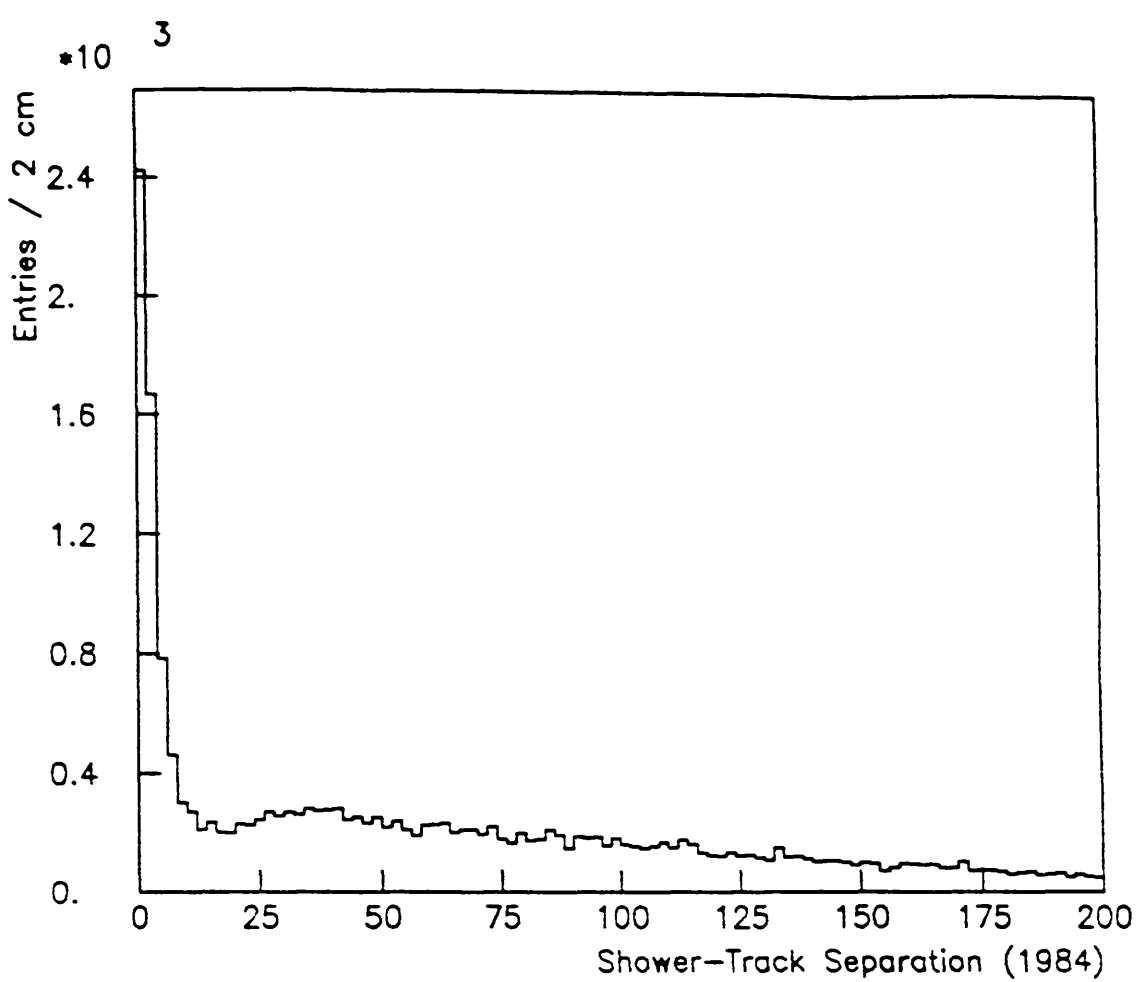


Fig. 4.2a

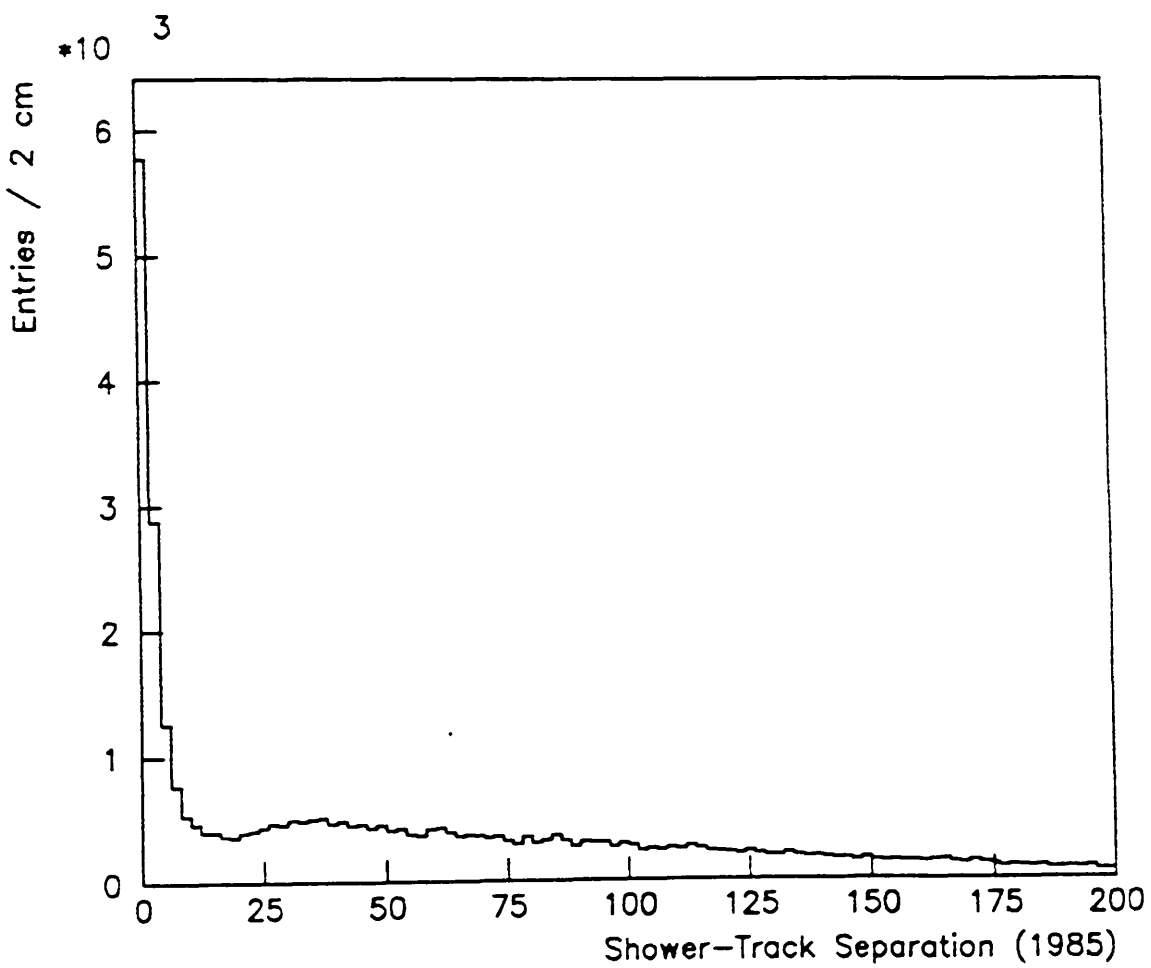


Fig. 4.2b

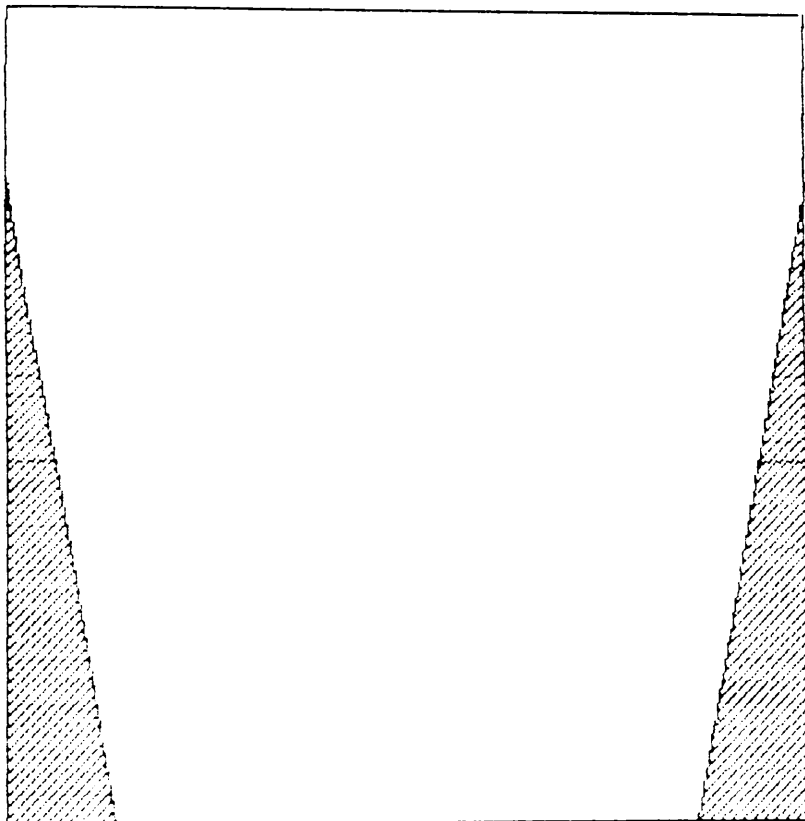


Fig. 4.3

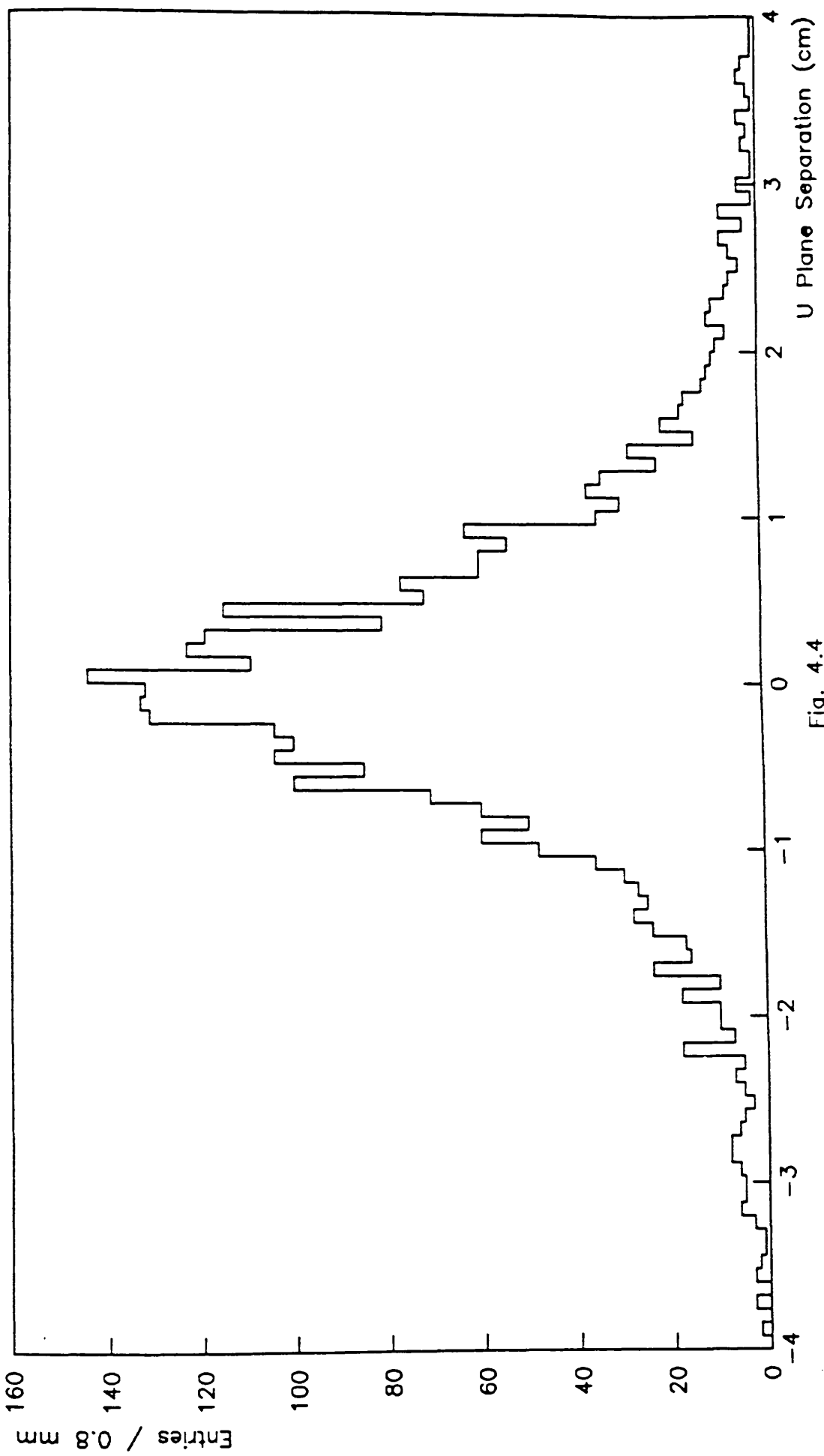


Fig. 4.4

## CHAPTER 5

### *Offline Calorimeter Calibration*

#### 5.1      *Discontinuities in Calorimeter Calibration*

##### 5.1.1      Introduction

During the analysis of the data taken by the source calibration system in the 1984 run, a discontinuity in the form of a step was observed between the wide and narrow channels in segments 1 and 2, even after correction had been made for the different geometries.

As a test of the validity of the source data, it was decided to check in the raw experimental data to see if steps also existed between the wide and narrow channels.

To provide a reasonable data sample for the test, six runs were chosen at random from the processed tapes. This produced a total of 177653 events.

##### 5.1.2      Analysis

The complete data sample was used to produce the sum of the ADC counts in each channel for both views in the three segments of all four quadrants. Although the third segment in each quadrant contains only wide channels and thus should not show any step, the segment 3 data was analysed to check the reliability of the method.

However, simply plotting the resultant summed ADC distribution for each view and fitting the curve to produce the step value for each case was insufficient, as an online cut of 5 ADC counts had already been applied to this data. This produced a 'step up' going from narrow to wide channels in all cases,

as this uniform cut had a greater effect on the narrow channels.

To overcome this ADC cut, two methods were used;

- 1) ADC cuts of 5, 7, 10, 14, 20 and 28 were applied in turn to the experimental data. A fit was then performed on PMs 81-112 of each of the resulting distributions, using the equation

$$F(x) = A.C \exp (-B x)$$

where C is the factor by which to multiply the wide tubes to obtain the best fit to the curve and so determine the step value. A plot of the step size, calculated by the fit against the ADC cut is shown for a typical example in the lower curve of Fig. 5.1. An extrapolation of this curve to a zero cut estimates a step of about  $30 \pm 3\%$ .

- 2) A more refined procedure used cuts of 5, 7, 10, 14 on the narrow channels and 10, 14, 20, 28, respectively on the wide channels. The resulting curves were again fitted with the above equation. Using the same example as before, a plot of the calculated step against ADC wide channel cut is shown in the upper curve of Fig. 5.1. This gives an apparent value for the step of about  $28 \pm 3\%$ .

This procedure was repeated for all sixteen views in segments 1 and 2 (S1, S2) and the results are shown in Table 5.1; Q1 - Q4 refer to the appropriate quadrants.

The source scan data was analysed independently to produce the sixteen corresponding step values. The two sets of measurements are compared in Fig. 5.2.

As this work was only intended as a test of the source data, a full error analysis was not performed on either set of results. However, Fig. 5.2 clearly shows a strong correlation between the steps observed in the source scan data and

those seen in the experimental data.

When the fits were performed on the segment 3 data, the average value obtained was consistent with 1.

Along with other analyses of the source data, this work resulted in the source system being used to set the PM voltages for the 1985 data taking run. An electron beam scan of quadrants 2 and 4 of the calorimeter performed in 1985, showed no steps between the wide and narrow channels, after correction for the different geometries.

## 5.2       *Absolute Energy Calibration*

### 5.2.1      Introduction

When the experiment was first being set up, it was hoped that the decay  $J/\psi \rightarrow e^+e^-$ , would provide a useful means of absolute energy calibration. This was expected to be particularly helpful since the  $J/\psi$  decay products are charged and so the mass can be reconstructed independently, using either the calorimeter or TRIDENT information. Consequently, as mentioned in Chapter 2, a special calorimeter trigger was included to detect the  $e^+e^-$  pair. This trigger demanded showers with  $P_t$  greater than 1.8 GeV/c in quadrant 1 and quadrant 3 respectively.

This section describes the work carried out to detect a  $J/\psi$  signal using the calorimeter and TRIDENT information.

### 5.2.2      Monte Carlo

A Monte Carlo was written to study both the experimental detection

efficiency for the  $J/\psi$  and the ability of a mass reconstruction algorithm to reproduce the accepted value for the mass using only the information given by the calorimeter showers.

a) Event Generation and Acceptance

The  $J/\psi$  particles were generated in the centre of mass frame using experimental data for the  $X_f$  and  $P_t$  distributions [28]. The vertex distribution was uniform along the length of the target. The  $J/\psi$  were then allowed to decay into  $e^+e^-$  pairs, boosted into the laboratory frame and tracked through the Omega field, using a field map. This gave the  $e^+e^-$  momenta and position at the downstream edge of the field. The particles were then projected to the calorimeter and the detection efficiency calculated. This efficiency took account of both the geometrical acceptance and the effect of the 1.8 GeV/c  $P_t$  trigger.

A plot of the asymmetry of the detected pairs is shown in Fig. 5.3, with the asymmetry of a particle pair with energies  $E_1$  and  $E_2$ , respectively, defined as,  $(E_1 - E_2)/(E_1 + E_2)$ . Hence an asymmetry cut of 0.6 was applied in the analysis of the real data.

b) Mass Reconstruction

In testing the mass reconstruction algorithm, it was initially assumed that if the electron and positron both hit the calorimeter, then their energy was measured exactly.

Two basic assumptions were also made about the Omega field;

- 1) it is perfectly uniform,
- 2) it has a precise cut-off point in  $x$ .

The Omega field strength was 1.18 T and the effective length of the field

in the x direction was 2.04 m from the downstream end of the target to the end of the field.

To calculate the invariant mass of the electron pair, their momenta at the vertex point must be determined. To do this, it was assumed that the path of each charged particle from the end of the magnetic field to the calorimeter front face was a straight line, and inside the field the path was the arc of a circle in the X, Y plane, with the radius of curvature, R in metres, being given by the equation

$$R = E / (B \times 0.29979)$$

where, E is the energy of the calorimeter shower in GeV,

B is the field strength in Tesla.

To provide a first estimate of the position of the particles at the end of the field, a straight trajectory from the main vertex to the calorimeter was assumed, and so the y and z coordinates of the track at  $x = 2.04$  m could be easily calculated. Then, knowing the positions of the two endpoints of the track in the field, and also the radius of curvature of the circle from the above equation, the direction of the track at the end of the field could be used to calculate the projected hit position at the front face of the calorimeter.

Although this projected hit position was inaccurate, since the real shower coordinates in the calorimeter were known, an iterative procedure could then be followed to more precisely determine the y and z coordinates of the track at the end of the field. The iteration continued until the projected hit position agreed with the known shower coordinates to within 1 mm. Therefore, knowing the coordinates of the particles both at the vertex and at the end of the field, and also the radii of curvature in the field, the momenta of the  $e^+e^-$  pair at the vertex could be determined, enabling the  $J/\psi$  mass to be reconstructed. For the events passing the trigger cut, the reconstructed mass is shown in Fig. 5.4.

An attempt is now made to introduce the spread in the mass produced by the energy resolution of the calorimeter. For a given shower energy,  $E$ , the resolution is, [21]

$$(\sigma_E/E)^2 = c_1^2/E + c_2^2$$

where,  $c_1 = 0.22$ ,

$$c_2 = 0.026 \quad \text{and} \quad \sigma_E/E \quad \text{in GeV}$$

So, for each generated charged particle, the experimental resolution can be calculated, and using a Gaussian random generator, the energy resolution effect can be imposed on the reconstructed mass plot. The resultant plot is shown in Fig. 5.5. This clearly shows that the dominant influence in the spread of the reconstructed mass is the energy resolution, and not the reconstruction algorithm.

### 5.2.3 Experimental Data

All plots have been produced using the 1985 negative data, and the results are presented for both negative and positive data samples.

The candidate  $J/\psi$  events were selected by applying the following cuts to the experimental data;

- (i) two electromagnetic showers both with  $P_t > 1.5$  GeV/c in opposite quadrants of the calorimeter,
- (ii) both showers had a corresponding TRIDENT track ending in the 4m chamber, whose projected hit position at the front face of the calorimeter was within 2 cm of the shower position,
- (iii) the asymmetry of the pair was less than 0.6

Also, for the TRIDENT mass plot, the tracks must have opposite sign.

The resultant mass plots using calorimeter shower energy and TRIDENT track momenta respectively are shown in Figs. 5.6a and 5.6b.

Using the events in the bin with lower edge 2.8 GeV/c in Fig. 5.6a (calorimeter mass plot), Fig. 5.7a shows the corresponding TRIDENT mass. Similarly, Fig 5.7b shows the calorimeter mass for the events in the bin with lower edge 3.0 GeV/c in Fig. 5.6b, the TRIDENT mass plot. These plots clearly show that some of the apparent  $J/\psi$  signal is in fact merely background.

The ratio of shower energy/track momenta for both tracks of the events shown in Fig. 5.7b is plotted in Fig. 5.8. This distribution suggests that the selected events contain a large number of hadrons, which will deposit only a fraction of their energy in the calorimeter.

A selection was therefore made on this ratio, demanding that it lay between 0.8 and 1.25 for both showers/tracks. The resultant calorimeter and mass plots are shown in Figs. 5.9a and 5.9b respectively.

Clearly, the  $J/\psi$  signal is very small, so before attempting to fit these curves, an attempt was made to reproduce the background shape for both curves, by combining showers or tracks from different candidate  $J/\psi$  events. The resultant background plots are shown in Figs. 5.10a and 5.10b.

This background shape is then combined with a Gaussian distribution to try and fit the mass plots. The resultant values for the  $J/\psi$  mass produced by the individual fits are shown in Table 5.2 for negative data and Table 5.3 for positive. The fitted values for the individual bins in the mass plots are shown as solid circles in Figs. 5.9a and 5.9b.

The results for the negative data give a TRIDENT/calorimeter mass ratio of  $1.02 \pm 0.01$  and for positive data this ratio is  $1.02 \pm 0.04$ .

Alone, these results are not statistically significant, but, they were used to confirm the results obtained in other absolute energy calibration studies.

The final adjustment of the energy scale was made using fits to the eta [21] mass distribution and comparison of the momentum of electron tracks in the Omega with the corresponding shower in the calorimeter. This showed that the energy of the showers reconstructed in the calorimeter had to be multiplied by 1.028, with an estimated systematic error of 1 %. This result is in very good agreement with the results obtained using the  $J/\psi$  mass distributions.

VIEW			Step Size (+ve = step down)
Q1	S1	Y	9 %
Q1	S1	Z	8 %
Q1	S2	Y	0 %
Q1	S2	Z	-13 %
Q2	S1	Y	6 %
Q2	S1	Z	9 %
Q2	S2	Y	3 %
Q2	S2	Z	29 %
Q3	S1	Y	6 %
Q3	S1	Z	18 %
Q3	S2	Y	26 %
Q3	S2	Z	33 %
Q4	S1	Y	-5 %
Q4	S1	Z	-6 %
Q4	S2	Y	-7 %
Q4	S2	Z	0 %

Table 5.2 - Negative data (GeV/c<sup>2</sup>)

Calorimeter mass	3.007 $\mp$ 0.010
Sigma	0.06 $\mp$ 0.04
TRIDENT mass	3.053 $\mp$ 0.028
Sigma	0.09 $\mp$ 0.02

Table 5.3 - Positive data (GeV/c<sup>2</sup>)

Calorimeter mass	2.982 $\mp$ 0.100
Sigma	0.29 $\mp$ 0.08
TRIDENT mass	3.056 $\mp$ 0.037
Sigma	0.13 $\mp$ 0.03

*Figures - Chapter 5*

- Fig. 5.1 Calculated step size against the artificial cut imposed on the wide tubes.
- Fig. 5.2 Calculated step size using experimental data against step size calculated from source scan data.
- Fig. 5.3 Asymmetry against total energy for electron pairs in the Monte Carlo data.
- Fig. 5.4 Reconstructed mass for Monte Carlo data, using correct value for particle energy.
- Fig. 5.5 Reconstructed mass for Monte Carlo data with energy smearing produced by the calorimeter.
- Fig. 5.6a Reconstructed mass for experimental data, using the calorimeter energy.
- Fig. 5.6b Reconstructed mass for experimental data, using the TRIDENT value for particles' momenta.
- Fig. 5.7a TRIDENT mass for charged particle pairs whose mass lies in the shaded bin in Fig. 5.6a.
- Fig. 5.7b Calorimeter mass for charged particle pairs whose mass lies in the shaded bin in Fig. 5.6b.
- Fig. 5.8 Ratio of shower energy/track momenta for both

particles of the events shown in Fig. 5.7b.

Fig. 5.9a                   Calorimeter mass for particles whose shower energy/track momenta ratio lies between 0.8 and 1.25. Solid circles show the mass produced by the fit.

Fig. 5.9b                   TRIDENT mass for particles whose shower energy/track momenta ratio lies between 0.8 and 1.25. Solid circles as before.

Fig. 5.10a                  Background shape for calorimeter mass distribution.

Fig. 5.10b                  Background shape for TRIDENT mass distribution.

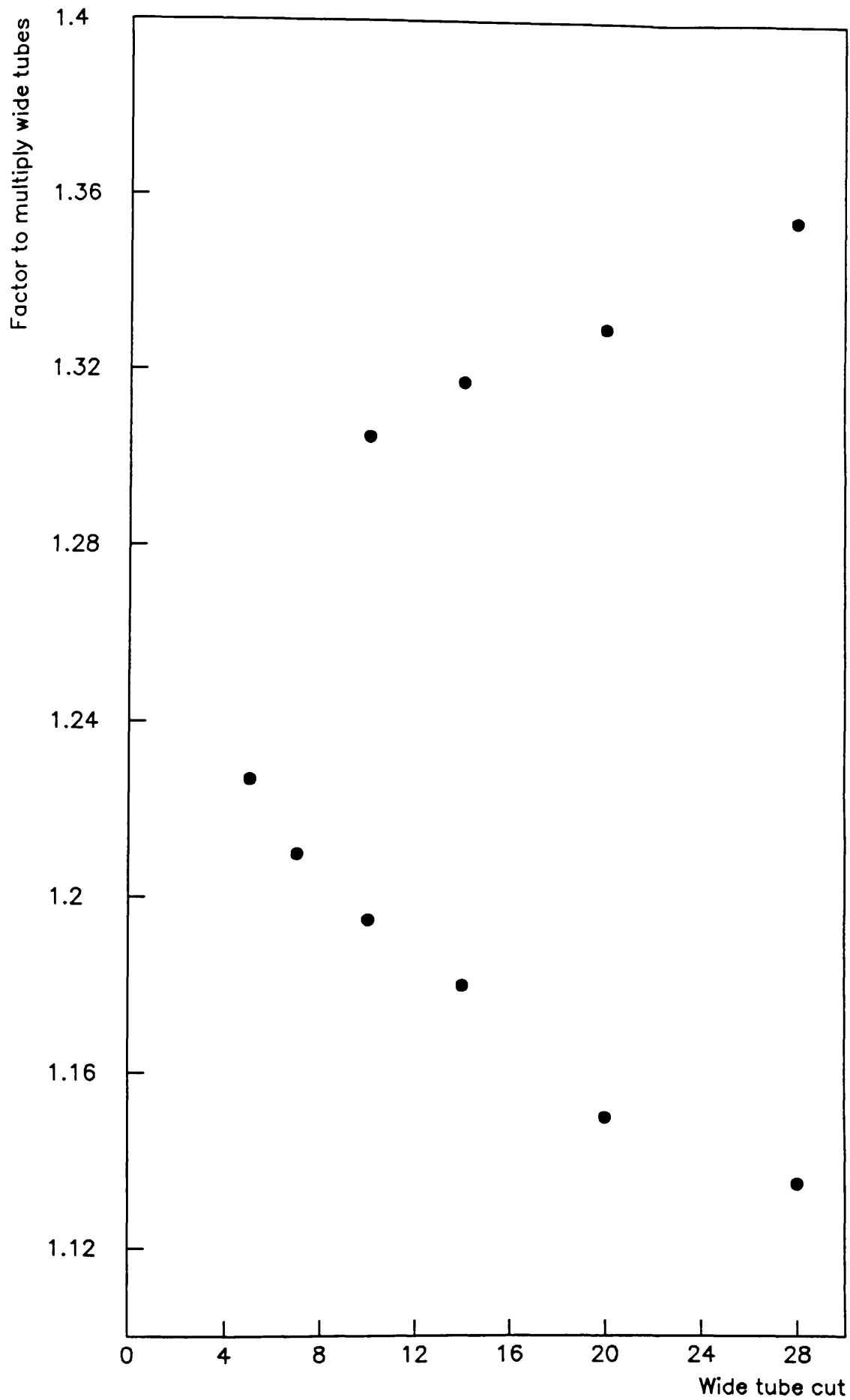


Fig. 5.1

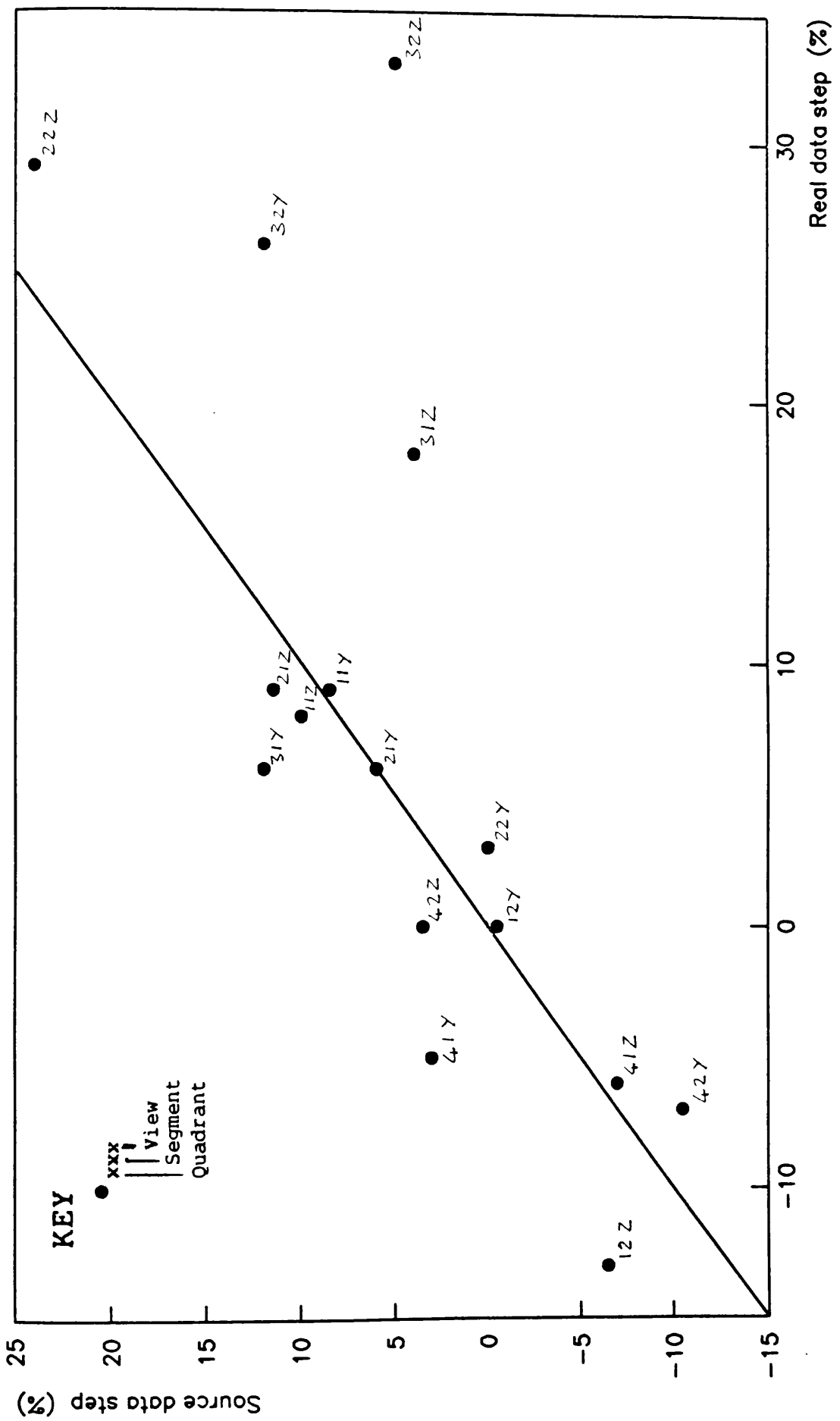


Fig. 5.2

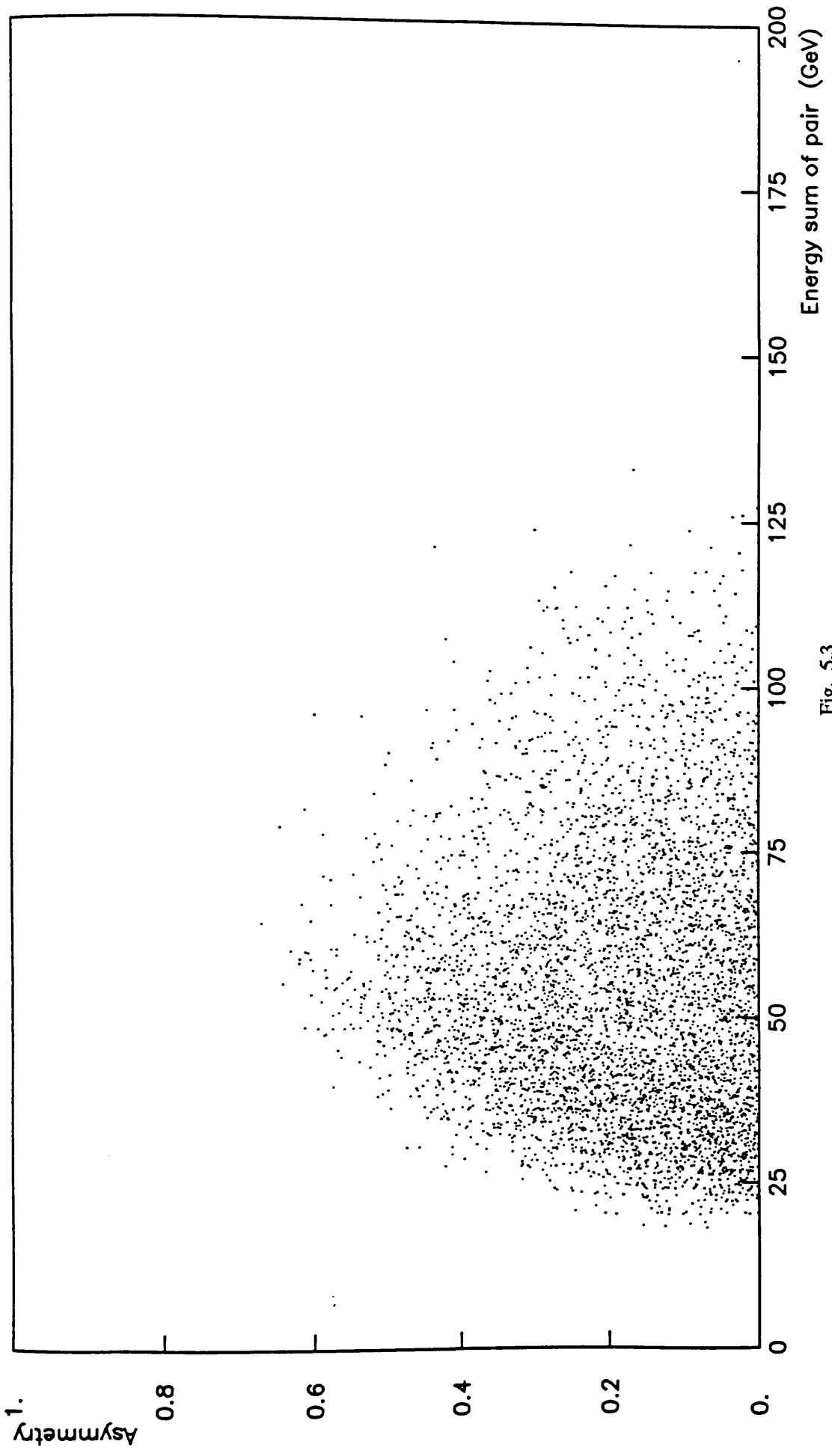


Fig. 5.3

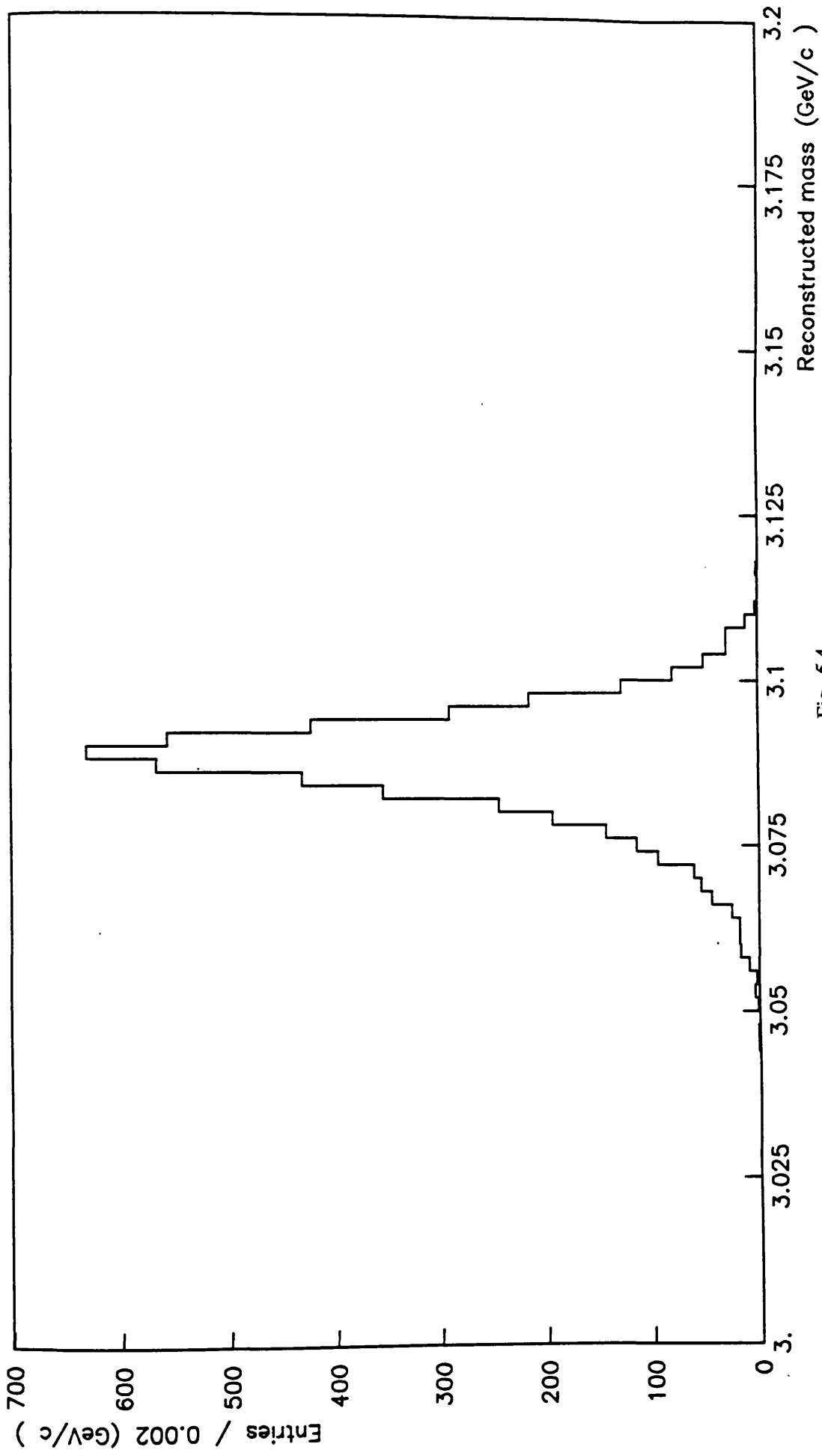


Fig. 5.4

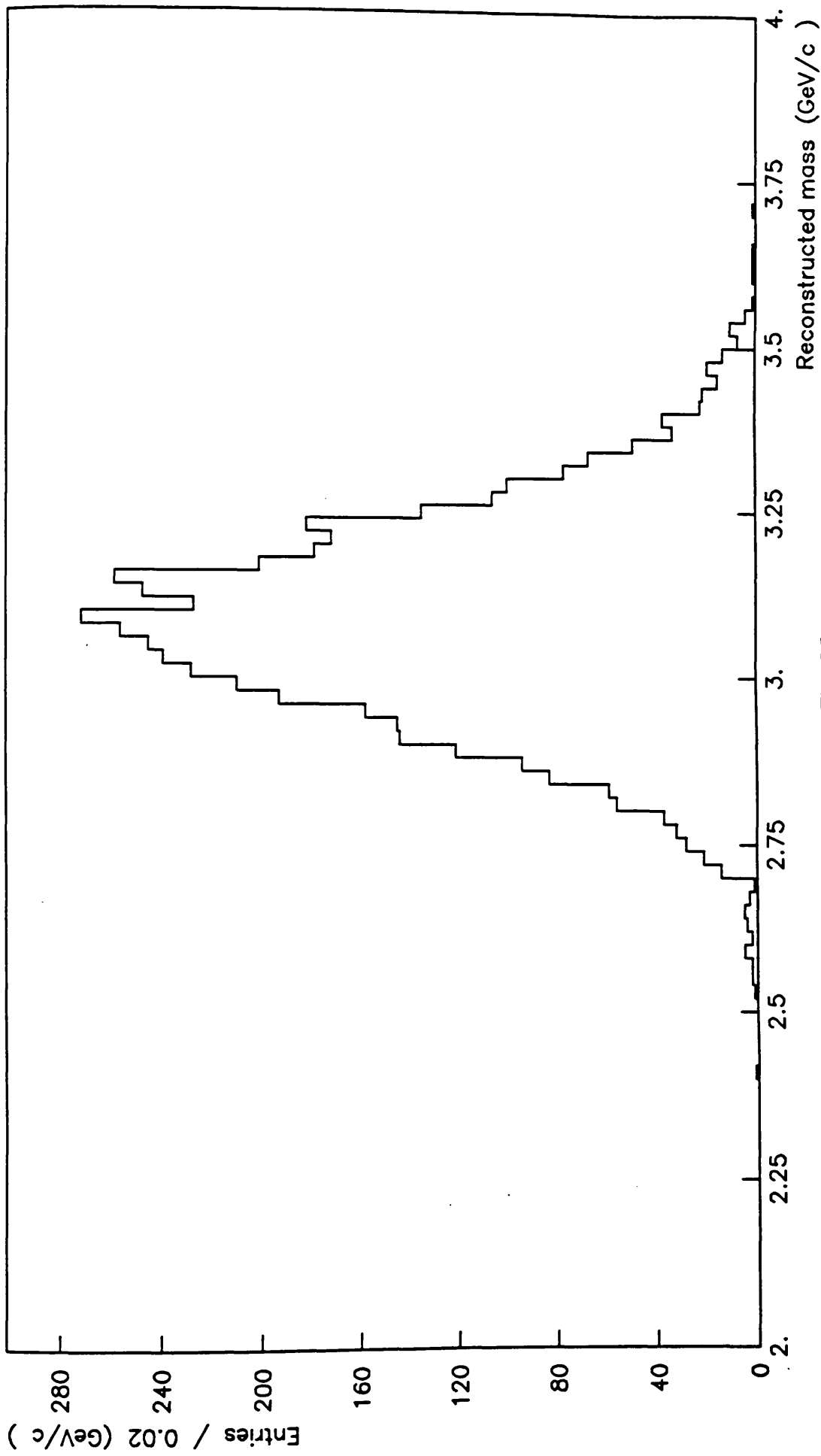


Fig. 5.5

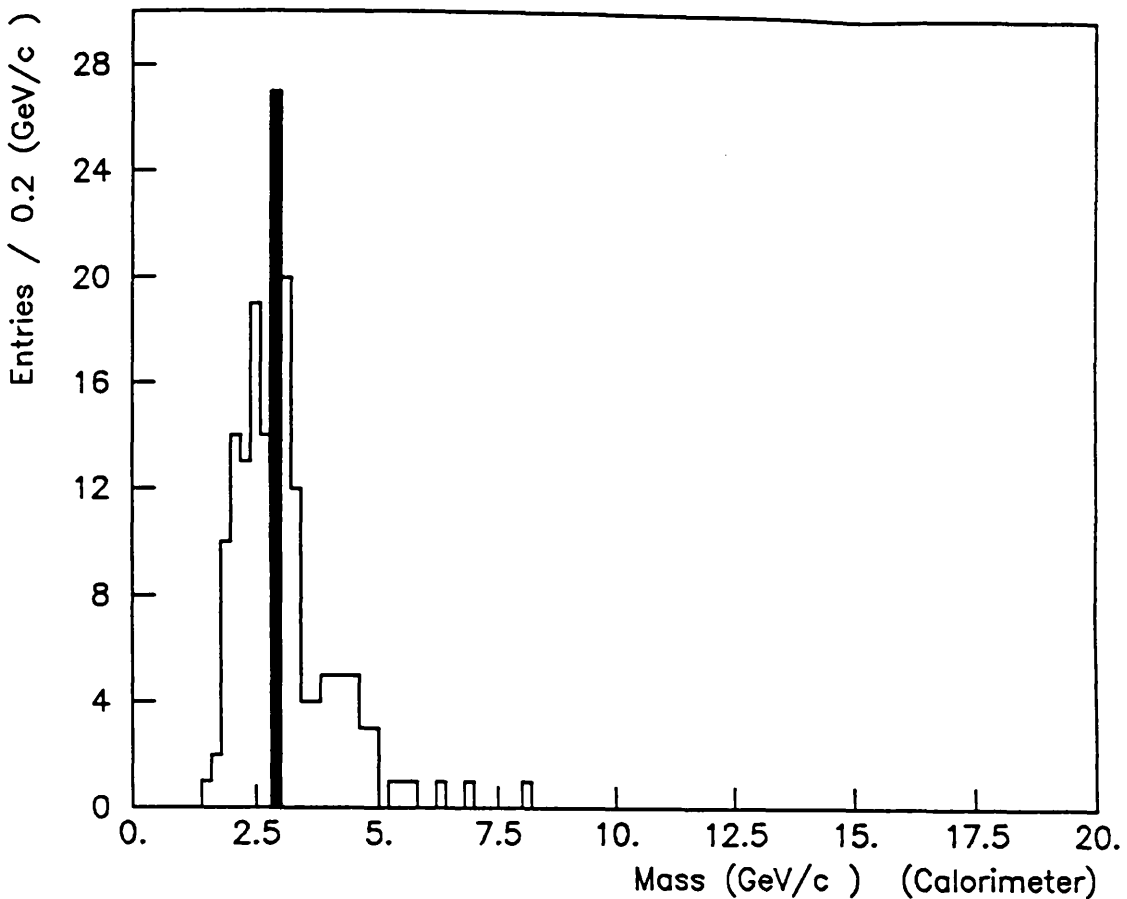


Fig. 5.6a

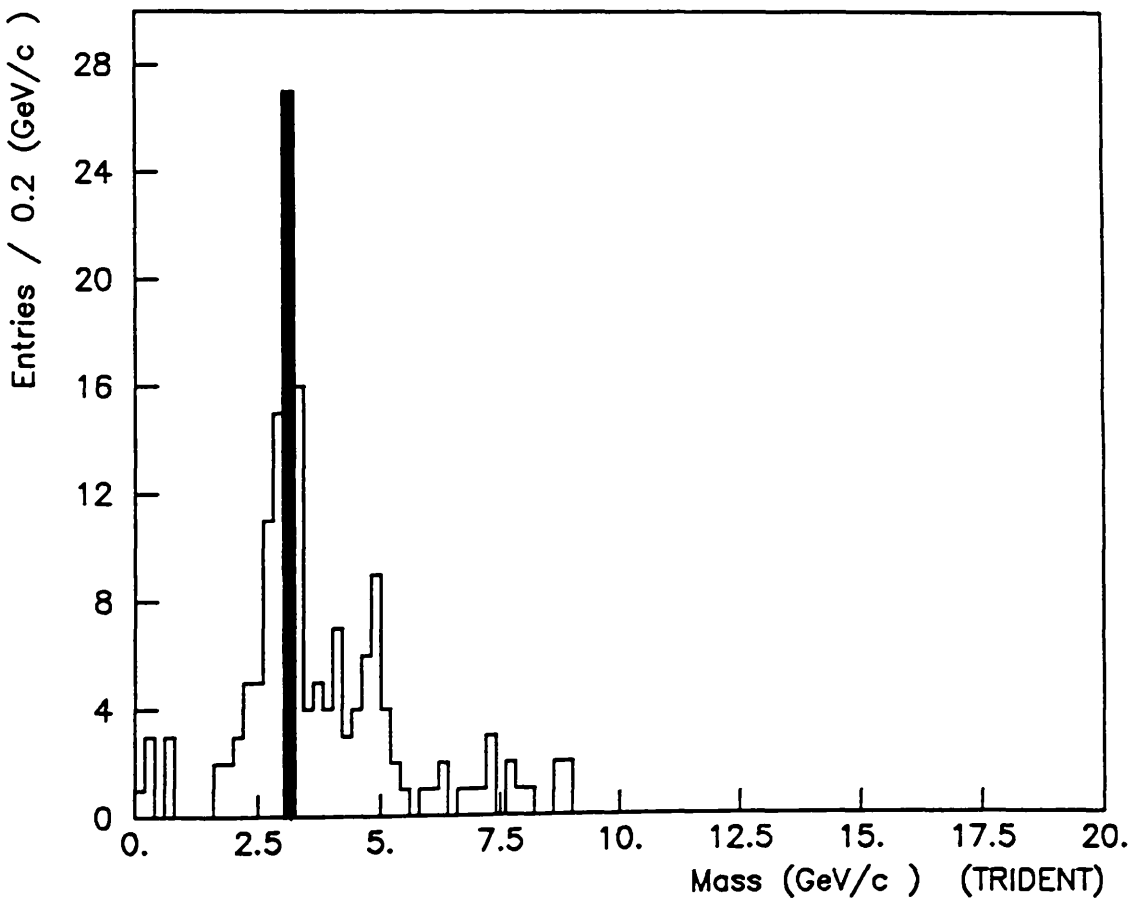


Fig. 5.6b

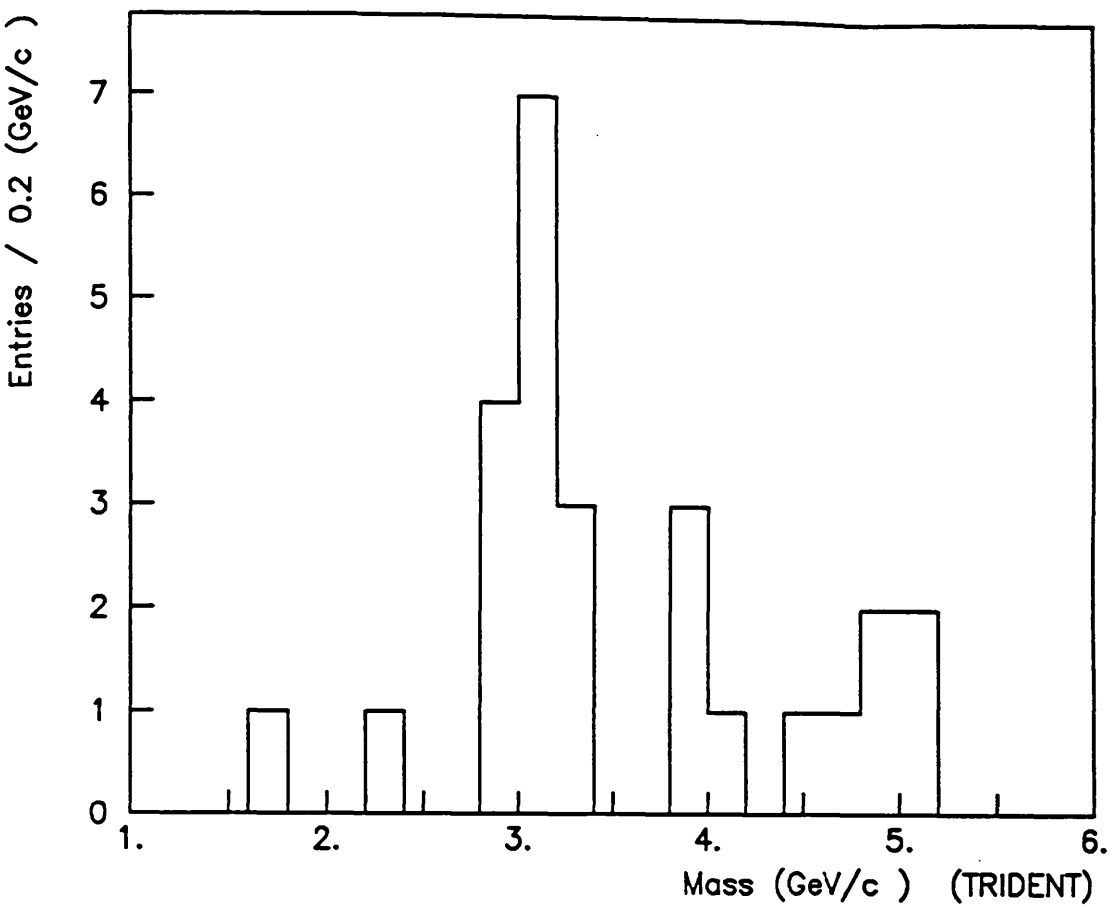


Fig. 5.7a

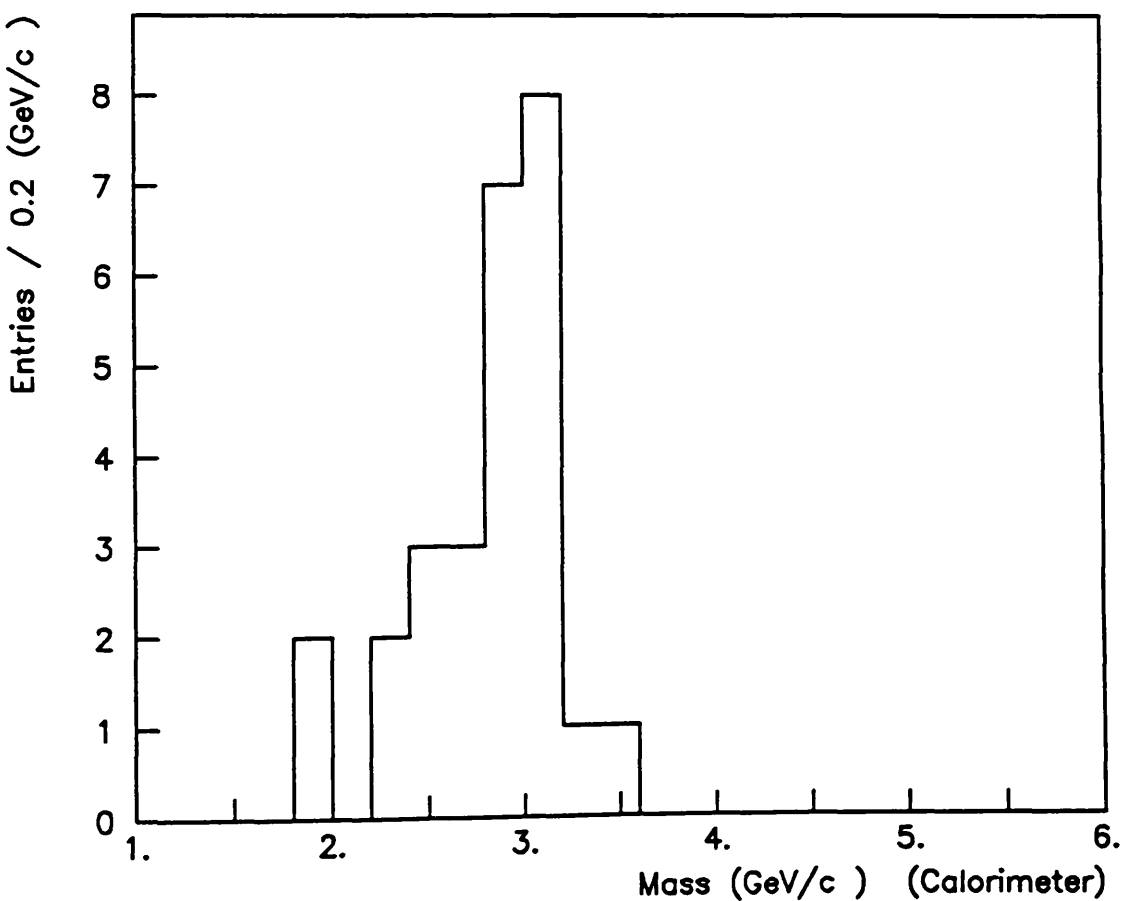


Fig. 5.7b

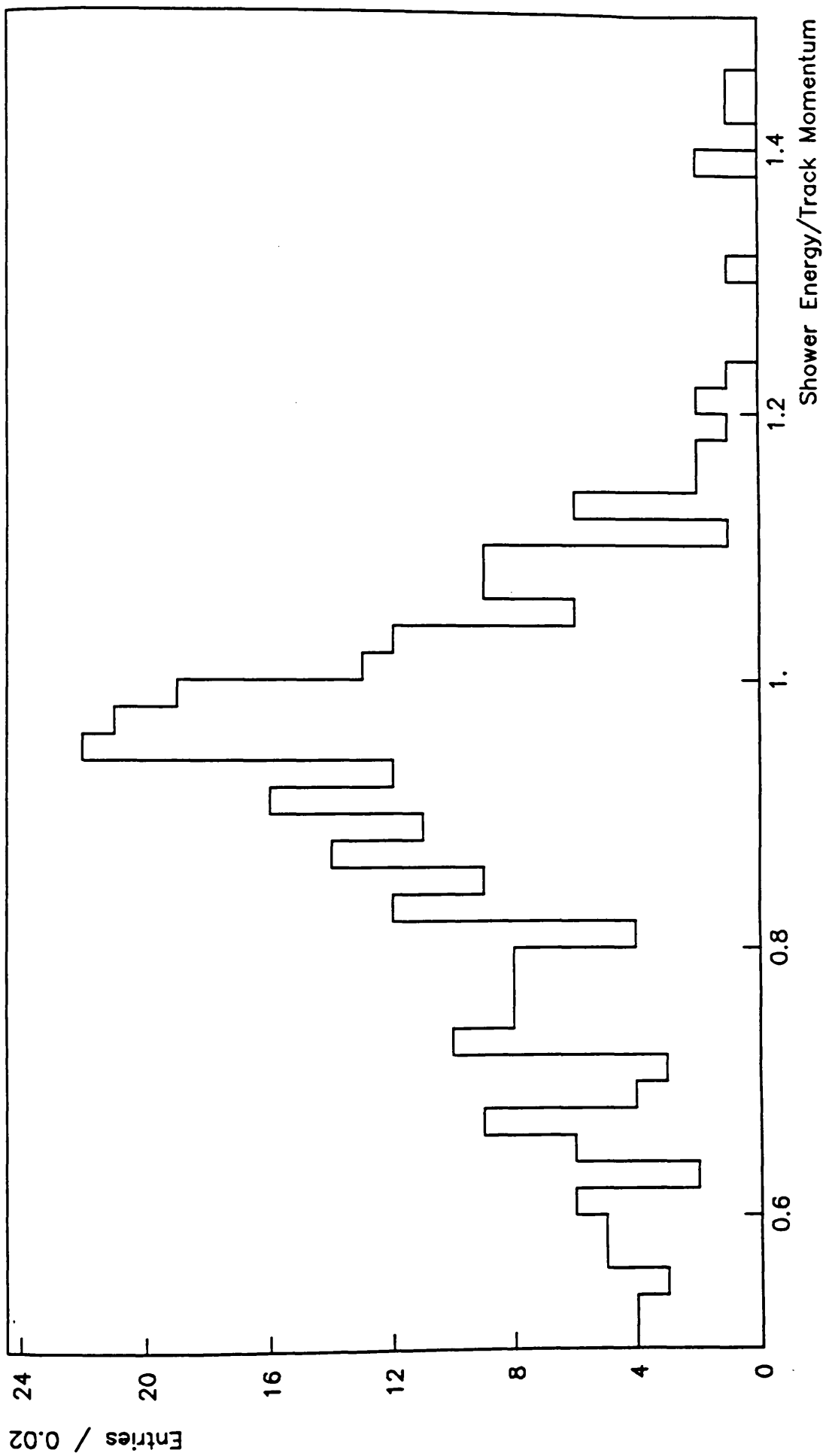


Fig. 5.8

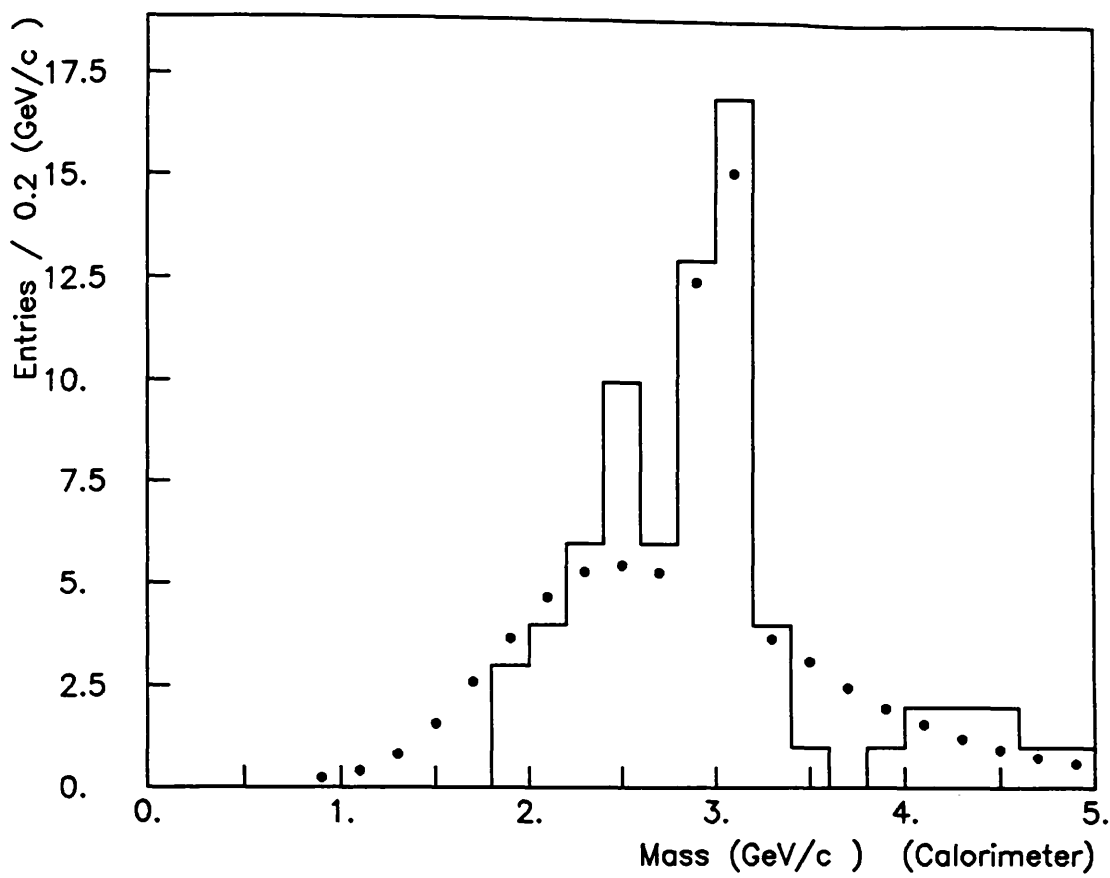


Fig. 5.9a

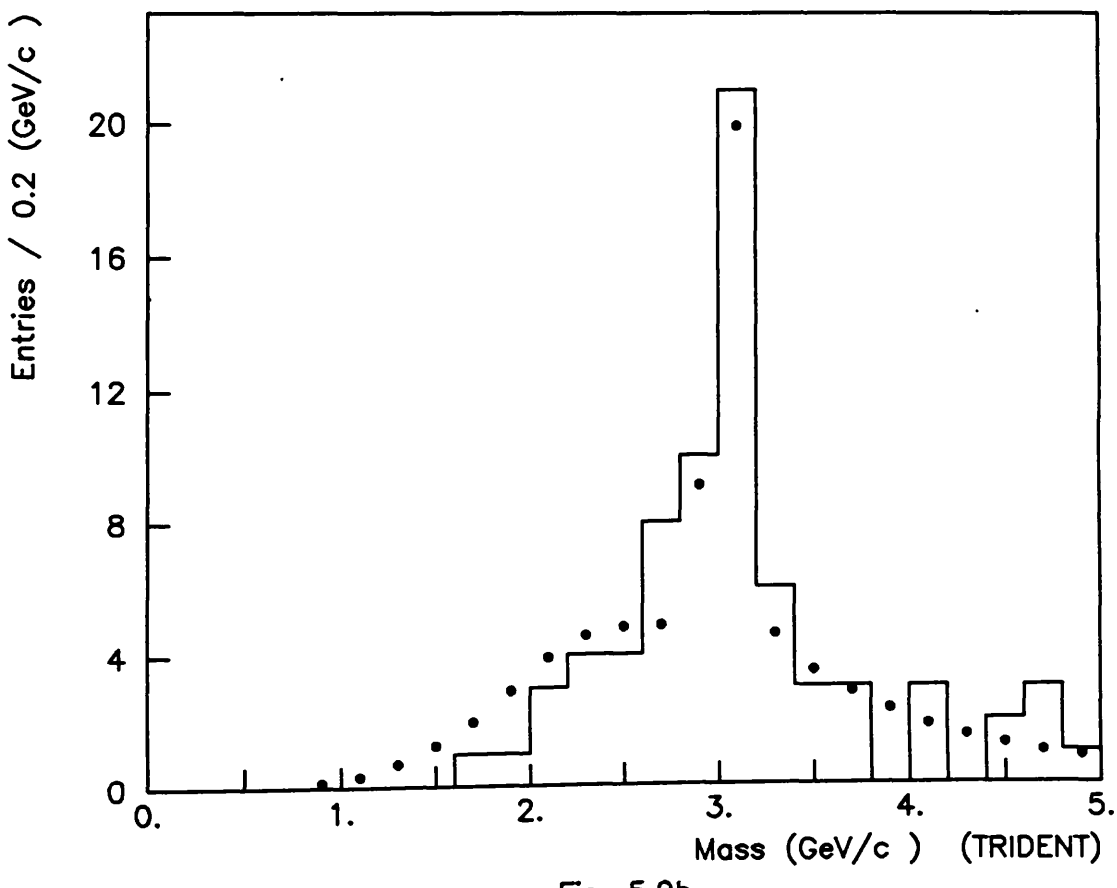


Fig. 5.9b

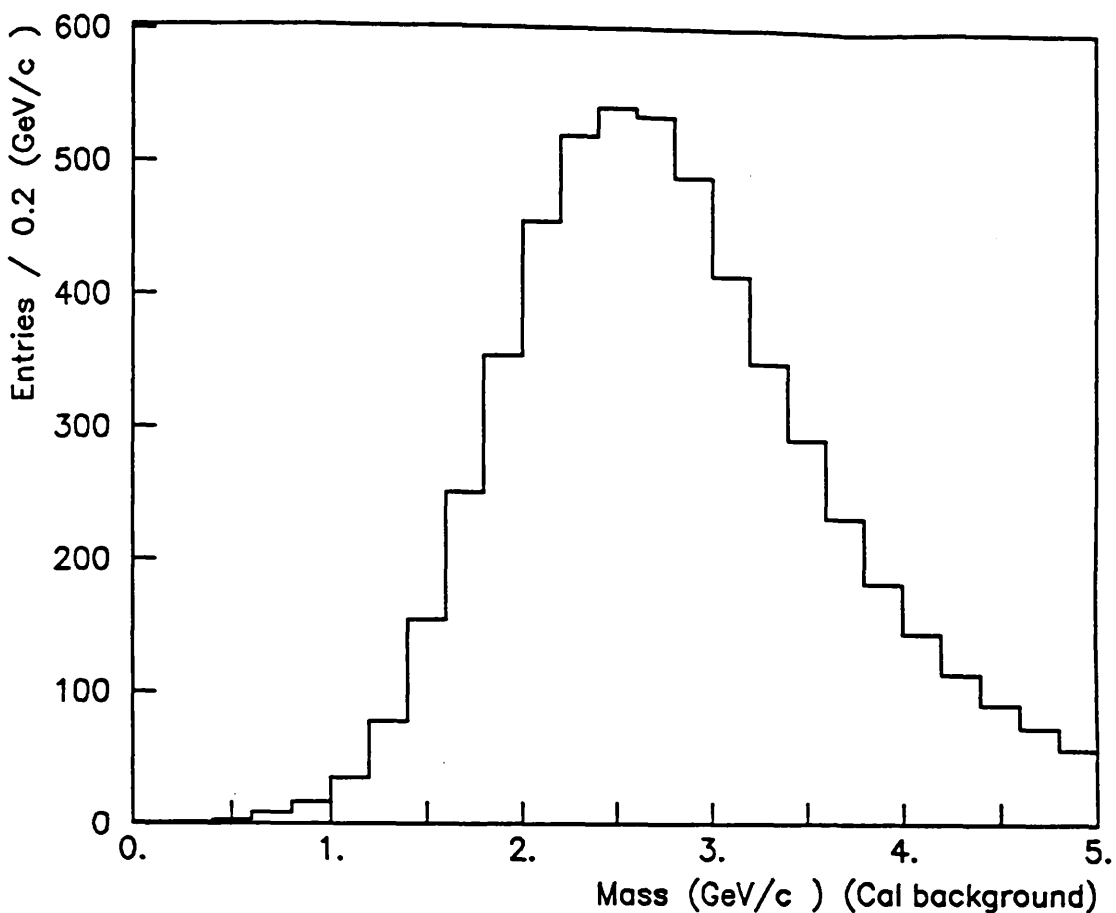


Fig. 5.10a

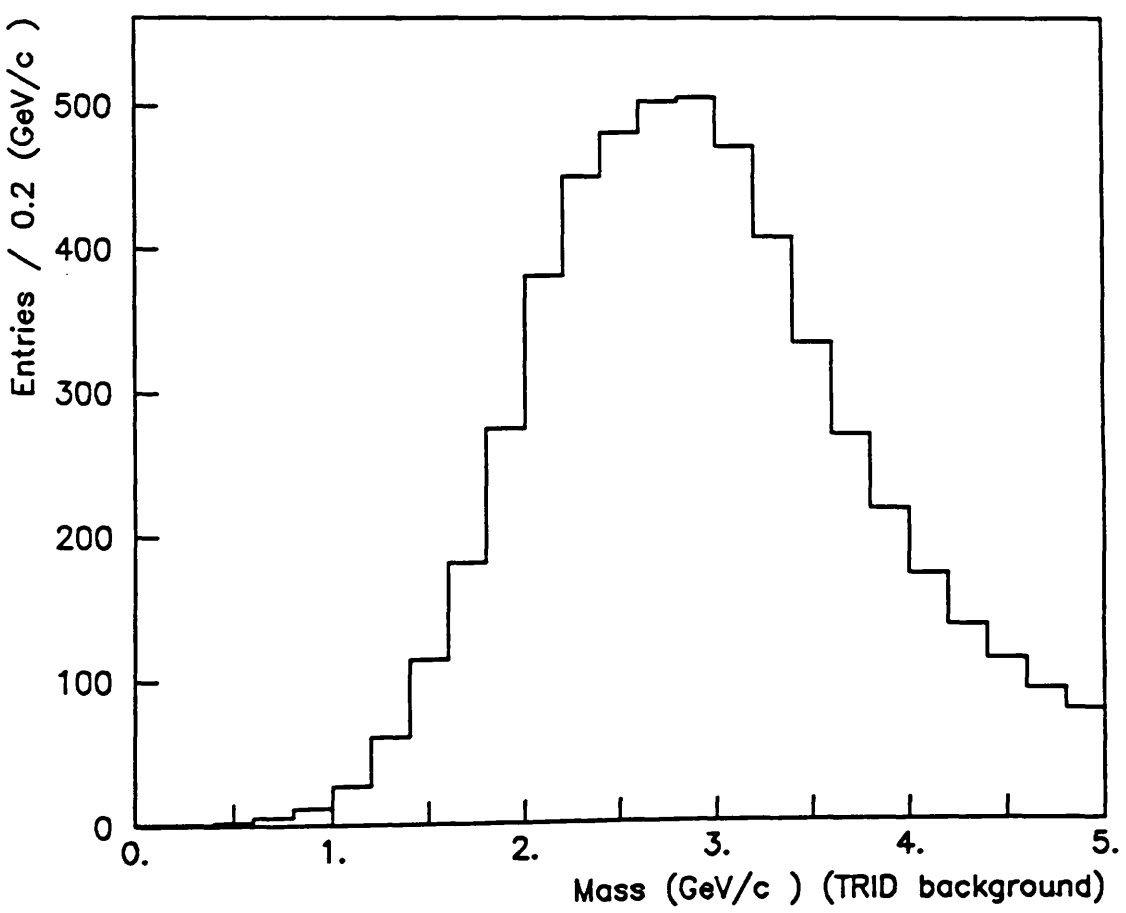


Fig. 5.10b

## CHAPTER 6

### Direct Photon and $\pi^0$ Analysis

#### 6.1 *Introduction*

The process used to obtain direct photon and  $\pi^0$  cross-sections, from data taken in the 1985 run, can be divided into three distinct parts ;

- (1) Analysis of experimental data to produce raw samples of direct photons and  $\pi^0$ 's,
- (2) Estimation of background in the raw signals and loss of good events due to the different analysis cuts,
- (3) Monte Carlo calculation of acceptance.

#### 6.2 *Experimental Data Analysis*

##### 6.2.1 Selection of Direct Photon and $\pi^0$ Events

Before carrying out the physics analysis, the data obtained with the positive beam was divided to provide clean samples of  $\pi^+$  and proton beam particles. There were four pieces of information available to determine the identity of the incident particle; the PI bit, the P bit and C1 and C2, the cedar bits.

The CEDARS had both been tuned to detect pions, so the C1 and C2 bits were used to define pions. It had been observed that in some events, both the PI and P bits had been set, and these events were rejected. Thus, the resulting positive beam particle definitions were,

$$\pi^+ = (\text{PI NOT P}) \text{ AND } (\text{C1 OR C2})$$

$$p = (P \text{ NOT PI})$$

These cuts produced  $2.201 \times 10^{11}$  incident  $\pi^+$  and  $6.996 \times 10^{11}$  protons. There were  $3.525 \times 10^{11}$  incident  $\pi^-$  in the negative data.

The initial aim of the physics analysis was to produce a good sample of high Pt electromagnetic showers. To do this, events are rejected in which;

- (1) there is no reconstructed main vertex, or the vertex is not in the target,
- (2) there is a hit in the halo counters,
- (3) the trigger shower is out of time,
- (4) the highest Pt shower fails one of the following 'gentle' muon halo cuts.

There are three different cuts which can be applied to showers to reject the halo contamination;

(i) TOF

The distance between the TOF prediction and the actual position of a shower, from the PM signal, is greater than 40 cm for the 'gentle cut' and greater than 24 cm for the more strict cut. This removes the trigger showers that are not associated with the event in the target.

(ii) Shower direction

The direction of muons from the beam halo is basically parallel to the beam, and since direct photons originate from the target, the position of the showers in the three segments can be used to define a direction and reject particles travelling parallel to the beam.

(iii) 4m chamber

Events are rejected in which the trigger shower lies within 2 cm of the nearest two plane hit in the U, Y and V planes of the 4m chamber, indicating that the shower was caused by an electron or charged hadron.

A shower passing all of the above cuts is a candidate direct photon. The shower is now combined with all other electromagnetic showers to determine if

the shower has resulted from a  $\pi^0$  or  $\eta$  decay. A  $\pi^0$  is defined as any combination of the direct photon candidate with another electromagnetic shower, with energy greater than 500 MeV, which has a mass in the range 70-200 MeV/c<sup>2</sup>. An  $\eta$  is defined as any combination of the direct photon candidate with another electromagnetic shower, with energy greater than 2 GeV, which has a mass in the range 450-650 MeV/c<sup>2</sup>.

A search is also made in the secondary hypotheses produced by the GLOBAL pattern recognition program (3.2.3) for a  $\pi^0$  in the same quadrant as the candidate direct photon.

If the shower is found to come from a  $\pi^0$  or  $\eta$  decay, then it is rejected as a candidate direct photon.

At this stage it is necessary to determine how to divide the data in bins of Xf and Pt. It was decided that for the analysis of the 1985 data, the lower edge Pt cut-off should be at 4.0 GeV/c and that the results be presented in Pt bins of 0.5 GeV/c with the top bin size being 1.0 GeV/c. The top bin is 6.0 - 7.0 GeV/c for the  $\pi^- p$  and pp data samples, and 5.5 - 6.5 GeV/c for  $\pi^+ p$ , due to the reduced numbers of high Pt direct photon events produced by  $\pi^+ p$  interactions.

The Xf bins were chosen to be symmetric about 0. For the  $\pi^- p$  and  $\pi^+ p$  interactions the backward and forward bins were 0 - 0.15 and 0.15 - 0.45. Due to the rapidly decreasing acceptance of the calorimeter in backward Xf for pp interactions, the Xf bins chosen were 0 - 0.15 and 0.15 - 0.35.

### 6.2.2 $\pi^0$ Analysis

To produce the electromagnetic pair mass plot, the trigger shower, from events identified as containing a potential  $\pi^0$  or  $\eta$ , was combined with all other electromagnetic showers with energy greater than 500 MeV. The asymmetry plot

for these combinations is shown in Fig. 6.1. This distribution clearly peaks at high asymmetry, so an asymmetry cut of 90 % was imposed on the shower pairs. The resultant masses were plotted separately in their respective Xf and Pt bins. The mass plot in the  $\pi^- p$  data for the Xf region 0 - 0.15, and Pt 4.0 - 4.5 GeV/c is shown in Fig. 6.2. The  $\pi^0$  peak is clearly visible.

The corrected number of  $\pi^0$ 's is extracted from the plot by performing a sideband subtraction using the five bins on either side of the peak. This process was repeated for all Xf and Pt bins in the three interactions.

### 6.2.3 Direct Photon Analysis

Additional cuts on the candidate shower, to produce the raw direct photon sample, are;

1. Pt of the shower is greater than 3.5 GeV/c,
2. a fiducial cut, in which the distance of the shower from the edge of the quadrant is greater than the separation between the two photons of a  $\pi^0$  decaying with 50 % asymmetry + 2 cm,
3. the average shower width in segment 1 is less than 3 cm,
4. the shower passes the strict halo cuts,
5. the shower cannot be linked to a TRIDENT track or a hit in the 4m chamber. TRIDENT tracks are projected to the calorimeter, and the shower is rejected, if the distance to the nearest projected hit is less than 3 cm and the ratio track momentum/shower energy is greater than 0.5. In using the 4m chamber, the candidate shower is projected onto the 4m chamber and the event is rejected if a 3 or 4 plane hit occurs within 3 cm.

### 6.3      *Backgrounds and Losses*

Inevitably, the cuts applied to the data to remove background events result in the loss of some good direct photons and  $\pi^0$ 's. This section describes the procedures carried out to calculate the necessary corrections for the individual cuts. The value for each of the corrections is shown at the appropriate point in Section 6.6 or 6.7.

#### 6.3.1      Losses common to both $\pi^0$ and direct photon events

##### 1. Gentle Halo Cuts.

The analysis program was run on the events rejected with hits in the halo counters and rejected by the halo cuts. Assuming that the same percentage of  $\pi^0$  and direct photon events are lost by these cuts, the number of background subtracted  $\pi^0$ 's in this sample is taken as a percentage of the real  $\pi^0$  signal to obtain the correction factor. As the halo was concentrated in a particular spot in the calorimeter, the effect of the halo cuts was not expected to be flat in Xf and Pt. No observable variation with Pt was detected, but the loss was found to be greater in the backward Xf bin.

##### 2. Processing Filters.

Before the events are processed by GLOBAL, MICE and TOF filters have been applied. The effect of these cuts could not be properly simulated in the Monte Carlo due to the presence of overlapped events in the real data which were not considered in the Monte Carlo.

The method used to determine the losses in the production chain is, as before, using the  $\pi^0$  mass plot to estimate the percentage of  $\pi^0$ 's lost, and the percentage loss is assumed to be the same as for direct photons.

### 3. A<sub>1</sub>, A<sub>2</sub>, Vetoes.

There are two separate problems to be considered in calculating the losses produced by the two veto counters. Firstly, random noise in the counters produces a spurious signal. This effect was measured directly by putting the counters out of time and checking what fraction of events were still being vetoed. This correction was found to be 1.05 ± 0.02.

Secondly, the effect of particles, produced by an interaction in the target, hitting the counters must be considered. This was studied by Monte Carlo, and the resultant correction was 1.02 ± 0.002.

### 4. Non-target interaction events.

A correction was calculated for events whose interactions did not occur in the hydrogen target, but which still pass the vertex cuts. This effect was studied by taking some data with the target empty. In practice, very few of these events were found to pass the vertex cuts.

### 5. Attenuation in target.

Due to interactions in the target, the number of particles in the beam decreases along the target. This loss has been estimated using the Clean Beam and Interaction scalers, and assuming a simple exponential decrease along the target the attenuation constant can be calculated, giving the mean value of the beam intensity relative to its initial value.

### 6. Positive Beam Normalisation.

As mentioned in section 6.2.1, the selection of events in the positive beam data which were produced by  $\pi^+ p$  interactions was defined by (PI .NOT. P) .AND. (C1 .OR. C2), and the pp interactions were defined by (P .NOT. PI). The calculation for the correction needed to determine the total number of incident  $\pi^+$ 's

and protons can be divided into two parts.

A correction for the (PI .NOT. P) or (P .NOT. PI) selection is necessary due to a significant number of high Pt events being produced with both the P and PI bits being set. These events had to be divided to produce fractions that were produced by a  $\pi^+$  with a spectator proton present, and by a proton with a spectator  $\pi^+$  present. This fraction was derived by using the number of selected high Pt events with the P bit set and the number of events with PI bit set, and the relative count rates of the PI and P scalers. This produced a correction of 1.026 for the proton sample and 1.078 for the  $\pi^+$  sample.

Secondly, for the  $\pi^+$  sample only, the correction due to the (C1 .OR. C2) cut was determined. This was produced by measuring the correlation between the PI bit and the C1, C2 bits for the high Pt events. This resulted in an additional correction of 1.84 being applied to the  $\pi^+$  sample.

### 6.3.2 Direct photon candidates

Additional corrections must be made for losses and contaminations in the direct photon sample.

#### 1. Charged particle contamination.

In the normal analysis, to remove the charged particles from the direct photon sample, the showers linked to TRIDENT tracks are removed and then the 4m chamber is used to search for three and four plane hits. To estimate the efficiency of these cuts, the order in which the cuts are applied was reversed. The efficiencies were calculated to be :- TRIDENT  $61 \pm 2\%$  and 4m chamber  $81 \pm 2\%$ . This value for the 4m chamber efficiency within error agrees with the value ( $85 \pm 2\%$ ) obtained by using the efficiencies of the individual planes calculated in Chapter 4.

Knowing the total number of charged particles rejected by the TRIDENT and 4m chamber cuts and also their individual rejection efficiencies, the charge particle contamination of the direct photon sample can be estimated.

## 2. Neutral hadron contamination.

Since the charged hadron contamination could be directly determined more easily, the best method to calculate the neutral hadron contamination, was to obtain the number of charged hadrons and use a previously measured value for the charged hadron to neutral hadron cross-section ratio [29] to give the neutral hadron contamination.

To determine the charged hadron contamination, the normal analysis program was run on the data with the 4m chamber cuts removed in both the direct photon selection and beam halo rejection. A search was then made for showers which had an extrapolated TRIDENT track within 3 cm. The ratio of track momentum/shower energy was calculated for such hits. The asymmetry in this distribution is presumed to have been produced by charged hadrons since the distribution will be symmetric for electrons. The calculated number of charged hadrons is then corrected knowing TRIDENT to be 61 % efficient and the number of neutral hadrons is produced by using the ratio of charged hadrons to neutral hadrons as mentioned previously.

Due to an uncertainty in accurately choosing the correct mean for this distribution, the systematic error has been estimated at 0.5 %.

## 3. Losses due to Strict Halo Cuts

As with the gentle halo cuts, the method used was to estimate the percentage loss of  $\pi^0$ 's and assume that the percentage direct photon loss was the same. As with the gentle halo cuts, no variation with Pt was observed, and the percentage loss was found to be greater in backward Xf.

#### 4. Losses due to charge particle misidentification

To estimate these losses the coordinates of the photon candidate are rotated through  $180^\circ$ , and the 4m chamber and TRIDENT cuts are applied normally, and in the reverse order. This provides an estimate of the background in the 4m chamber and TRIDENT, and this is used to provide the percentage of photons which have been wrongly identified as charged particles.

#### 6.4 *Monte Carlo simulation chain*

In all direct photon experiments, since the acceptance is not 100 % and due to the high photon background, it is necessary to use a good Monte Carlo to accurately calculate the various acceptances and backgrounds. WA70 used two different Monte Carlos, with entirely different approaches. The Monte Carlo used by the author was the Lund Monte Carlo and this will be discussed in the following section. The other Monte Carlo was based on the superimposing of a simulated high Pt direct photon or  $\pi^0$  onto a real event. The author used the Lund Monte Carlo for the calculation of detection efficiencies, since, for example, the other Monte Carlo took no account of the event topology. However, since the two Monte Carlos have such different approaches, they provide a useful cross check on the calculated detection efficiencies. This check will be considered further when discussing systematic errors (Section 6.5).

The Lund Monte Carlo process can be divided into 2 distinct parts;

- 1) Event generation,
- 2) Experimental simulation.

#### 6.4.1 Event generation

Events were generated using the Lund Monte Carlo (Pythia 4.2 [30], Jetset 6.2 [31]), with the parton scattering using the appropriate QCD diagrams and the fragmentation being provided by the Lund model [32]. For each of the different beam types, the program was run in two different modes;

Direct photon generation - using the two first order diagrams shown in chapter 1. This sample of events is used to estimate the direct photon detection efficiency.

Background generation - this produces high Pt partons, which fragment into particles which can decay to produce high Pt photons which could simulate direct photons. Obviously, this includes  $\pi^0$ 's and this sample can be used to calculate  $\pi^0$  detection efficiency and to estimate the direct photon background from  $\pi^0$  decay.

#### 6.4.2 Experimental simulation

The particles produced by the Lund generation are tracked through the magnetic field, and those particles hitting the calorimeter, generate showers. From the study of shower development in the WA70 experimental data, the vertex depth in the calorimeter of the showers was simulated by following an exponential distribution of mean  $1.3 X_0$  for photons,  $X_0$  for electrons and  $\lambda$  for hadrons, where  $X_0$  and  $\lambda$  are the mean radiation and absorption lengths of the materials in the calorimeter. The energy deposited by these showers is then used to generate ADC and TOF information.

The GLOBAL pattern recognition program is then run on this data to reconstruct the calorimeter showers.

The information produced in the wire chambers is simulated using the OMGEANT program [33]. This takes the positions and directions of the charged

particles and uses the measured efficiencies of the chambers to produce digitisings in the wire planes. The efficiencies used for the Omega chambers were;

A chambers	- 97 %
B chambers	- 95 %
Drift chambers	- 97 %
Single Y plane chambers	- 90 %

obtained from measurements in the WA67 experiment, and for the big chamber, the efficiencies used for the individual planes are given in Chapter 4.

The TRIDENT track reconstruction program is then run on the simulated wire chamber information. This finally produces data in the same format as the DST2 experimental data tapes.

Unfortunately, since this large chain of Monte Carlo programs involves running Lund, GLOBAL, OMGEANT and TRIDENT, a large amount of computer time is used. Consequently, this effects the statistics available for the detection efficiency calculation. Fortunately, the Lund program can be run with different Pt thresholds and so reasonable statistics were produced.

Most of the Monte Carlo events used in this thesis were generated using an IBM 4361, with the approximate time for the various stages, measured in events per hour, being;

Lund Direct photon events	1000
Lund Background events	120
GLOBAL :	8000
OMGEANT :	1500
TRIDENT :	2000

The time required to generate background events, including high Pt  $\pi^*$  and  $\eta$  generation, is so much greater than for direct photon generation since the program generates a high Pt parton then fragments it, before determining if the resultant

high Pt  $\pi^0$  or  $\eta$  is above the Pt threshold. Obviously a large amount of time is wasted in producing jets which do not contain a particle with sufficient Pt.

The total number of events used in the calculation of the detection efficiencies, was ;

	Direct Photon Events	Background Events
$\pi p$	52199	197643
$p p$	140372	117952

For a given bin of Xf and Pt, the detection efficiency for direct photons (or  $\pi^0$ 's) is defined as

$$\epsilon = \frac{\text{Number of direct photons reconstructed in bin}}{\text{Number of direct photons generated in bin}}$$

using the reconstructed, not generated, Pt and Xf in the numerator of this expression. The reconstructed quantities are used in order to allow for the leaking of particles between bins due to energy resolution effects etc.

The Monte Carlo efficiencies for the various Xf and Pt bins are shown in Tables 6.1 to 6.4. To reduce statistical errors, for the direct photon and  $\pi^0$  acceptance calculations, the Monte Carlo events produced using  $\pi^- p$  and  $\pi^+ p$  interactions were combined, as no difference in the detection efficiency was either expected or observed.

However, in this Monte Carlo process several losses cannot be properly simulated, and these must be calculated using the methods described in section 6.3.

## 6.5      *Systematic Errors*

The errors on all the direct photon and  $\pi^0$  results shown in the Tables and figures in this chapter are statistical only. The various sources of systematic errors are now described.

Early analysis of the data, performed before the final energy scale had been determined, showed that an alteration in the energy scale of 1 % produced a 10 % change in cross-section. Therefore, the 1 % error in the energy scale correction factor of 1.028, discussed in Chapter 5, produces a 10 % systematic error in the cross-sections.

As mentioned previously, the study of the acceptances produced using the two Monte Carlos gives a good estimate of the systematic error on the detection efficiencies calculated in this thesis. When the results of the two Monte Carlos were compared, systematic effects not exceeding 15 %, were found in the acceptance of certain bins.

## 6.6      $\gamma/\pi^0$ Ratios

The simplest results to produce, are the  $\gamma/\pi^0$  ratios for the different interactions. This is relatively straightforward to calculate, since many of the correction factors which need to be applied to produce direct photon and  $\pi^0$  cross-sections cancel, as they are common to both samples, and hence the statistical error in the resultant ratio is reduced.

The 'raw' direct photon and  $\pi^0$  samples are shown in Tables 6.5 to 6.7 for the different interactions. For these tables, the raw direct photon events are simply those which pass the cuts described above, whereas, the raw  $\pi^0$  signal has already been background subtracted. The error on the direct photon signal is taken as the square root of the signal.

The equation used to calculate the corrected number of direct photons for the  $\gamma/\pi^0$  ratio is

$$\gamma_{\text{corr}} = \frac{\gamma_{\text{seen}} - \left( \frac{\gamma}{\pi^0} \times \pi_{\text{seen}}^0 \right) \times F}{\gamma_{\text{eff}}}$$

The individual correction factors, used to produce F in the above equation were calculated to be;

1) Charged particle contamination	0.982 $\pm$ 0.001
2) Neutral hadron contamination	0.974 $\pm$ 0.005
3) Strict halo cut losses	
-0.45 < Xf < -0.15	1.049 $\pm$ 0.003
-0.15 < Xf < 0.	1.027 $\pm$ 0.002
0. < Xf < 0.45	1.017 $\pm$ 0.001
4) Charged particle misidentification losses	1.074 $\pm$ 0.007

To calculate the corrected number of  $\pi^0$ 's in the various Xf and Pt bins, the raw  $\pi^0$  signals for the different interactions, shown in Tables 6.5 - 6.7, are multiplied by the appropriate Monte Carlo  $\pi^0$  detection efficiency, shown in Tables 6.2 and 6.4. The  $\gamma$  efficiencies used in the above equation are shown in Tables 6.1 and 6.3.

The corrected direct photon and  $\pi^0$  totals can now be used to calculate the  $\gamma/\pi^0$  ratio. These are shown in Figs. 6.3 and 6.4, for  $|Xf| < 0.45$  and  $|Xf| < 0.15$  respectively.

As predicted by theory (Chapter 1.2), the ratios all rise with Pt, with the ratio being greater for  $\pi^- p$  than  $\pi^+ p$  interactions.

6.7      *Cross-sections*

To produce the total number of  $\pi^0$ 's and direct photons for the cross-section calculation, the corrected numbers given above, must be adjusted for some other losses in the analysis.

1) Gentle halo cut losses

$-0.45 < X_f < -0.15$	$1.085 \pm 0.005$
$-0.15 < X_f < 0.45$	$1.073 \pm 0.002$

2) Processing filters

Negative beam	$1.10 \pm 0.01$
Positive beam	$1.143 \pm 0.014$

3) $A_1, A_2$ , Veto	$1.07 \pm 0.02$
4) Non-target interaction events	$0.997 \pm 0.001$

5) Attenuation in target	$1.04$
6) Selection of clean positive beam sample	

$\pi^+$	$1.989$
p	$1.026$

The equations used to calculate the invariant cross-sections were,

$$\frac{d^2\sigma}{dX_f dP_t} = \frac{n_c m_p}{n_b \rho L \Delta X_f \Delta P_t}$$

where,  $n_c$  is the fully corrected number of particles seen,  $m_p$  is the proton mass,  $n_b$  is the total effective number of incident beam particles after correction for the attenuation along the target,  $\rho$  is the density of liquid hydrogen,  $L$  is the target length, 1m, and  $\Delta X_f$  and  $\Delta P_t$  are the ranges of the  $X_f$  and  $P_t$  bins, and

$$E \frac{d^3 \sigma}{d p^3} = \frac{1}{\pi \sqrt{s}} \frac{E_{cms}}{Pt} \frac{d^2 \sigma}{d Xf d Pt}$$

where,  $E_{cms}$  is the centre of mass energy of the particle.

### 6.7.1 $\pi^0$ Cross-sections.

The full  $Xf$  and  $Pt$  cross-section grids for  $\pi^0$  production are shown in Tables 6.8 - 6.10 for  $\pi^- p$ ,  $\pi^+ p$  and  $p p$  interactions, respectively.

In studying the  $Pt$  distribution of the  $\pi^0$  cross-sections in Tables 6.8 - 6.10, it is apparent that the cross-section for  $p p$  interactions is more steeply falling with  $Pt$  than those produced by  $\pi^-$  and  $\pi^+$  interactions. The variation of the  $\pi^0$  cross-section with  $Pt$  for  $|Xf| < 0.45$  is shown in Figs. 6.5a - 6.7a for  $\pi^- p$ ,  $\pi^+ p$  and  $p p$  production respectively, and similarly in Figs. 6.5b - 6.7b for  $|Xf| < 0.15$ . In these Figs., the experimental cross-sections are compared with cross-sections produced using the parametrisations calculated by NA3[34] and Donaldson[35]. The  $Pt$  distributions of these results do not appear to closely follow either of the two parametrisations, except that the slope of the curve favours the NA3 results, which agrees well with previously published comparisons [36]. The general disagreement is perhaps not surprising, since the Donaldson parametrisation was calculated from experimental results using beam momenta of 100 GeV/c and 200 GeV/c respectively, and the beam momentum for the NA3 experiment was 200 GeV/c.

Comparison of the  $Xf$  distributions of the three sets of cross-sections shows that in all  $Pt$  bands, as expected, for  $\pi^- p$  and  $\pi^+ p$  interactions, the  $\pi^0$  cross-section is greater in the forward  $Xf$  direction. The  $Xf$  distribution for the  $p p$  interactions is, as expected, within error, symmetric about 0.

The Xf distribution for  $4.0 \text{ GeV/c} < Pt < 4.5 \text{ GeV/c}$  is shown in Fig. 6.8 for all three interactions, and is again compared with the Donaldson and NA3 parametrisations. Again, the comparison is not expected to be exact, but the data does follow the general shape of the parametrisations.

### 6.7.2 Direct Photon Cross-sections.

The full Xf and Pt grids for direct photon production in  $\pi^- p$ ,  $\pi^+ p$  and pp interactions are shown in Tables 6.11 - 6.13 respectively.

Again, as with the  $\pi^0$  cross-sections, when the general Pt distributions for the three interactions are compared, the cross-section for pp production is falling more steeply. The Pt distribution for  $|Xf| < 0.45$  is shown in Figs. 6.9a - 6.11a for  $\pi^- p$ ,  $\pi^+ p$  and pp interactions respectively, and similarly in Figs. 6.9b - 6.11b for  $|Xf| < 0.15$ . In these Figs. the results are compared with the fully optimised cross-sections given by the second order calculations of Aurenche using the Set I and Set II structure functions. Generally, in both Xf bands and for all Pt bins the results are in remarkably good agreement with the predictions produced using the Set I structure functions.

The Xf distributions for direct photon production for the three interactions for  $4.0 \text{ GeV/c} < Pt < 4.5 \text{ GeV/c}$  is shown in Fig. 6.12. Again, these results strongly favour the Set I structure functions.

These results, for both Xf and Pt distributions, in  $\pi^- p$ ,  $\pi^+ p$  and pp interactions agree totally with the findings of all the other direct photon experiments presenting results on the gluon structure functions, as described in Chapter 1.6.

### 6.7.3 $\pi^-/\pi^+$ Cross-sections ratios.

The Pt distribution for the ratio

$(\pi^- p \rightarrow \gamma + X) / (\pi^+ p \rightarrow \gamma + X)$  for  $|Xf| < 0.45$  is shown in Fig. 6.13a, and the similar distribution for  $\pi^0$  production is shown in Fig. 6.13b. Although there is some evidence that this ratio for direct photon production is increasing, the statistics are clearly not good enough for any clear conclusion to be drawn. The distribution for the  $\pi^0$  production ratio appears to be flat, but again no clear conclusion can be drawn.

## 6.8 Conclusions

The main aim of this thesis was to present cross-sections for direct photon and  $\pi^0$  production in  $\pi^- p$ ,  $\pi^+ p$  and  $p p$  interactions, and compare these with predicted theoretical values and previous experimental results.

For  $\pi^0$  production, the results were compared with predictions from two previous experiments. The results did not follow either set of predictions very closely, but this was not surprising since these experiments were performed at different momenta, and their predictions had been extended beyond their intended range.

The  $\gamma/\pi^0$  ratios for all three interactions clearly increased with Pt, as predicted by theory and seen in previous experiments.

The direct photon cross-sections provided the real quantitative test of QCD. In all cases, in both  $Xf$  and Pt distributions, the results obtained favoured the theoretical values produced using the Set I structure functions. This result was also in agreement with results presented by other experiments.

The ratio of  $\pi^-/\pi^+$  produced direct photon cross-sections was expected to increase with Pt. However, with the limited statistics available, this prediction

was neither confirmed nor refuted. Results presented by the WA70 collaboration [19], using data taken in both the 1984 and 1985 experimental runs, suggest that this ratio is only weakly dependent on Pt.

In general, the results produced are in strong agreement with the theoretical predictions produced by QCD.

Table 6.1

Pion data

Direct photon detection efficiency  
(% Error)

Pt (GeV/c)	Xf				
	-0.45 -0.15	-0.15 0	0 0.15	0.15 0.45	
4.0-4.5	57.7 (3.5)	64.8 (3.1)	60.3 (2.9)	49.6 (2.4)	
4.5-5.0	54.4 (5.6)	69.7 (5.7)	54.3 (4.6)	57.8 (4.4)	
5.0-5.5	62.8 (3.2)	64.8 (2.8)	63.3 (2.6)	55.9 (2.2)	
5.5-6.0	66.4 (5.3)	72.8 (5.1)	64.7 (4.5)	55.6 (3.5)	
6.0-7.0	72.9 (8.3)	69.2 (7.2)	61.5 (5.5)	58.5 (5.3)	
5.5-6.5	66.5 (4.6)	71.4 (4.4)	64.3 (3.7)	54.4 (2.9)	

Table 6.2

Pion data

$\pi^0$  detection efficiency  
(% Error)

Pt (GeV/c)	Xf				
	-0.45 -0.15	-0.15 0	0 0.15	0.15 0.45	
4.0-4.5	45.5 (6.9)	62.9 (5.0)	62.1 (4.7)	54.8 (4.4)	
4.5-5.0	60.6 (9.9)	67.6 (9.2)	66.9 (7.9)	44.6 (8.3)	
5.0-5.5	55.3 (2.7)	60.5 (2.1)	58.6 (1.9)	53.4 (1.8)	
5.5-6.0	62.0 (4.5)	66.0 (3.4)	57.0 (3.3)	59.7 (3.1)	
6.0-7.0	59.2 (6.6)	63.5 (6.4)	64.7 (5.2)	51.9 (5.0)	
5.5-6.5	61.1 (3.9)	63.3 (3.1)	58.9 (2.9)	57.6 (2.7)	

Table 6.3

Proton data

Direct Photon detection efficiency  
(% Error)

Pt (GeV/c)	Xf				
	-0.35 -0.15	-0.15 0	0 0.15	0.15 0.35	
4.0-4.5	59.2 (1.2)	65.6 (1.1)	61.2 (1.1)	52.7 (1.2)	
4.5-5.0	68.5 (2.5)	67.3 (2.1)	61.6 (1.9)	56.1 (2.1)	
5.0-5.5	67.5 (2.9)	66.9 (2.4)	62.5 (2.4)	54.5 (2.7)	
5.5-6.0	65.2 (5.5)	73.4 (5.1)	69.1 (4.8)	63.0 (5.4)	
6.0-7.0	75.0 ( 10)	65.6 (8.4)	57.3 (7.5)	62.8 (8.8)	

Table 6.4

Proton data

$\pi^0$  detection efficiency  
(% Error)

Pt (GeV/c)	Xf				
	-0.45	-0.15	0	0.15	0.45
4.0-4.5	48.0 (3.1)	58.0 (2.3)	56.2 (2.4)	46.7 (3.3)	
4.5-5.0	55.8 (6.2)	63.4 (4.8)	57.7 (4.3)	55.8 (6.5)	
5.0-5.5	61.5 (5.4)	62.5 (4.4)	62.6 (4.5)	57.9 (5.8)	
5.5-6.0	67.6 (9.2)	59.7 (9.2)	58.7 (9.1)	55.1 (12)	
6.0-7.0	53.1 (20)	75.5 (16)	59.7 (17)	46.5 (23)	

Table 6.5

$\pi^- p$  Interactions

Raw direct photons

		Xf			
Pt (GeV/c)		-0.45 -0.15	-0.15 0	0 0.15	0.15 0.45
4.0-4.5		357	520	515	488
4.5-5.0		135	178	181	203
5.0-5.5		46	68	52	74
5.5-6.0		25	29	25	38
6.0-7.0		8	14	14	15

Raw  $\pi^0$   
(% Error)

		Xf			
Pt (GeV/c)		-0.45 -0.15	-0.15 0	0 0.15	0.15 0.45
4.0-4.5		1508 (2.7)	2368 (2.1)	2741 (2.0)	2587 (2.1)
4.5-5.0		444 (4.9)	661 (4.0)	732 (3.8)	829 (3.6)
5.0-5.5		137 (8.8)	196 (7.3)	204 (7.2)	241 (6.6)
5.5-6.0		29 (19)	43 (16)	57 (14)	58 (14)
6.0-7.0		16 (25)	17 (24)	20 (23)	22 (21)

Table 6.6

$\pi^+ p$  Interactions

Raw Direct Photons

		Xf			
Pt (GeV/c)		-0.45 -0.15	-0.15 0	0 0.15	0.15 0.45
4.0-4.5		81	116	85	94
4.5-5.0		25	23	27	30
5.0-5.5		6	9	4	7
5.5-6.5		6	3	5	4

Raw  $\pi^+$   
(% Error)

		Xf			
Pt (GeV/c)		-0.45 -0.15	-0.15 0	0 0.15	0.15 0.45
4.0-4.5		339 (5.6)	625 (4.1)	659 (4.1)	566 (4.4)
4.5-5.0		107 ( 10)	163 (8.1)	223 (6.8)	190 (7.4)
5.0-5.5		31 ( 19)	45 ( 15)	58 ( 13)	44 ( 15)
5.5-6.5		8 ( 38)	11 ( 30)	15 ( 26)	10 ( 32)

Table 6.7  
pp Interactions

Raw Direct Photons

		Xf			
Pt (GeV/c)		-0.35 -0.15	-0.15 0	0 0.15	0.15 0.35
4.0-4.5		358	445	378	178
4.5-5.0		124	116	91	59
5.0-5.5		26	31	22	14
5.5-6.0		7	4	7	5
6.0-7.0		4	3	4	2

Raw  $\pi^0$   
(% Error)

		Xf			
Pt (GeV/c)		-0.35 -0.15	-0.15 0	0 0.15	0.15 0.35
4.0-4.5		1884 (2.4)	2875 (1.9)	2874 (1.9)	1538 (2.7)
4.5-5.0		441 (4.9)	664 (4.0)	662 (4.0)	352 (5.6)
5.0-5.5		106 (10)	140 (8.7)	140 (8.6)	64 (13)
5.5-6.0		26 (19)	29 (19)	38 (17)	18 (24)
6.0-7.0		8 (38)	11 (30)	9 (33)	2 (70)

Table 6.8

$\pi^- p$

$\pi^0$  cross-section (nb/GeV<sup>2</sup>/c<sup>3</sup>)  
(% Error)

		Xf			
Pt (GeV/c)		-0.45 -0.15	-0.15 0	0 0.15	0.15 0.45
4.0-4.5		.33 (7.7)	.65 (5.8)	.76 (5.5)	.50 (5.3)
4.5-5.0		.074 ( 12)	.17 ( 10)	.19 (9.1)	.19 (9.3)
5.0-5.5		.024 (9.4)	.056 (7.9)	.060 (7.7)	.044 (7.1)
5.5-6.0		.0045 ( 20)	.011 ( 16)	.017 ( 14)	.0095 ( 14)
6.0-7.0		.0013 ( 26)	.0023 ( 25)	.0026 ( 23)	.0020 ( 22)

Table 6.9

$\pi^+ p$

$\pi^+$  cross-section (nb/GeV<sup>2</sup>/c<sup>3</sup>)  
(% Error)

		Xf			
Pt (GeV/c)		-0.45 -0.15	-0.15 0	0 0.15	0.15 0.45
4.0-4.5	.25 (9.1)	.57 (6.8)	.61 (6.6)	.36 (6.5)	
4.5-5.0	.059 (15)	.14 (12)	.19 (11)	.14 (11)	
5.0-5.5	.018 (19)	.042 (15)	.056 (14)	.027 (16)	
5.5-6.5	.0021 (38)	.0049 (30)	.0072 (26)	.0028 (32)	

Table 6.10

pp

$\pi^0$  cross-section (nb/GeV<sup>2</sup>/c<sup>3</sup>)  
(% Error)

		Xf			
Pt (GeV/c)		-0.35 -0.15	-0.15 0	0 0.15	0.15 0.35
4.0-4.5		.32 (4.4)	.46 (3.7)	.47 (3.7)	.27 (4.7)
4.5-5.0		.062 (8.2)	.097 (6.6)	.11 (6.3)	.050 (8.8)
5.0-5.5		.013 (12)	.021 (10)	.021 (9.9)	.0085 (15)
5.5-6.0		.0029 (22)	.0045 (21)	.0059 (19)	.0025 (27)
6.0-7.0		.00056 (42)	.00067 (34)	.00069 (37)	.00016 (74)

Table 6.11

$\pi^- p$

Direct photon cross-section (nb/GeV<sup>2</sup>/c<sup>3</sup>)  
(% Error)

		Xf			
Pt (GeV/c)		-0.45 -0.15	-0.15 0	0 0.15	0.15 0.45
4.0-4.5		.035 ( 29)	.089 ( 19)	.081 ( 23)	.077 ( 15)
4.5-5.0		.022 ( 22)	.042 ( 15)	.053 ( 17)	.026 ( 25)
5.0-5.5		.0054 ( 25)	.014 ( 20)	.011 ( 22)	.010 ( 18)
5.5-6.0		.0035 ( 24)	.0064 ( 24)	.0058 ( 28)	.0062 ( 21)
6.0-7.0		.00051 ( 40)	.0017 ( 33)	.0019 ( 32)	.0011 ( 34)

Table 6.12

$\pi^+ p$

Direct photon cross-section (nb/GeV<sup>2</sup>/c<sup>3</sup>)  
(% Error)

		Xf			
Pt (GeV/c)		-0.45 -0.15	-0.15 0	0 0.15	0.15 0.45
4.0-4.5		.027 ( 39)	.058 ( 32)	.026 ( 70)	.046 ( 25)
4.5-5.0		.013 ( 39)	.017 ( 35)	.023 ( 40)	.010 ( 61)
5.0-5.5		.0018 ( 90)	.0047 ( 70)	.00055 (421)	.0023 ( 81)
5.5-6.5		.0014 ( 46)	.00094 ( 85)	.0018 ( 62)	.0010 ( 66)

Table 6.13

pp

Direct photon cross-section (nb/GeV<sup>2</sup>/c<sup>3</sup>)  
(% Error)

		Xf			
Pt (GeV/c)		-0.35 -0.15	-0.15 0	0 0.15	0.15 0.35
4.0-4.5		.033 ( 15)	.028 ( 22)	.029 ( 20)	.013 ( 33)
4.5-5.0		.011 ( 21)	.0088 ( 33)	.0067 ( 41)	.0041 ( 53)
5.0-5.5		.0024 ( 32)	.0038 ( 25)	.0021 ( 47)	.0014 ( 49)
5.5-6.0		.00073 ( 52)	.00025 (143)	.00082 ( 54)	.00058 ( 54)
6.0-7.0		.00019 ( 65)	.00013 (132)	.00027 ( 79)	.00011 ( 92)

*Figures - Chapter 6*

Fig. 6.1

Asymmetry of electromagnetic shower pairs.

Fig. 6.2

Invariant mass for electromagnetic shower pairs with asymmetry less than 90 %.

Fig. 6.3

$\gamma/\pi^0$  ratios for  $\pi^- p$ ,  $\pi^+ p$  and  $p p$  interactions with  $|Xf| < 0.45$ .

Fig. 6.4

$\gamma/\pi^0$  ratios for  $\pi^- p$ ,  $\pi^+ p$  and  $p p$  interactions with  $|Xf| < 0.15$ .

Fig. 6.5

Cross-sections for  $\pi^0$  production in  $\pi^- p$  interactions, for (a)  $|Xf| < 0.45$ , (b)  $|Xf| < 0.15$ . The solid triangles are the predictions produced using the NA3 parametrisation and the solid circles are produced using the Donaldson parametrisation.

Fig. 6.6

Cross-sections for  $\pi^0$  production in  $\pi^+ p$  interactions, for (a)  $|Xf| < 0.45$ , (b)  $|Xf| < 0.15$ . The solid triangles and circles have the same meaning as before.

Fig. 6.7

Cross-sections for  $\pi^0$  production in  $p p$  interactions, for (a)  $|Xf| < 0.35$ , (b)  $|Xf| < 0.15$ . The solid triangles and circles have the same meaning as before.

Fig. 6.8

$\pi^0$  cross-sections as a function of  $X_f$ , in the  $P_t$  range 4.0-4.5 GeV/c. The solid triangles and circles have the same meaning as before.

Fig. 6.9

Cross-sections for direct photon production in  $\pi^- p$  interactions, for (a)  $|X_f| < 0.45$ , (b)  $|X_f| < 0.15$ . The open triangles are the predictions produced using the Set I structure functions and the open squares are produced using the Set II structure functions.

Fig. 6.10

Cross-sections for direct photon production in  $\pi^+ p$  interactions, for (a)  $|X_f| < 0.45$ , (b)  $|X_f| < 0.15$ . The triangles and squares have the same meaning as before.

Fig. 6.11

Cross-sections for direct photon production in  $p p$  interactions, for (a)  $|X_f| < 0.35$ , (b)  $|X_f| < 0.15$ . The triangles and squares have the same meaning as before.

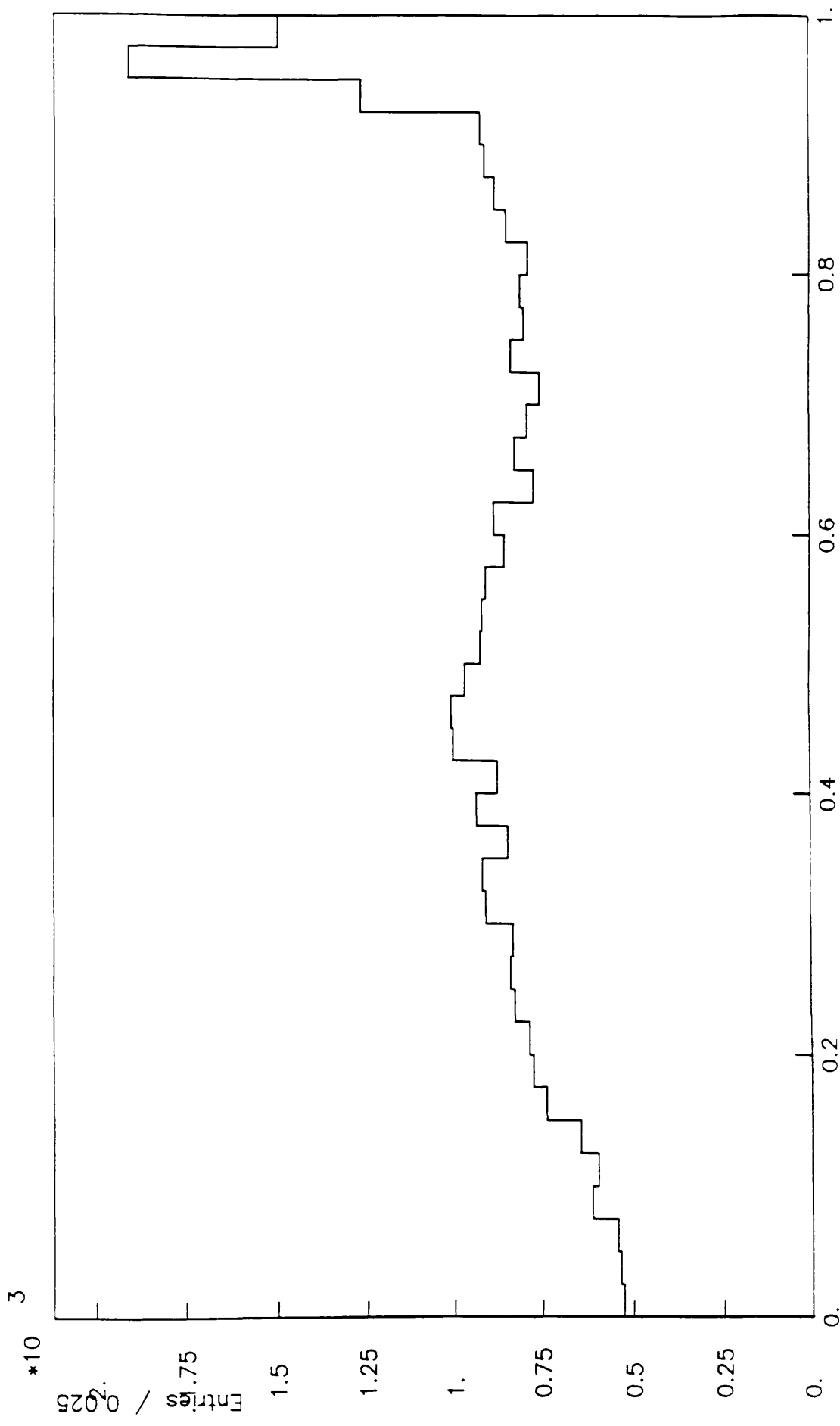
Fig. 6.12

Direct photon cross-sections as a function of  $X_f$ , in the  $P_t$  range 4.5-4.5 GeV/c. The triangles and squares have the same meaning as before.

Fig. 6.13

Ratio of cross-sections ( $\pi^-$  beam /  $\pi^+$  beam) for direct photon and  $\pi^0$  production with  $|X_f| < 0.45$ . The open triangles, open squares, solid triangles and solid circles have the same meaning as before.

Fig. 6.1



\*10<sup>3</sup>

Entries / 0.01 (GeV/c)

0.6

0.4

0.2

0.

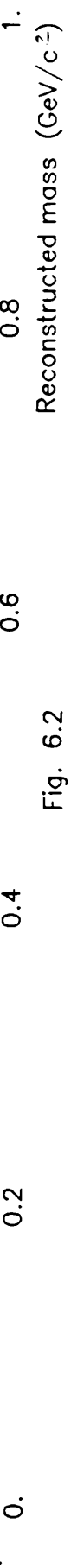


Fig. 6.2

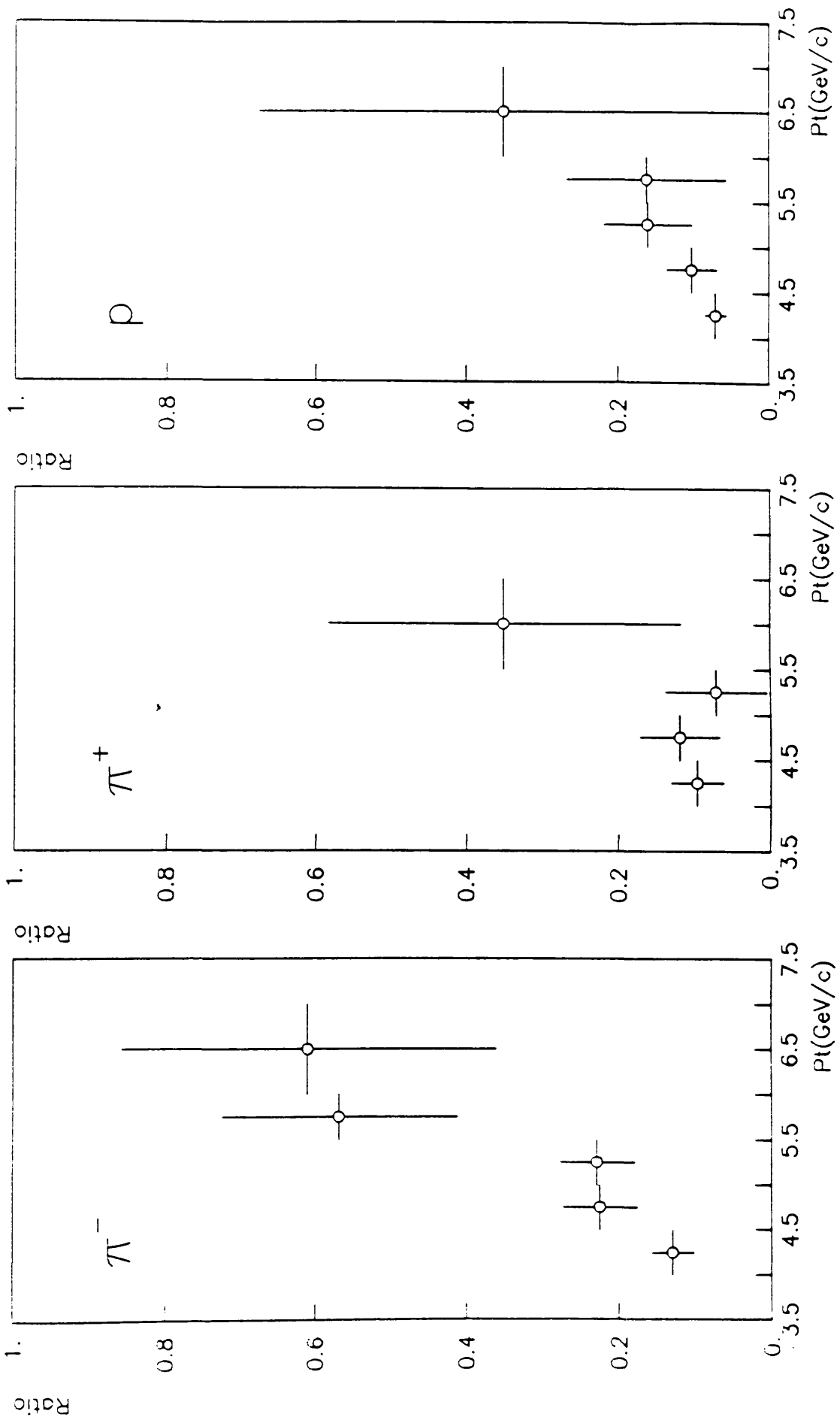


Fig. 6.3

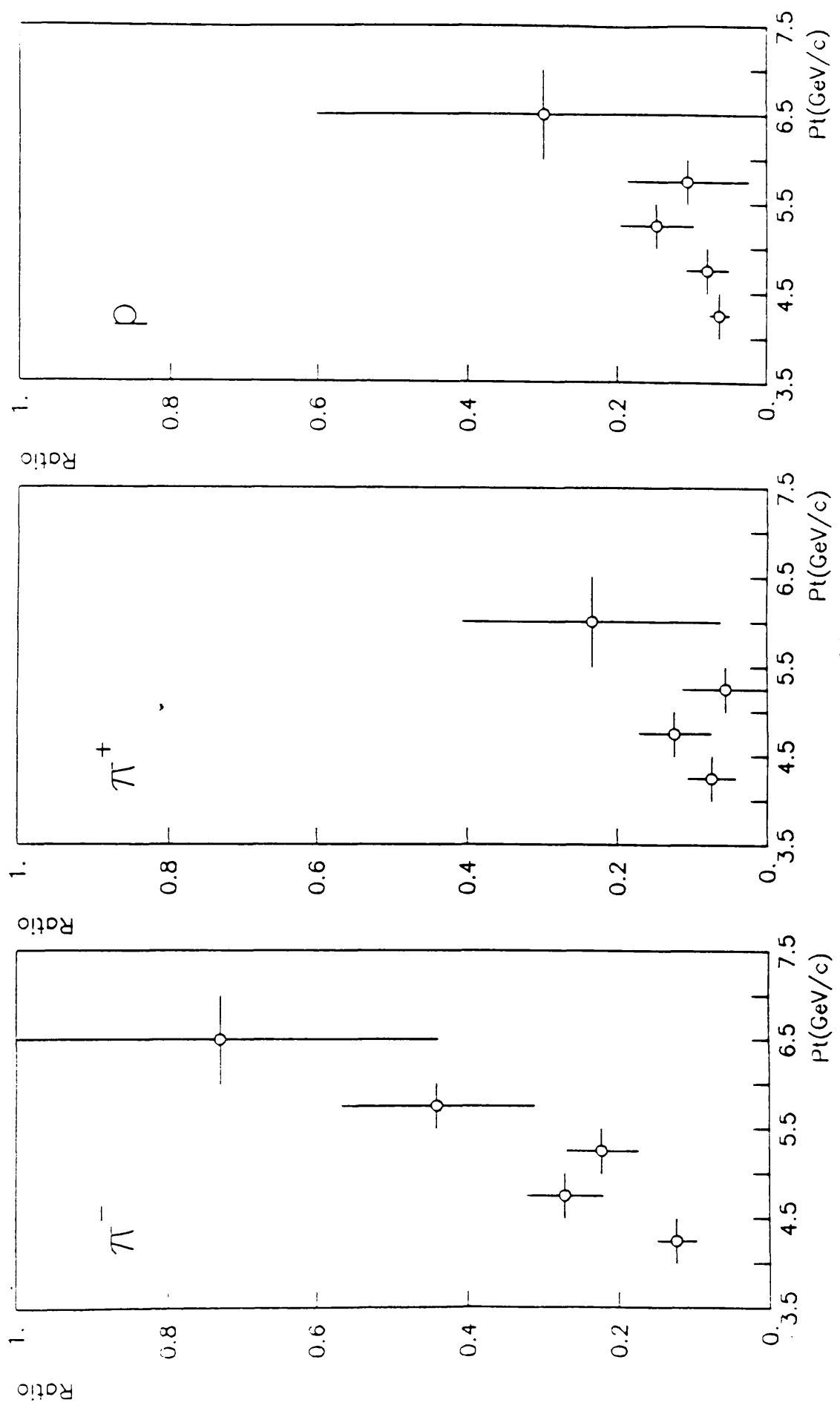


Fig. 6.4

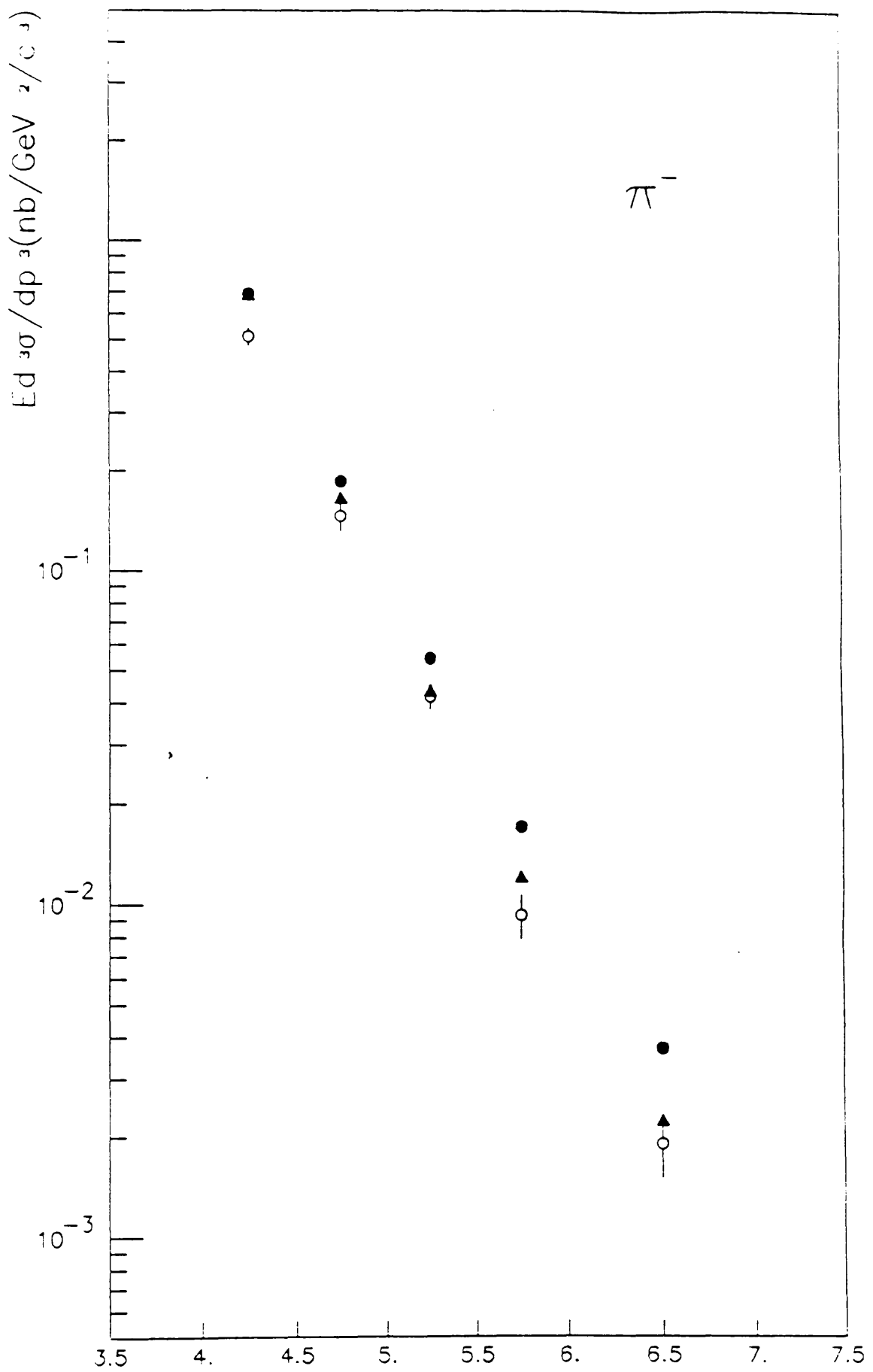


Fig. 6.5a

$P_T (\text{GeV}/c)$

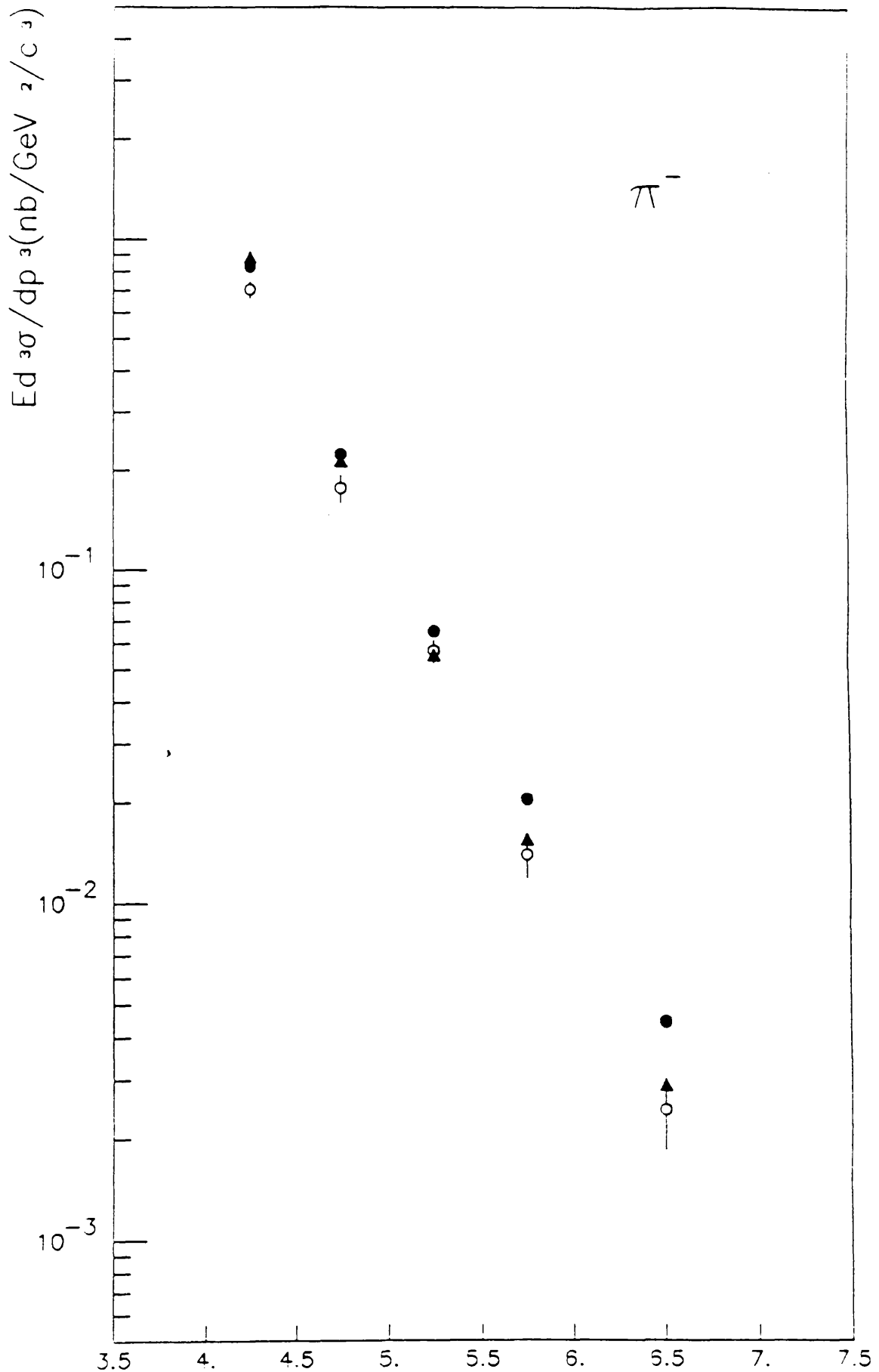


Fig. 6.5b

$Pt$  (GeV/c)

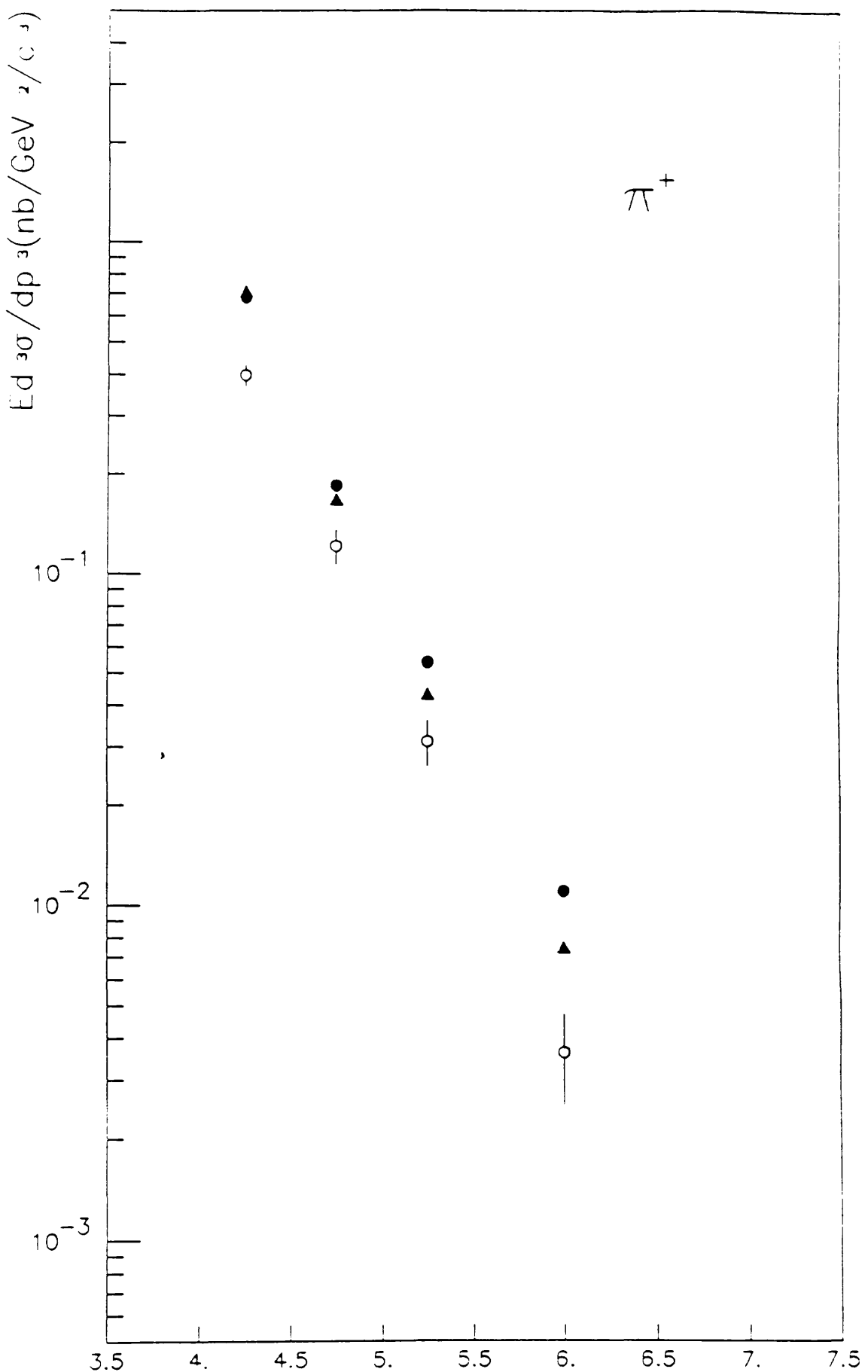


Fig. 6.6a

$Pt$  (GeV/c)

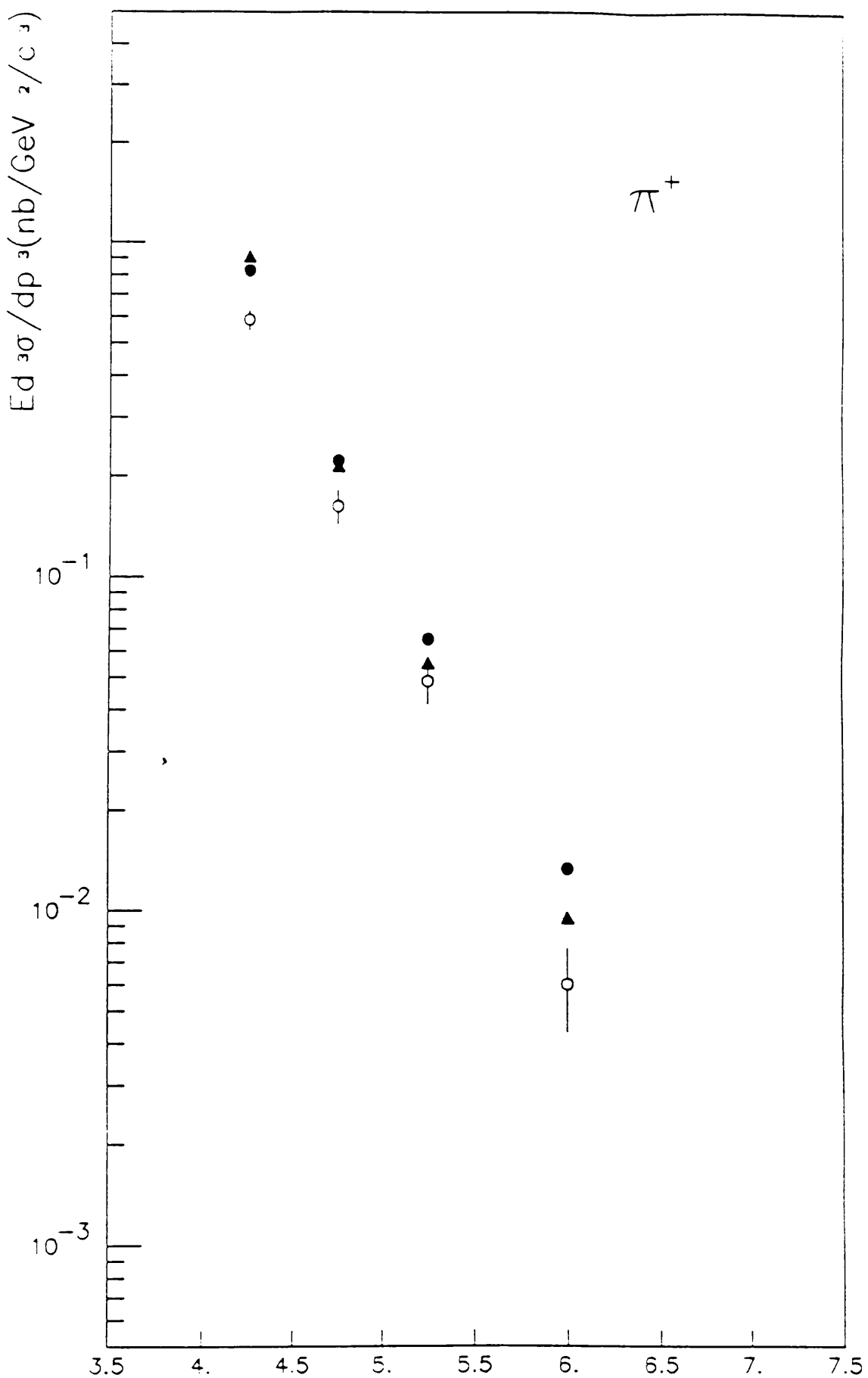


Fig. 6.6b

$Pt$  (GeV/c)

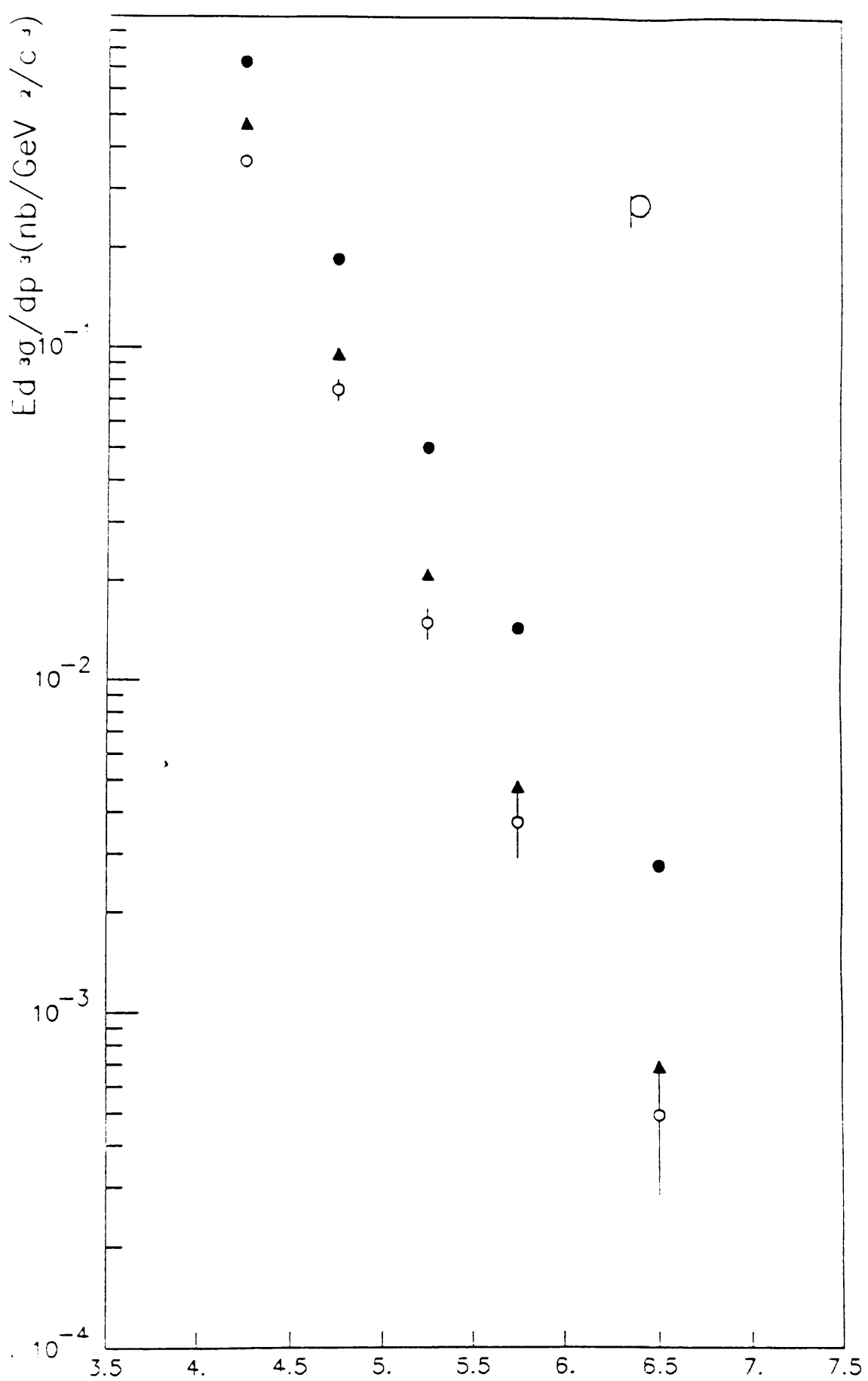


Fig. 6.7a

$\sqrt{s}$  (GeV/c)

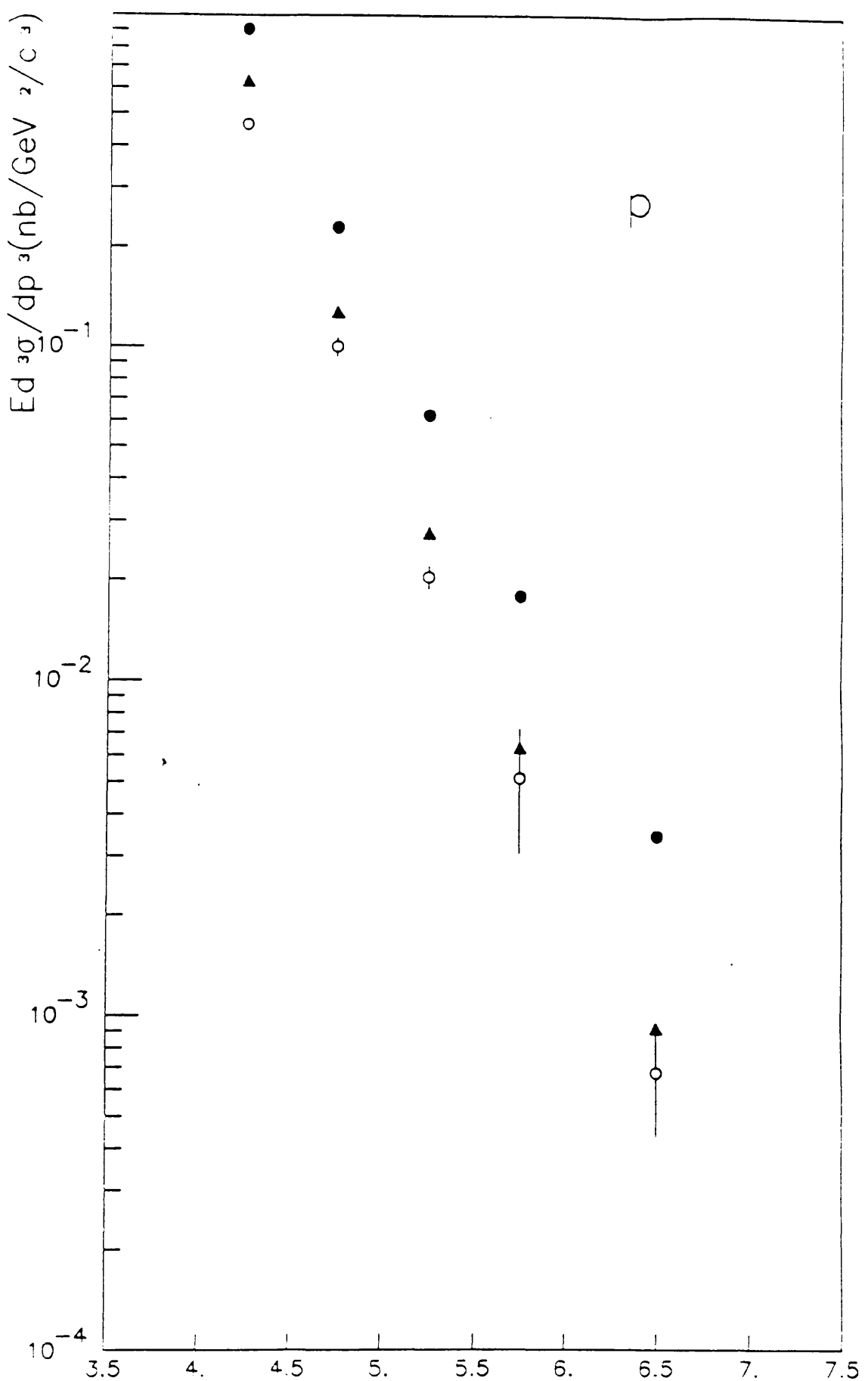


Fig. 6.7b

$Pt$  (GeV/c)

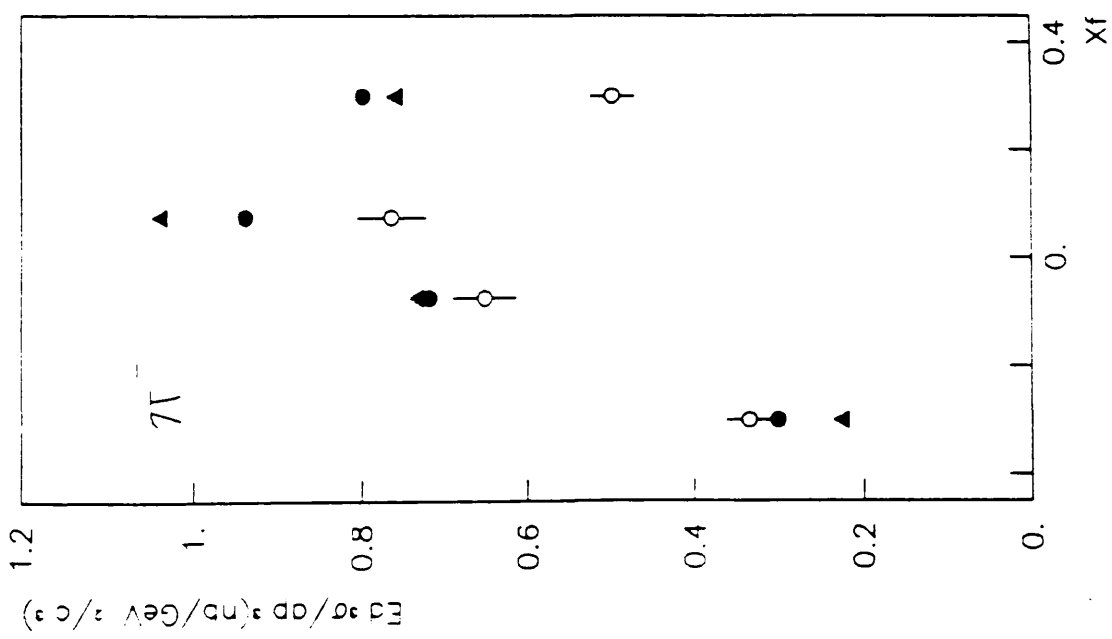
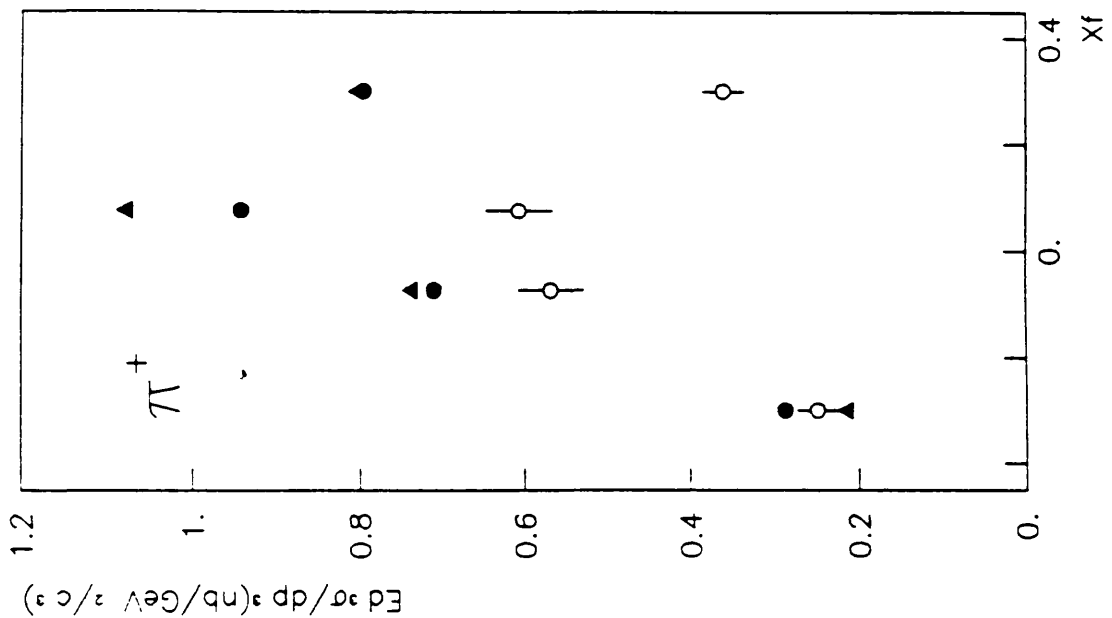
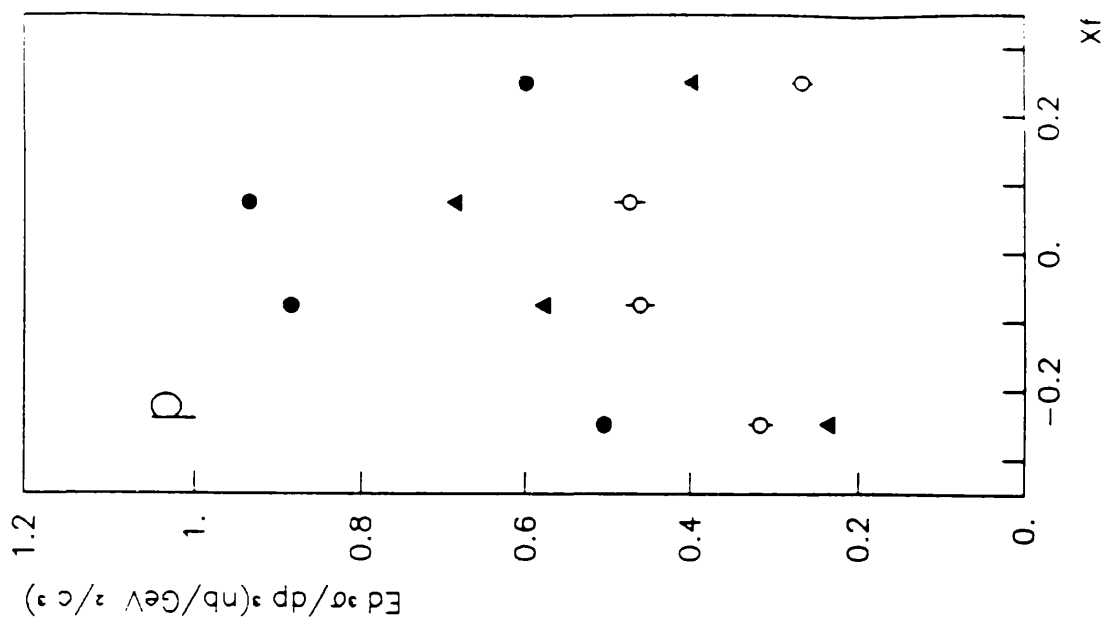


Fig. 6.8

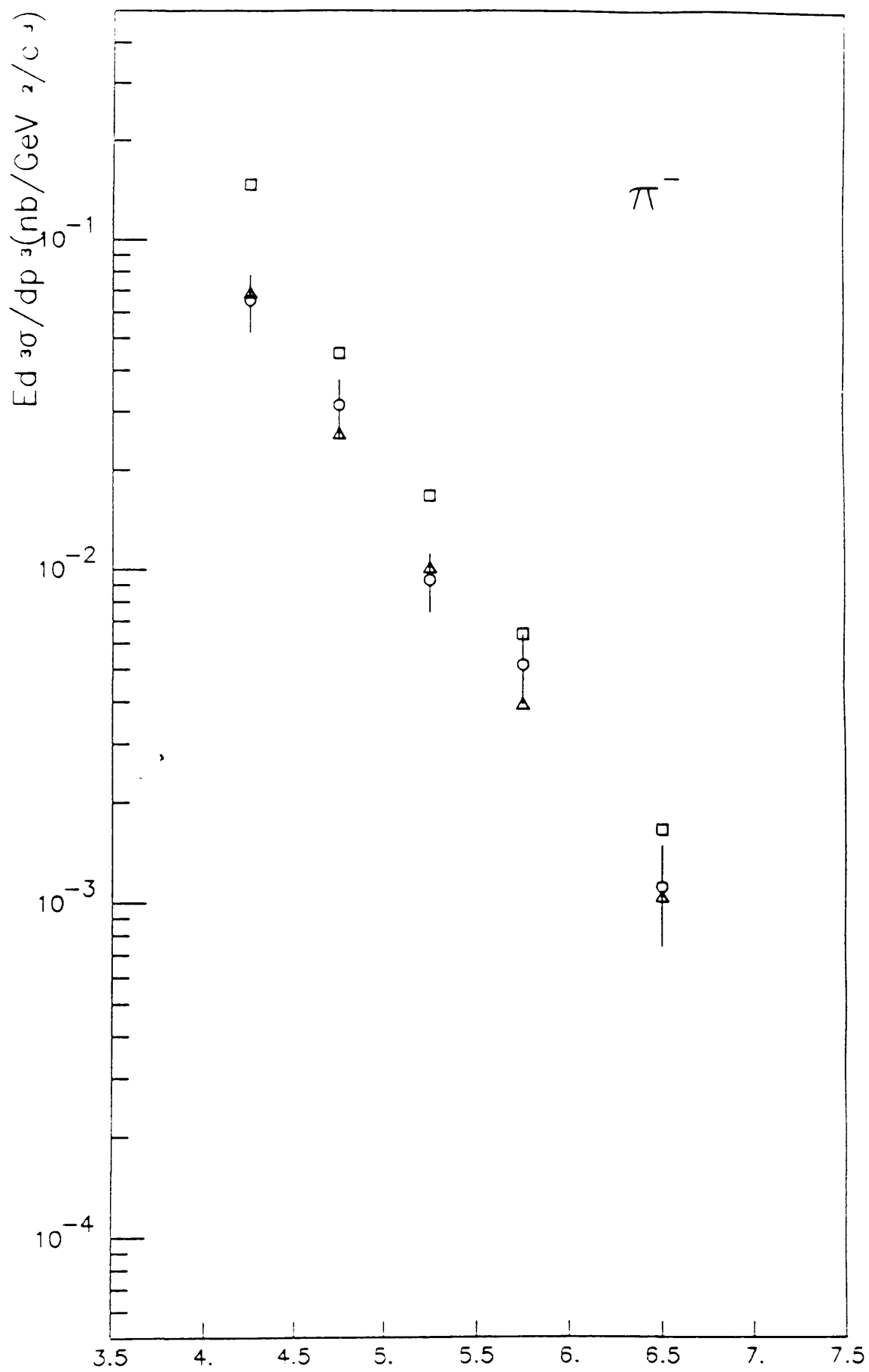


Fig. 6.9a

 $Pt(\text{GeV}/c)$

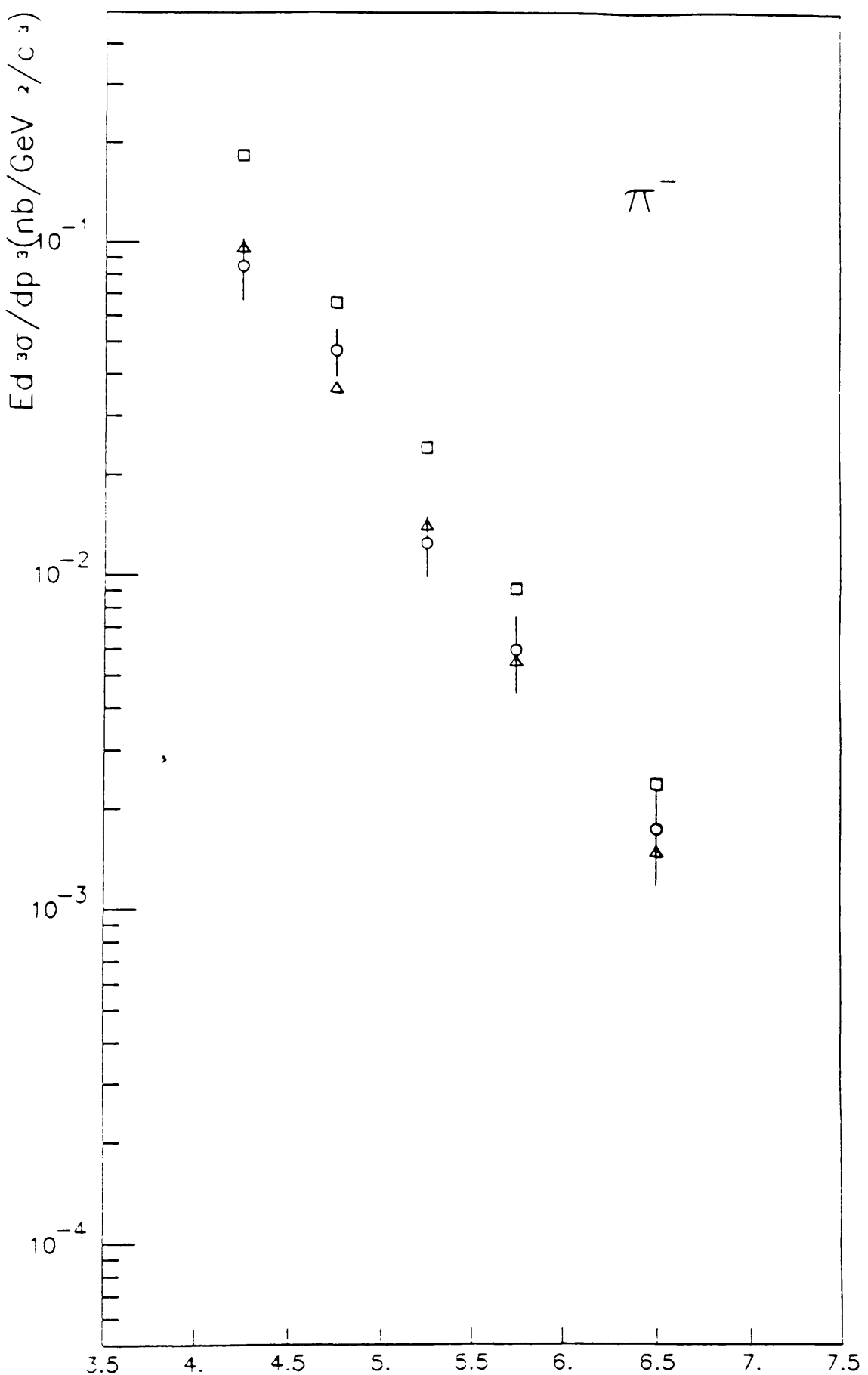


Fig. 6.9b

$\pi^-$

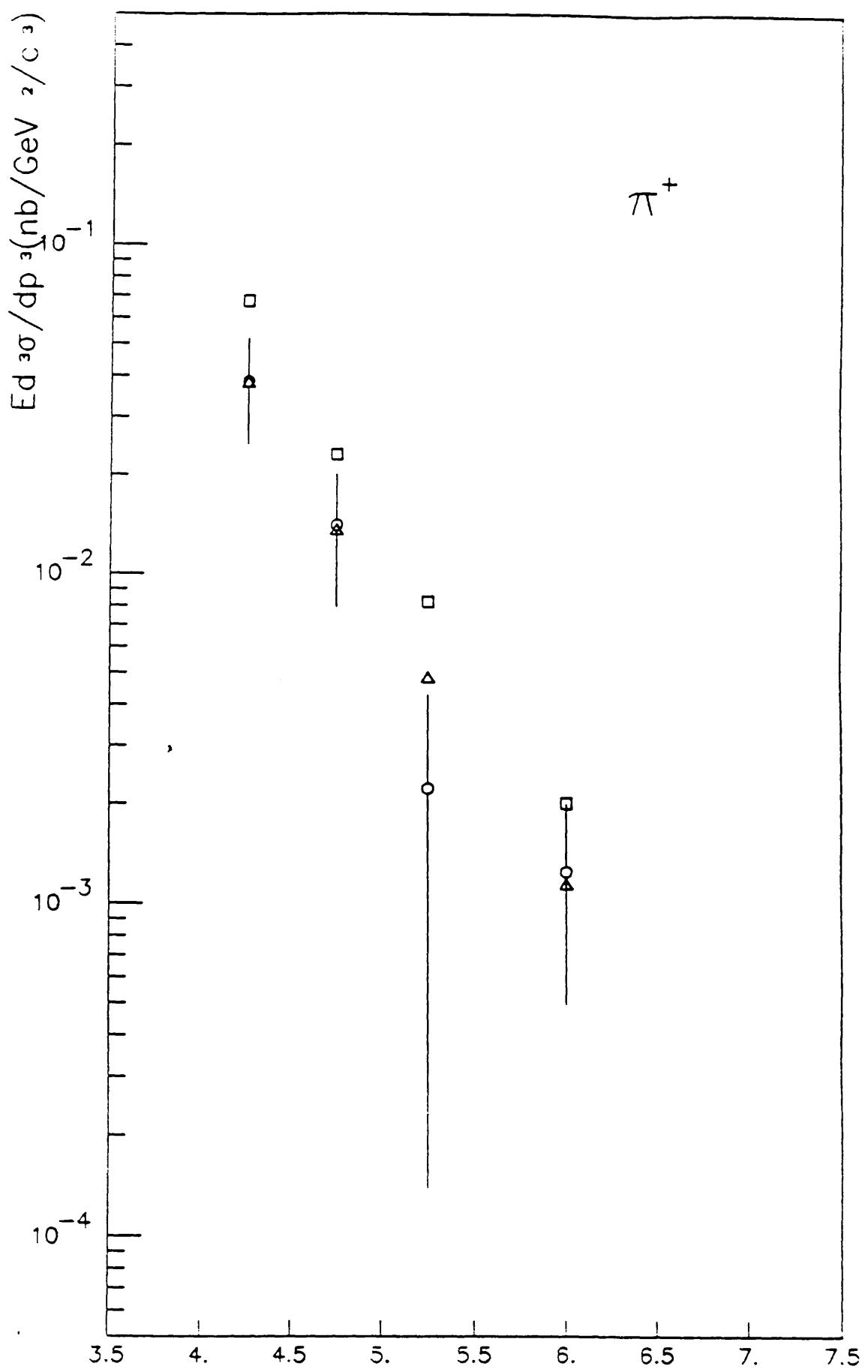


Fig. 6.10a

$Pt \text{ (GeV/c)}$

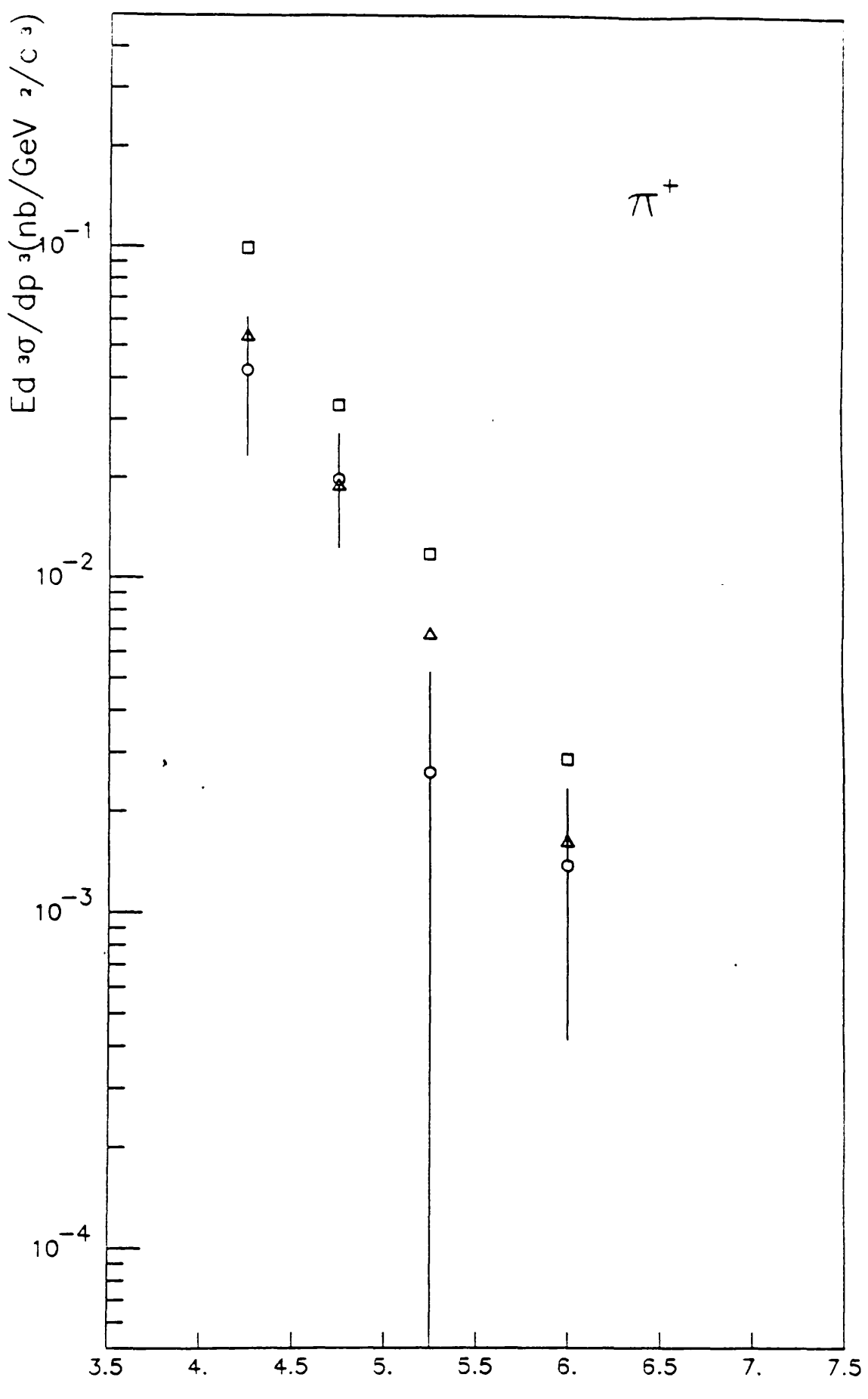


Fig. 6.10b

$\pi^+$

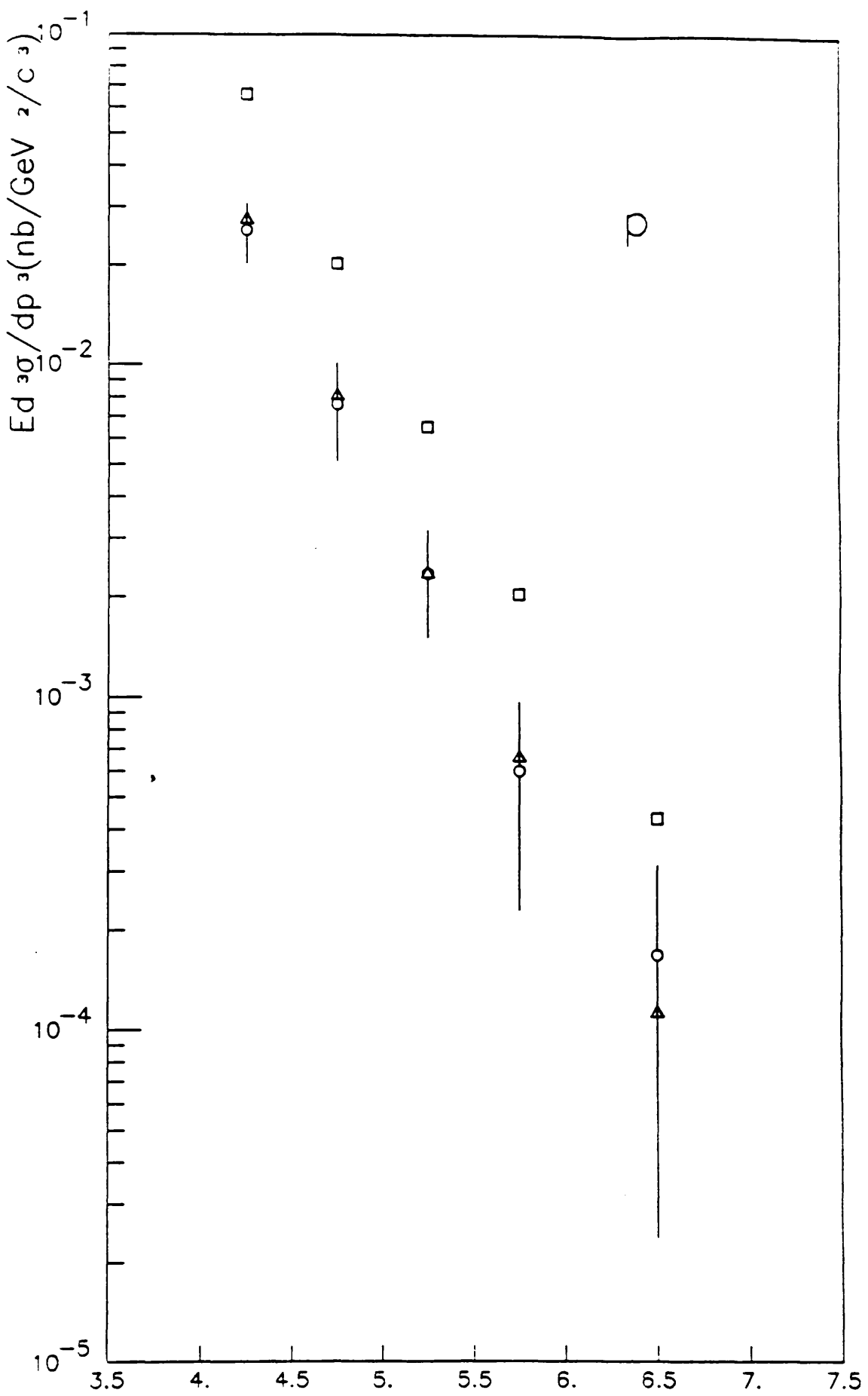


Fig. 6.11a

$Pt$ (GeV/c)

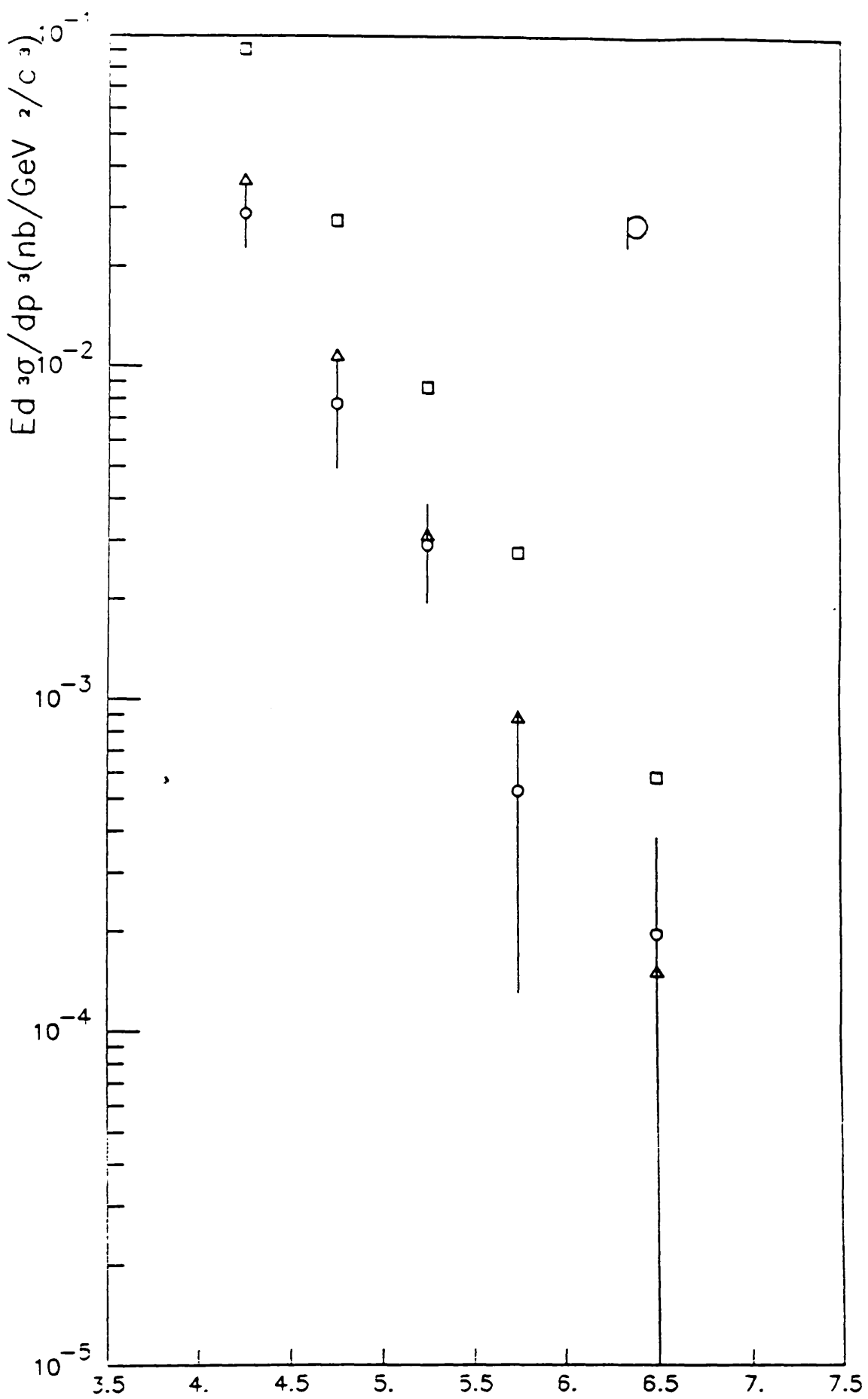


Fig. 6.11b

$Pt(\text{GeV}/c)$

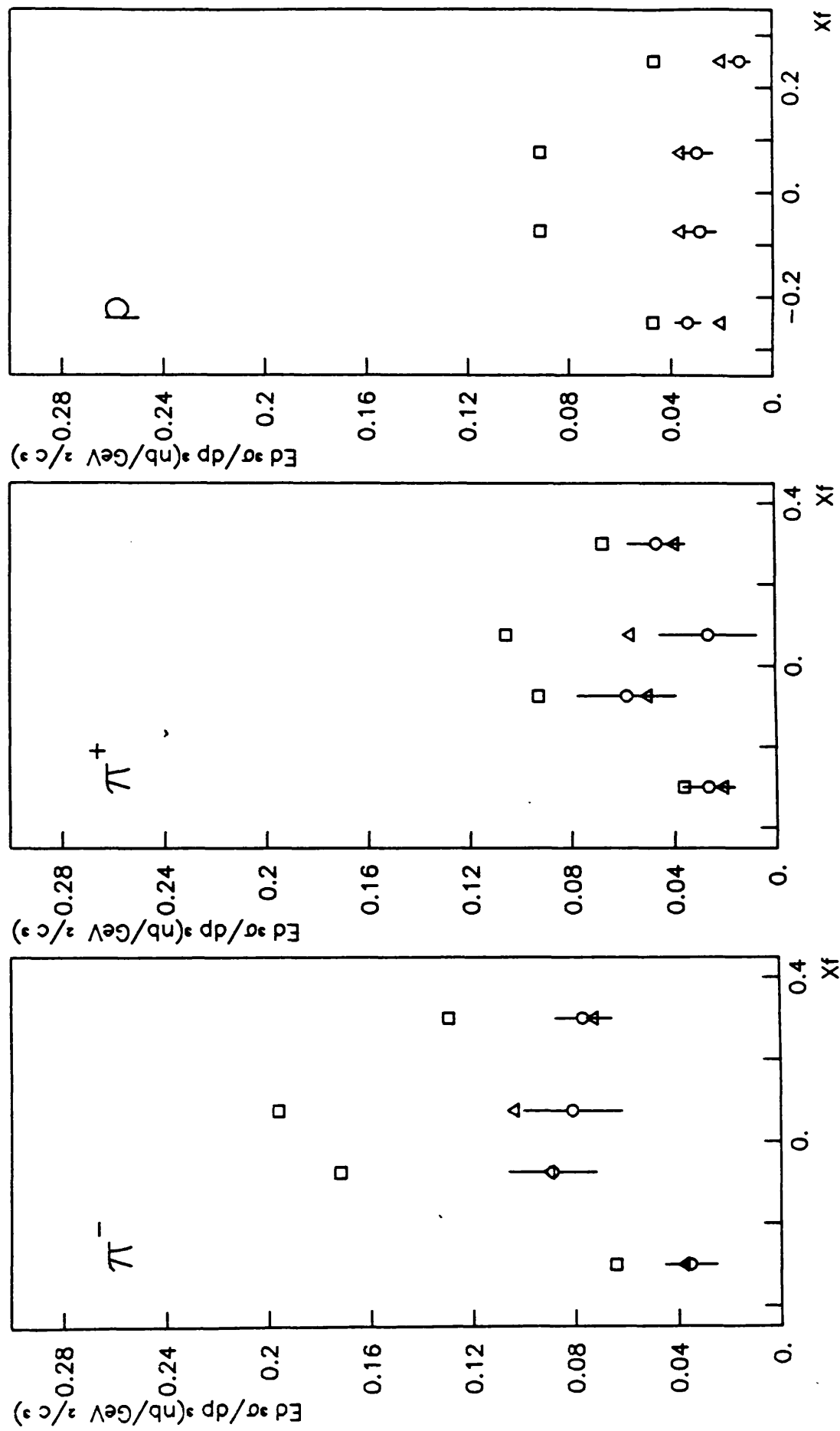


Fig. 6.12

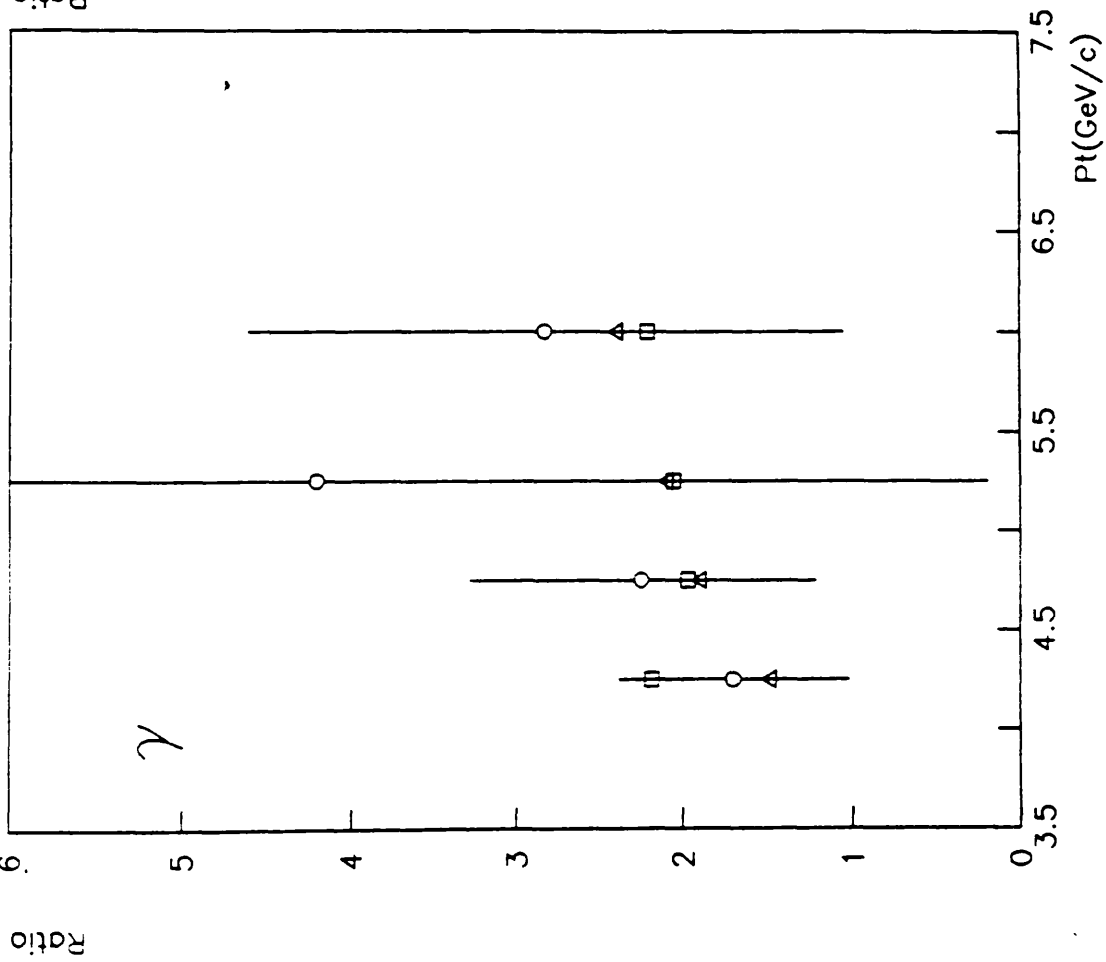
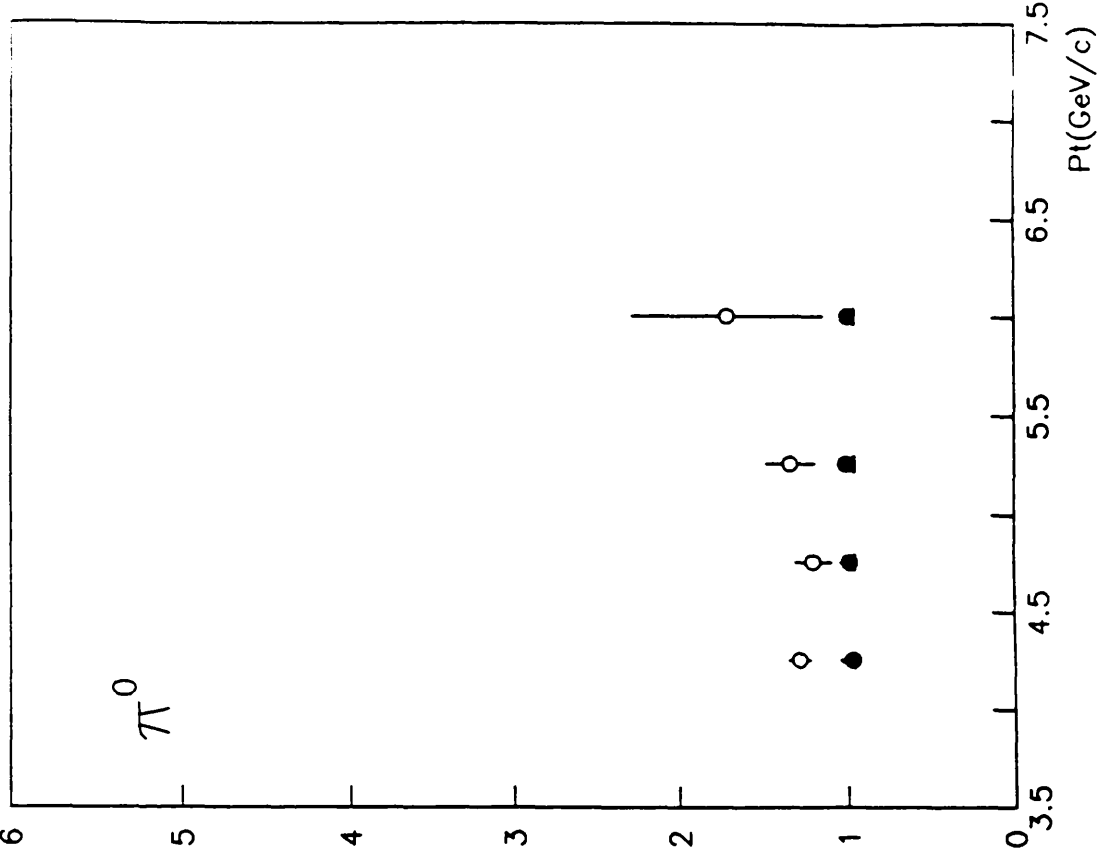


Fig. 6.13

*References*

- [ 1] D. W. Duke et al., Phys. Rev. D30 (1984) 49
- [ 2] J. F. Owens, Phys. Rev. D30 (1984) 943
- [ 3] H. Fritzsch et. al., Phys. Lett. 69B (1977) 316
- [ 4] R. Baier et al., Z Phys C6 (1980) 309
- [ 5] A. P. Contogouris et al., Phys. Rev. D33 (1986) 1265
- [ 6] E. L. Berger et. al., Nucl. Phys. B239 (1984) 52
- [ 7] A. P. Contogouris et. al., Phys. Rev. D32 (1985) 1134
- [ 8] P. Aurenche et al., Phys. Lett. 140B (1984) 87
- [ 9] P. Aurenche et al., Nucl. Phys. B286 (1987) 509
- [10] W. Beusch et al., CERN reports SPSC/77-70
- [11] T. Ferbel et al., Rev. Mod. Phys. 56 (1984)
- [12] R. M. Turnbull, Journal of Physics G14 (1988) 135
- [13] C. De Marzo et al., Phys. Rev. D36 (1987) 8
- [14] J. Badier et al., Z. Phys. C31 (1986) 341
- [15] T. Akesson et al., Phys. Lett. 158B (1985) 282
- [16] T. Akesson et al., Phys. Lett. 123B (1983) 367
- [17] J. A. Appel et al., Phys. Lett. 176B (1986) 239
- [18] A. Bernasconi et al., CERN - EP/87-120

- [19] M. Bonesini et al., Z. Phys. C37 (1988) 535
- [20] M. Bonesini et al., Z. Phys. C38 (1988) 371
- [21] M. Bonesini et al., Nucl. Inst. and Methods A261 (1987) 471
- [22] C. Bovet et al., CERN report 82-13
- [23] M. Bonesini et al., Nucl. Inst. and Methods A264 (1988) 205
- [24] P. Bene et. al. Nucl. Inst. and Methods A270 (1988) 21
- [25] M. Bonesini et al., Nucl. Inst. and Methods A263 (1988) 325
- [26] M. Bonesini et al., Nucl. Inst. and Methods A270 (1988) 32
- [27] J. C. Lassalle et al., Nucl. Inst. and Methods 176 (1980) 371
- [28] Muon Collaboration, private communication
- [29] H. J. Frisch et al., Phys. Rev. D27 (1983) 1001
- [30] H.-U. Bengtsson et al Comp. Phys. Comms. 34 (1985) 251
- [31] T. Sjostrand et al., Comp. Phys. Comms. 27 (1982) 243
- [32] B. Andersson et al., Phys. Rep. 97 (1983) 31
- [33] F. Carena et al., CERN DD/EE/79-1
- [34] J. Badier et al., Z. Phys. C30 (1986) 45
- [35] G. Donaldson et al., Phys. Lett. 73B (1978) 375
- [36] M. Bonesini et al., Z. Phys. C37 (1987) 39